HOKKAIDO UNIVERSITY

Title	鉄鋼排熱利用型熱電発電システムの可能性調査
Author(s)	大矢, 麻美
Degree Grantor	北海道大学
Degree Name	博士(工学)
Dissertation Number	甲第11563号
Issue Date	2014-09-25
DOI	https://doi.org/10.14943/doctoral.k11563
Doc URL	https://hdl.handle.net/2115/59833
Type	doctoral thesis
File Information	Oya_Asami.pdf



Hokkaido University Collection of Scholarly and Academic Papers : HUSCAP

Feasibility Study of Thermoelectric Generation System Using Exhaust Heat from Steel Industry

鉄鋼排熱利用型熱電発電システムの可能性調査

Laboratory of Energy Media

Asami OYA

Hokkaido University

2014

Contents

Chapter 1
General Introduction

1.1 Background 1
1.1.1 Energy supply and demand in Japan 1
1.1.2 Exhaust heat in Japan 4
1.1.3 Exhaust heat in the steel industry 6
1.1.4 Overview of the technologies for the recovery of exhaust heat from the steel industry 7
1.1.5 Overview of thermoelectric power generation technology 9
1.1.6 Thermoelectric elements for sustainable power generation 11
1.2 Purpose and contents of this thesis 15
1.3 References 16

Chapter 2
Energy conservative preparation for thermoelectric $SrTiO_3$

2.1 Introduction 19
2.2 Effects of sintering temperatures in CS-SPS method 22
2.2.1 Objective of section 2.2 22
2.2.2 Experimental 22
2.2.3 Results and discussion 23
2.2.4 Summary 29
2.3 Effects of sintering times in CS-SPS method 30
2.3.1 Objective of section 2.3 30
2.3.2 Experimental 30
2.3.3 Results and discussion 31
2.3.4 Summary 40
2.4 Combustion synthesis of $SrTiO_3$ without $NaClO_4$ for in-situ densification 41
2.4.1 Objective of section 2.4 41
2.4.2 Experimental 41
2.4.3 Results and discussion 44
2.4.4 Summary 56
2.5 Conclusions 57
2.6 References 59

Chapter 3
Energy conservative preparation for thermoelectric Fe_2VAl

3.1 Introduction 63
3.2 Theory 66
3.3 System definition 69
3.3.1 Conventional arc-melting method 69
3.3.2 Single thermite synthesis 75
3.3.3 Double thermite synthesis 77
3.4 Results and discussion 81
3.5 Conclusions 88
3.6 References 89

Chapter 4
Life cycle assessment of thermoelectric power generation system

4.1 Introduction 93
4.2 Life cycle of TEG system 96
4.2.1 Specification of a TEG system 96
4.2.2 Functional unit and evaluation indicator 101
4.2.3 System boundary 103
4.2.4 Collection of data for calculation 105
4.3 Data setting for the TEG system 106
4.3.1 Case A: With Bi_2Te_3-type thermoelectric element 106
4.3.2 Case B: With $SrTiO_3$-type thermoelectric element 117
4.3.3 Case C: With Fe_2VAl-type thermoelectric element 124
4.4 Results and discussion 131
4.5 Conclusions 138
4.6 References 139

Chapter 5
General Conclusions

161

APPENDIX 165
Acknowledgments 169

Chapter 1

General Introduction

1.1 Background

1.1.1 Energy supply and demand in Japan

Many energy resources consumed around the world are derived from fossil fuel, such as crude oil, natural gas, and coal. The extensive amounts of energy consumption since the industrial revolution have raised concerns over the diminishing resources. It is estimated that if consumption remains at the current rate, crude oil, natural gas, and coal will be depleted in approximately 42, 60, and 122 years, respectively [1]. Moreover, the economic progress in developing countries with significant population growth, such as China and India, is increasing the demand for resources.

Figure 1–1 illustrates the primary energy consumption rate and self-sufficiency of major countries in 2011 [2, 3]. The energy consumption structure of major countries is varied. Countries with high dependency on crude oil are relatively common. However, the fractions of coal, biofuel, energy-from-waste, and nuclear energy used are expanding in countries such as China, France, and India. In recent years, there has generally been a tendency to move from crude oil and coal to natural gas. Energy self-sufficiency indicates the amount of domestic production as a percentage of the total primary national energy supply. Uranium can be used as fuel for nuclear power. As the ore is imported, it is believed that nuclear power is categorized as quasi-domestic energy. For the purposes of calculating energy self-sufficiency, nuclear energy is considered to be produced together

with exported electricity domestically. The energy self-sufficiency ratio of Japan is the lowest for all 13 countries (Fig. 1–1). Altering the categorization of nuclear energy to 'imported', would lower the self-sufficiency ratio of Japan to 5%.

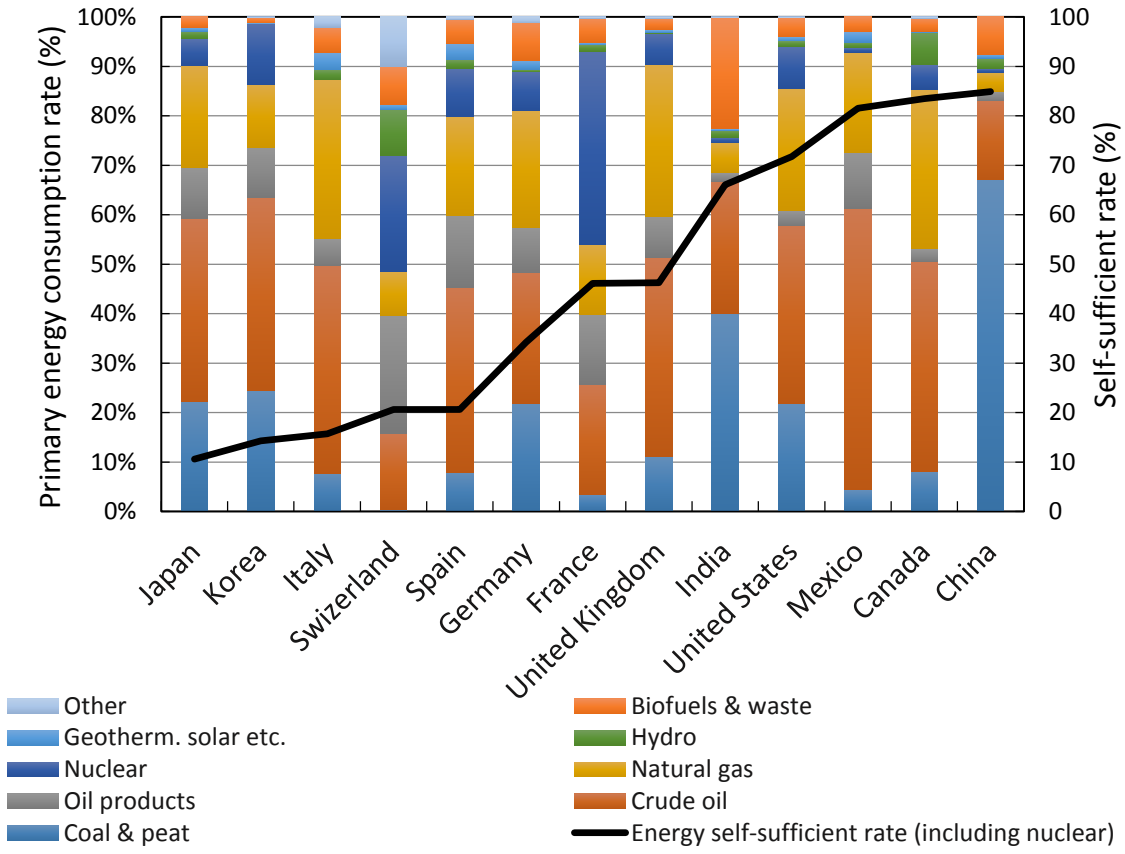


Fig. 1–1 Primary energy consumption rates and energy self-sufficiency ratios of major countries in 2011 [2, 3]

The Tohoku Region Pacific Coast Earthquake in 2011 has altered energy supply with nuclear power plants in Japan operating intermittently due to periodic checks. This has led

to the contribution of nuclear power dropping to 0% as of September 2013. Due to the long-term shutdown of nuclear power plants, thermal power generation has increased, causing a rise in fossil fuel dependence.

Various energy resources such as crude oil, coal, natural gas, etc., were made available in Japan, accounting for a total of 21147 PJ. The final amount of energy consumption was obtained after subtracting the loss in power generation and conversion sector from the total primary energy supply. Figure 1–2 shows the breakdown of the energy consumption of Japan in 2011 [4]. The energy consumption can be divided into the industrial, civilian, and transportation sectors. The industrial sector accounts for 42.8% of the total energy consumed in Japan, of which 93.1% flows into the manufacturing industry. The energy used by the manufacturing industry can be further divided into the chemical industry (36.9%) consuming the most energy, followed by the steel industry (29.3%). Energy consumed in the steel industry accounted for approximately 8% of the total primary energy supply.

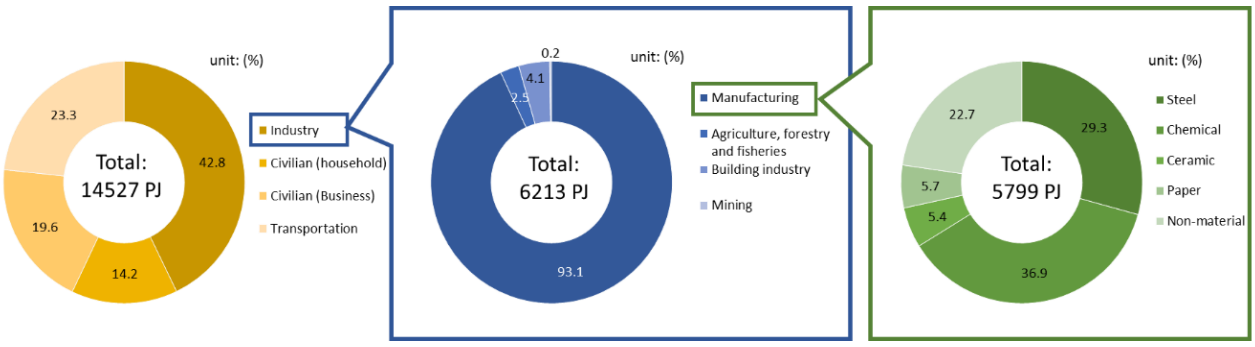
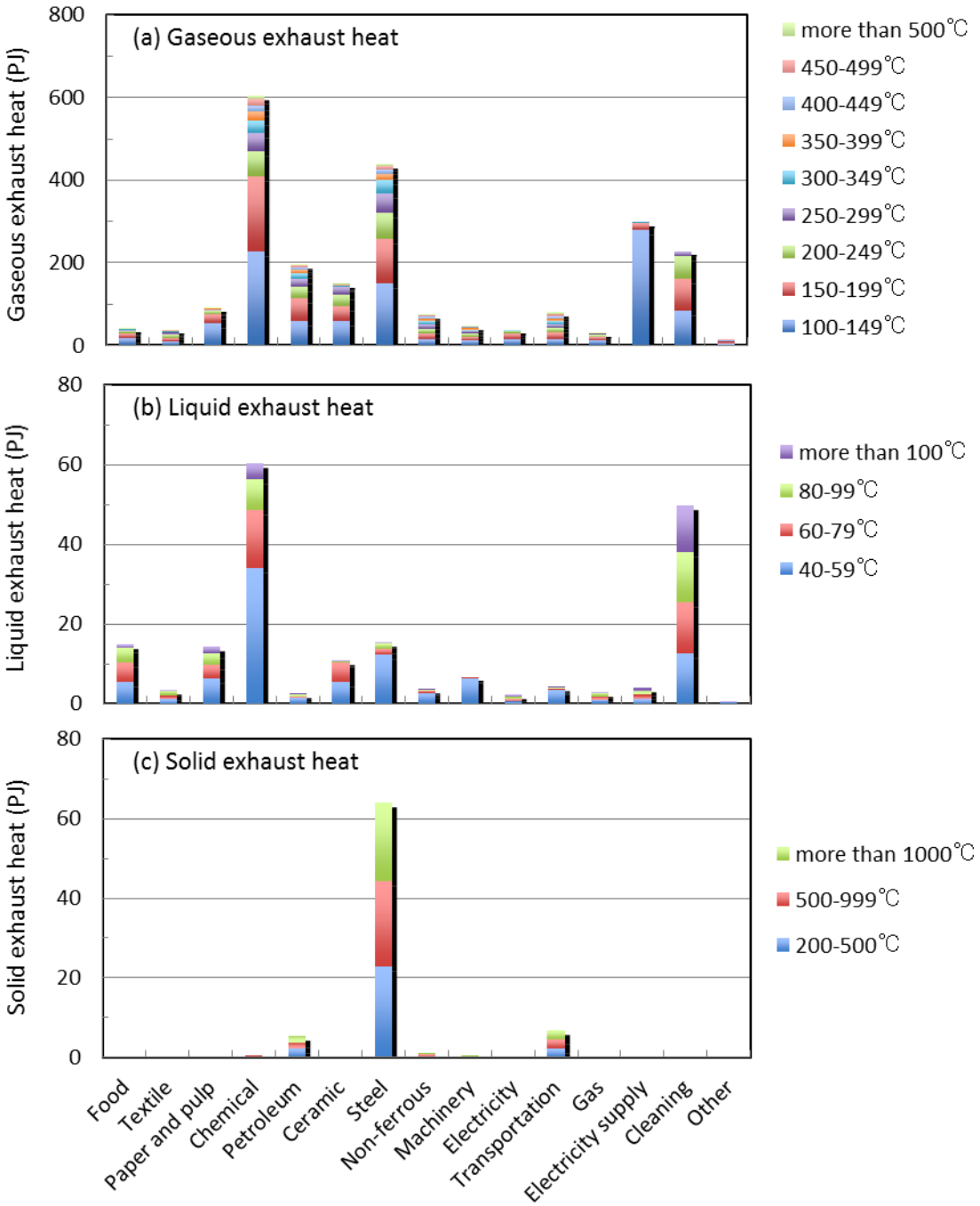


Fig. 1–2 Breakdown of the energy consumption of Japan in 2011 [4]

1.1.2 Exhaust heat in Japan

The Energy Conservation Center, Japan has summarized the state of exhaust heat by industry, form, and temperature in 2001 [5]. Figures 1–3 shows the amount of (a) gaseous, (b) liquid, and (c) solid exhaust heat by industry and temperature. Figure 1–3 (a) demonstrates that the amount of gaseous exhaust heat is large, and can be arranged by industry in decreasing order as chemical, steel, and electricity supply industries. For most industries, gaseous exhaust heat has low-temperatures (up to 200°C), which is relatively difficult to recover. The amount of exhaust heat is small in non-ferrous and transportation industries, but more than half is at temperatures above 200°C, indicating relatively easy recovery. Figure 1–3 (b) illustrates that a lot of liquid exhaust heat is discharged by the chemical and cleaning industries. The proportion of the waste heat at temperatures of 99°C or less is the majority in all industries. Solid exhaust heat is characterized in Figure 1–3 (c), most of the emissions are discharged by the steel industry. High temperature exhaust heat (500°C or more) is in abundance in the steel industry, indicating that there remains much potential to recover.



Figs. 1–3 Amount of (a) gaseous, (b) liquid, and (c) solid exhaust heat by industry and temperature

1.1.3 Exhaust heat in the steel industry

Steel plants have exhaust heat of varying types and amounts, because they produce a wide range of products. Figure 1–4 shows the amount of exhaust heat in a steel plant [6, 7]. The steel plants in Japan use exhaust heat generated from the iron-making process effectively and recover it as steam and electricity.

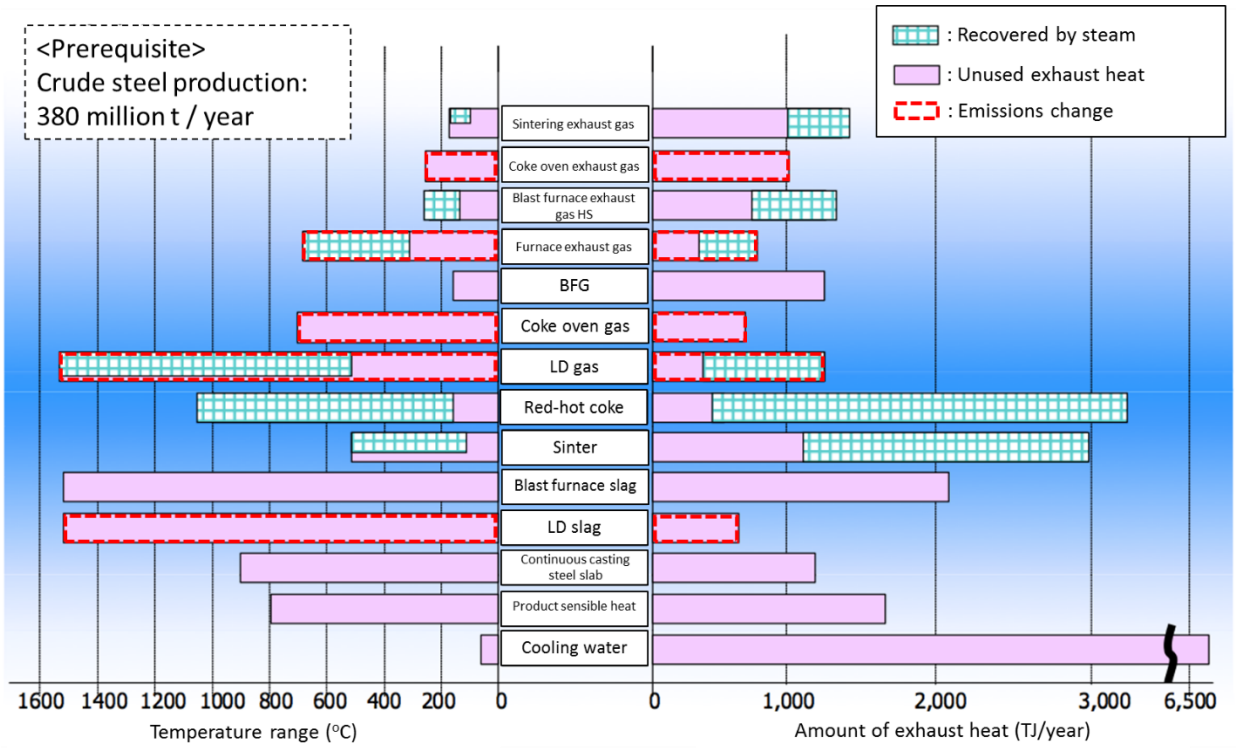


Fig. 1–4 The amount of exhaust heat in a steel plant (modified) [6, 7]

Typical key energy-saving equipment in the steel manufacturing process are as follows [8]:

- Coke dry quenching (CDQ)

  CDQ equipment is intended to extinguish red-hot coke at 1,000°C with an inert

gas such as nitrogen. Sensible heat from circulating gas is recovered with steam at 300 to 500°C in a boiler.

- Top pressure recovery turbine (TRT)

  TRT equipment is used to recover power by turbine expansion with the pressure of a blast furnace gas discharged from the top.

- LD Converter Gas (LDG) recovery facilities and sensible heat recovery equipment

  LDG generated by blowing into the converter is a high-temperature gas, consisting mainly of CO, including a lot of dust. Cooling the LDG, as processing equipment for dust removal, using a non-combustion method is the mainstream.

The penetration rate of the technologies above in Japanese steelworks is 100%, which is unique in comparison to other developed countries. The technologies presented have boosted the energy efficiency of the Japanese steel industry to the world's highest level [6]. This may imply that there is no further potential for energy saving, however, the steel industry must still take measures in order to improve energy efficiency further.

1.1.4 Overview of the technologies for the recovery of exhaust heat from the steel industry

Promising technologies for the recovery of exhaust heat from steelworks have been studied in detail by the Iron and Steel Institute of Japan. Table 1–1 shows typical technologies for the recovery of exhaust heat from steelworks.

Table 1–1 Promising technologies for the recovery of exhaust heat from steelworks

	Kalina cycle	Phase change materials (PCM)	Heat pump	Thermoelectric generator
Output	Thermal⇒Electrical	Thermal⇒Thermal	Thermal⇒Thermal	Thermal⇒Electrical
Initial cost	△	○	○	△
Efficiency	○	△	○	△
Thermal responsiveness	△	○	△	○
Temperature range	Kalina cycle PCM Heat pump Low (R.T.~300 °C)	Medium (300~600 °C)	Thermoelectric power generation	High (600~1000 °C)
Merit	1) Excellent power recovery of sensible heat from the heat source 2) Feasible of structure of which thermal efficiency can be superior to the Rankine cycle	1) Can be used repeatedly 2) Larger thermal stage density than the sensible heat storage 3) Low initial cost	1) Can be driven with only exhaust heat 2) High exergy efficiency 3) Can be output higher temperature than the heat source	1) Quietness and log-term maintenance free due to absence of moving part 2) Applicable to a wide temperature range
Demerit	1) High initial cost 2) Insufficient thermodynamic property data of ammonia-water mixture	1) Usable temperature range is low 2) Thermal storage/release rate is slow	1) Usable temperature range is low 2) High initial cost	1) Low efficiency 2) High initial cost

The Kalina Cycle is a power cycle where the working fluid is a non-azeotropic mixed media, such as ammonia-water, that uses the absorption process. It shows an effective power recovery of sensible heat from heat sources, mainly, gas turbine exhausts Depending on the temperature of the heat source, it is possible to realize a structure in which thermal efficiency is better than that of the Rankine Cycle which is a power cycle that can be recovered exhaust heat of the low temperature. There are a few cases where the Kalina Cycle can be used for the recovery of waste heat around 100°C, however, challenges such as equipment cost and thermal efficiency remain. Phase change material (PCM) is a substance capable of storing heat in high density, utilizing the melting-solidification latent heat. By transporting insulated containers filled with PCM, heat transportation with low-loss is possible. Improvement in thermal storage/releasing rate is necessary to adapt to large amounts of exhaust heat that are produced in steel plants.

A heat pump is a device that produces a temperature difference using heat or power. Since high efficiency can be expected if the temperature rise is small, it is suitable for producing low pressure from hot exhaust water. Using heat-driven pumps, useful steam can be generated from abundant low-temperature exhaust heat with no current use. Utilization of thermoelectric power generation for the recovery of exhaust heat from steelworks is proposed in this study. Since the applicable temperature range is extensive, thermoelectric material can be used without compromising the energy level of high-temperature exhaust heat.

1.1.5 Overview of thermoelectric power generation technology

As mentioned above, many methods have been researched and applied to exhaust heat recovery. Thermoelectric material is a promising candidate among various heat recovery methods for development [9]. Thermoelectric materials can convert thermal energy into electric energy directly, in a process called thermoelectric power generation (TEG). The principle phenomenon that underpins TEG is known as the Seebeck effect, discovered by Thomas Seebeck in 1821. The Seebeck effect is the conversion of a temperature differential into electric energy at the junction of two materials. After 2000, the importance of the concept of spin current was acknowledged. The spin-Seebeck phenomenon that spin pressure is generated from the temperature gradient was defined by Uchida et al. in 2008 [10]. TEG has many advantages that include direct conversion, quietness, a lack of long-term maintenance due to the absence of moving parts, scale-free efficiency, wide temperature range application by selecting elemental types, and no greenhouse gas emissions during power generation, which is the most important merit. Exploiting the merits of TEG, industrial waste heat can be recovered and utilized more

efficiently. In TEG, more than one pair of thermoelectric elements, p-type and n-type are necessary. The merit of thermoelectric material is generally evaluated using the following equation:

$$ZT = T\alpha^2\sigma / \kappa \quad (1\text{–}1)$$

where Z, T, α, σ and κ are figure-of-merit (1/K), absolute temperature (K), Seebeck coefficient (μV/K), electric conductivity (S/cm), and thermal conductivity (W/(m·K)). The term $\alpha^2\sigma$ (W/(m·K^2)) is called the power factor, which is associated to the electric power consumed in the thermoelectric generation [11, 12]. For one pair of thermoelectric materials, the maximum conversion efficiency η_{TEG} can be calculated using the following equations:

$$\eta_{TEG} = \frac{T_{high}-T_{low}}{T_{high}} \cdot \frac{(M-1)}{M+T_{low}/T_{high}} \quad (1\text{–}2)$$

$$\mathrm{M} = \sqrt{1+\frac{1}{2}Z(T_{high}+T_{low})} \quad (1\text{–}3)$$

where Z, T_{high}, and T_{low} are the figure-of-merit of one pair of thermoelectric materials, hot-side temperature, cold-side temperature, and the average operation temperature, respectively. The first term of Eq. (1–2) is Carnot's efficiency, and the second term is related to the merit of the materials. The efficiency of a thermoelectric generator is mainly affected by the temperature difference of the hot and cold sides, and the thermoelectric merit of each material. In other words, to increase the η_{TEG}, Z values of the elements, the T_{high} must be high. Therefore, materials in high-efficiency thermoelectric generation are required to have good heat-resistance at high temperatures, with simultaneously high Z

values.

1.1.6 Thermoelectric elements for sustainable power generation

Figures 1–5 shows the temperature dependence of the dimensionless figure-of-merit, *ZT* of the selected (a) n-type and (b) p-type thermoelectric materials, which were found to have relatively high *ZT* values in the literature [13-29]. To use thermoelectric materials practically in industrial fields, the merit of the materials, as well as the price of the products, the stability of the materials in harsh environments, and their environmental suitability must be appropriate. Many researchers have investigated thermoelectric materials and described various materials. Intermetallic compounds such as Bi-Te alloys and Pb-Te alloys have been reported to have relatively high *ZT* values. In Figure 1–5, Bi-Te alloys are dominant at a relatively lower temperature range. Bi-Te alloys are adopted as materials for commercial use. However, there are some barriers to further practical utilization of Bi-Te alloys typical of intermetallic thermoelectrics. For example, their oxidation and melting at high temperatures can cause degradation of performance. Furthermore, Te and Pb are toxic to the humans, and the use of Pb is restricted to avoid environmental pollution. Intermetallic compounds need surface protection to prevent oxidation and vaporization. To sustain the demand for new thermoelectric materials, which can be used at high temperatures, oxides have begun to attract much attention.

Historically, oxides were not deemed useful for thermoelectric application. This is due to the fact that they are made from light oxygen atoms, and often show low mobility. This position was altered with the discovery of good thermoelectric properties in $Na_xCo_2O_4$ [30].

Recently, there has been an increase in literature published on thermoelectric oxides,

and many oxides have been found to have the potential for thermoelectric application. In Figure 1–5 (b), $TiO_{1.1}$ [25] and $Na_{1.7}Co_2O_4$ [21] have been reported to have high *ZT* values at temperatures above 700 K. Conventional synthesis methods for oxides, such as the solid-state reaction [31, 32], sol-gel method [33-35], and the hot-press sintering method [36], require a solid-state reaction with heating at high temperature for a long periods and grinding to achieve homogeneous products. These conventional methods consume a lot of time and energy. An important strategy for the industrial spread of thermoelectric applications is to reduce the time and energy for manufacture, which would lead to a reduction in the cost of products. Therefore, the establishment of a novel processes to synthesize thermoelectric oxides is urgent.

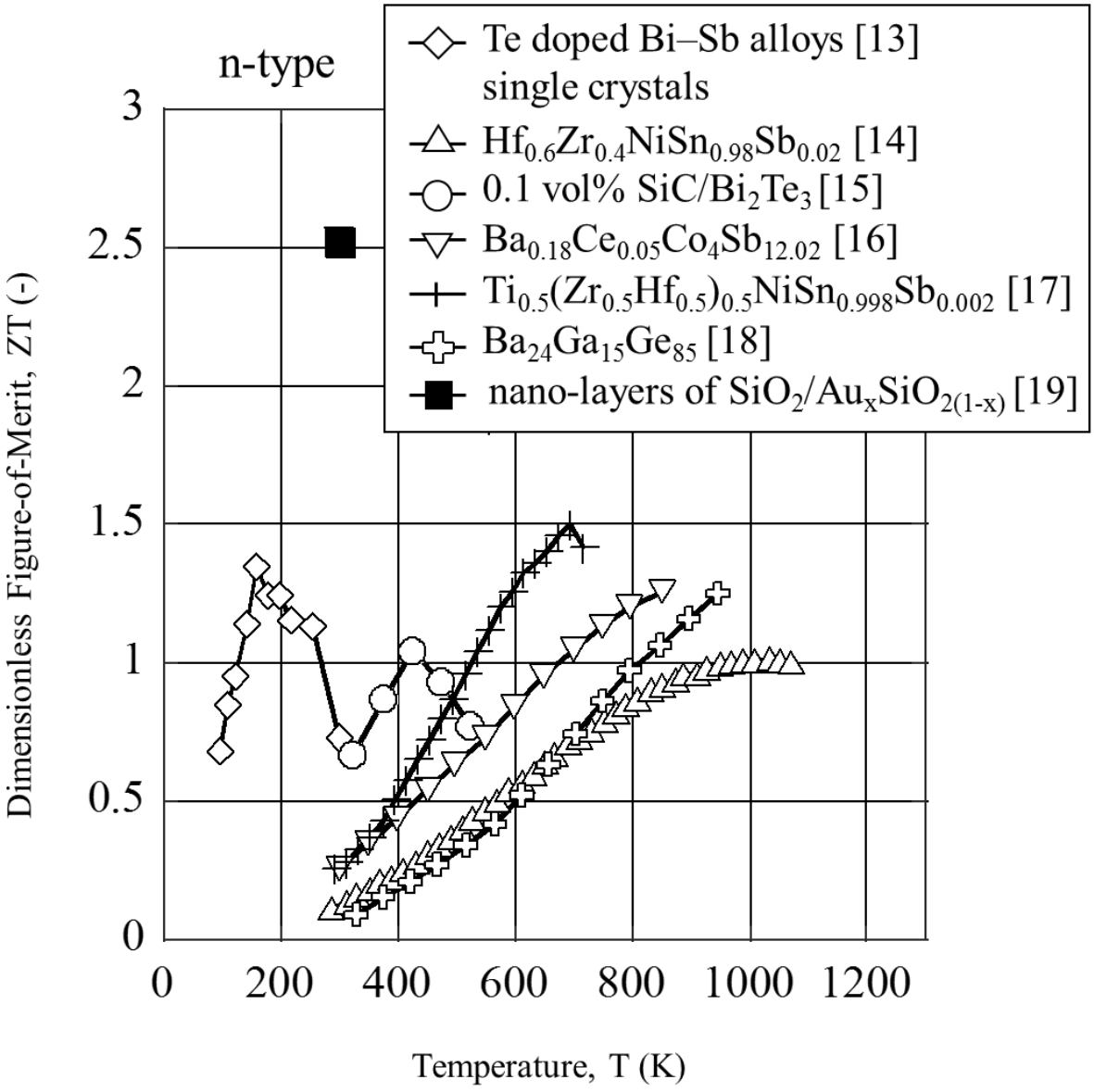


Fig. 1–5 (a) Temperature dependence of the dimensionless figure-of-merit of a variety of n-type thermoelectric materials [13-19]

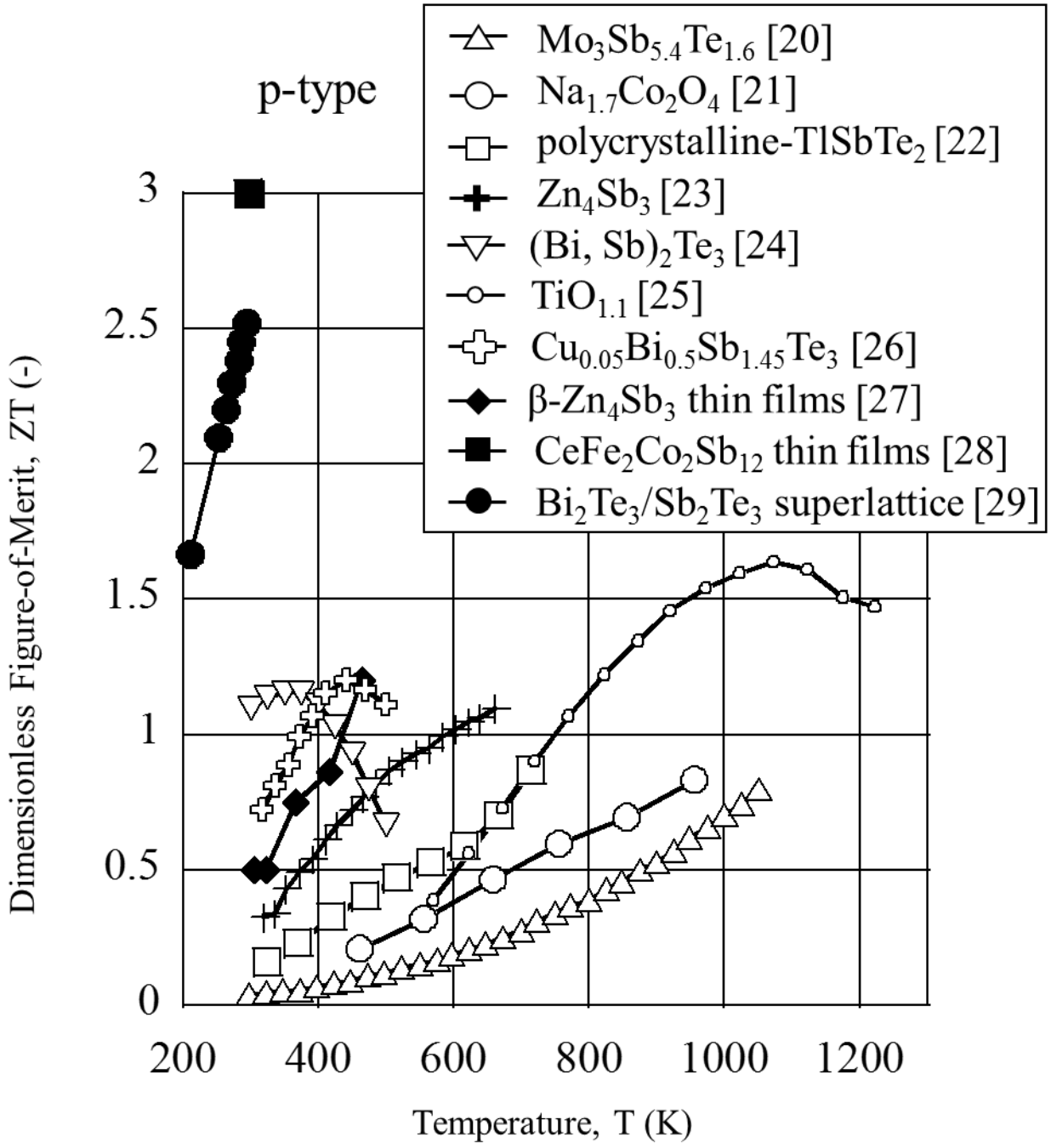


Fig. 1–5 (b) Temperature dependence of the dimensionless figure-of-merit of a variety of p-type thermoelectric materials [20-29]

1.2 Purpose and contents of this thesis

The aim of this thesis is to investigate the feasibility of sustainable thermoelectric power generation systems using exhaust heat from the steel industry. In order to establish a sustainable thermoelectric power generation system and, in turn, reduce energy consumption and the impact on global warming, the following is conducted:

1) Development of exergy conservative preparation for thermoelectric elements, and

2) Life cycle assessment of thermoelectric power generator systems using exhaust heat discharged from the steel industry.

The five chapters constituting this thesis can be described as follows:

Chapter 1: Presents a general introduction.

Chapter 2: Describes energy conservative preparation methods of thermoelectric La-doped $SrTiO_3$, focusing on the effects of operating conditions of spark plasma sintering. In addition, a new combustion route to obtain high-purity $SrTiO_3$, without the use of $NaClO_4$ is examined. The effects of the Ti/TiO_2 ratio in the raw materials, reaction rate, and activation energy are discussed.

Chapter 3: Describes exergy conservative preparation methods of thermoelectric Fe_2VAl, focusing on the enthalpy and exergy changes of the processes.

Chapter 4: Assesses the life cycle assessment of thermoelectric power generation system using exhaust heat discharged from the steel industry. Environmental impacts associated with global warming and energy consumption in the whole life cycle of thermoelectric power generation system are mainly examined, focusing on the type of thermoelectric elements and the difference in performance in power generation.

Chapter 5: Presents the main conclusions of the study.

1.3 References

[1] Trade and Industry The Agency for Natural Resources and Energy in the Ministry of Economy. *Energy in Japan 2010*, (2010).

[2] Trade and Industry The Agency for Natural Resources and Energy in the Ministry of Economy. *Energy white paper 2013*, (2013).

[3] International Energy Agency. (2013). Energy balance of non-OECD countries (2013 edition).

[4] Ministry of Economy Agency for Natural Resources and Energy, Trade and Industry (METI) Japan. *General Energy Statistics*, (2013).

[5] Japan The Energy Conservation Center. *Abstracts of exhaust heat survey of plant group*, (2001).

[6] Research Institute of Innovative Technology for the Earth (RITE). *Carbon dioxide separation and recovery technology development that utilize low-grade waste heat (in Japanese)*, (2008).

[7] Course50. Retrived July 25, 2014, from http://www.jisf.or.jp/course50/tecnology03/#point3.

[8] JFE Techno-Research Corporation. *Energy conservation survey and effective utilization of unused heat energy in the steel industry (in Japanese)*, (2013).

[9] Takenobu Kajikawa. (2011). "*Present, past, and future of the thermoelectric conversion (in Japanese)*": Fundamentals amd Applications of Thermoelectrics -Guidepost to Green Society-, 1st ed., Tokyo: CMC Publishing CO.,LTD.

[10] K. Uchida, S. Takahashi, K. Harii, J. Ieda, W. Koshibae, K. Ando, S. Maekawa, E. Saitoh. (2008). Observation of the spin Seebeck effect. *Nature*, *455*, (7214), 778-781.

[11] E. Altenkirch. (1909). *Physics Z*, *10*, 560.

[12] E. Altenkirch. (1949). *Physics Z*, *12*, 920.

[13] V. S. Zemskov, A. D. Belaya, U. S. Beluy, G. N. Kozhemyakin. (2000). Growth and investigation of thermoelectric properties of Bi-Sb alloy single crystals. *Journal of Crystal Growth*, *212*, 161-166.

[14] Cui Yu, Tie-Jun Zhu, Rui-Zhi Shi, Yun Zhang, Xiu-Bing Zhao, Jian He. (2009). High-performance half-Heusler thermoelectric materials $Hf_{1-x}Zr_xNiSn_{1-y}Sb_y$ prepared by levitation melting and spark plasma sintering. *Acta Materialia*, *57*, 2757-2764.

[15] Li-Dong Zhao, Bo-Ping Zhang, Jing-Feng Li, Min Zhou, Wei-Shu Liu, Jing Liu. (2008). Thermoelectric and mechanical properties of nano-SiC-dispersed Bi_2Te_3 fabricated by mechanical alloying and spark plasma sintering. *Journal of Alloys and Compounds*, *455*, 259-264.

[16] S. Q. Bai, Y. Z. Pei, L. D. Chen, W. Q. Zhang, X. Y. Zhao, J. Yang. (2009). Enhanced thermoelectric performance of dual-element-filled skutterudites $Ba_xCe_yCo_4Sb_{12}$. *Acta Materialia*, *57*, 3135-3139.

[17] Naoki Shutoh, Shinya Sakurada. (2005). Thermoelectric properties of $Ti_X(Zr_{0.5}Hf_{0.5})_{1-X}NiSn$ half-Heusler compounds. *Journal of Alloys and Compounds*, *389*, 204-208.

[18] Jung-Hwan Kim, Norihiko L. Okamoto, Kyosuke Kishida, Katsushi Tanaka, Haruyuki Inui.

(2006). High thermoelectric performance of type-III clathrate compounds of the Ba-Ge-Ga system. *Acta Materialia*, *54*, 2057-2062.

[19] S. Budak, C. Muntele, B. Zheng, D. Ila. (2007). MeV Si ions bombardment effects on thermoelectric properties of sequentially deposited $SiO_2/Au_xSiO_{2(1-x)}$ nano-layers. *Nuclear Instruments and Methods in Physics Research Section B: Beam Interactions with Materials and Atoms*, *261*, (1-2), 1167-1170.

[20] Franck Gascoin, Julia Rasmussen, G. Jeffrey Snyder. (2007). High temperature thermoelectric properties of $Mo_3Sb_{7-x}Te_x$ for x=1.6 and 1.5. *Journal of Alloys and Compounds*, *427*, 324-329.

[21] M. Ito, T. Nagira, D. Furumoto, S. Katsuyama, H. Nagai. (2003). Synthesis of $Na_xCo_2O_4$ thermoelectric oxides by the polymerized complex method. *Scripta Materialia*, *48*, 403-408.

[22] Ken Kurosaki, Hironori Uneda, Hiroaki Muta, Shinsuke Yamanaka. (2004). Thermoelectric properties of thalliun antimony telluride. *Journal of Alloys and Compounds*, *376*, 43-48.

[23] K. Ueno, A. Yamamoto, T. Noguchi, T. Inoue, S. Sodeoka, H. Takazawa, C. H. Lee, H. Obara. (2004). Optimization of hot-press conditions of Zn_4Sb_3 for high thermoelectric performance I. Physical properties and thermoelectric performance. *Journal of Alloys and Compounds*, *384*, 254-260.

[24] Jun Jiang, Lidong Chen, Shengqiang Bai, Qin Yao, Qun Wang. (2005). Thermoelectric properties of textured p-type $(Bi,Sb)_2Te_3$ fabricated by spark plasma sintering. *Scripta Mater.*, *52*, 347-351.

[25] Noriyuki Okinaka, Tomohiro Akiyama. (2006). Latent Property of Defect-Controlled Metal Oxide: Nonstoichiometric Titanium Oxides as Prospective Material for High-Temperature Thermoelectric Conversion. *Jpn. J. Appl. Phys.*, *45*, (9A), 7009-7010.

[26] J. L. Cui, H. F. Xue, W. J. Xiu, W. Yang, X. B. Xu. (2006). Thermoelectris properties of Cu-doped pseudo-binary $Cu_xBi_{0.5}Sb_{1.5-x}Te_3$ (x=0.05-0.4) alloys prepared by spark plasma sintering. *Scripta Mater.*, *55*, 371-374.

[27] L. T. Zhang, M. Tsutsui, K. Ito, M. Yamaguchi. (2003). Thermoelectric properties of Zn_4Sb_3 thin films prepared by magnetron sputtering. *Thin Solid Films*, *443*, 84-90.

[28] S. Güner, S. Budak, C. Muntele, D. Ila. (2009). Effects of MeV Si ions bombardment on the thermoelectric properties of Zn_4Sb_3 and $CeFe_2Co_2Sb_{12}$ thin films. *Surface and Coatings Technology*, *203*, 2664-2666.

[29] Rama Venkatasubramanian, Edward Siivola, Thomas Colpitts, Brooks O'quinn. (2001). Thin-film thermoelectric devices with high room-temperature figures of merit. *Nature*, *413*, 597-602.

[30] I. Terasaki, Y. Sasago, K. Uchinokura. (1997). *Phys. Rev. B*, *56*, 12685-12687.

[31] N. V. Nong, Chia-Jyi Liu, M. Ohtaki. (2011). High-temperature thermoelectric properties of late rare earth-doped $Ca3Co4O_{9+\delta}$. *Journal of Alloys and Compounds*, *509*, (3), 977-981.

[32] A. J. Zhou, T. J. Zhu, X. B. Zhao. (2006). Thermoelectric properties of perovskite-type oxide $La_{1-x}Sr_xCoO_3$ (x = 0, 0.1) prepared by solid state reactions. *Mater. Sci. Eng. B*, *128*, (1-3), 174-178.

[33] Chia-Jyi Liu, Pradipta K. Nayak, Yong-Zhi Chen. (2009). A simple approach of fabricating

thermoelectric γ-Na_xCoO_2 and superconductive $Na_x(H_2O)_yCoO_{2-\delta}$ films using the sol-gel spin-coating method. *Thin Solid Films, 518,* (1), 91-93.

[34] Peng-Peng Shang, Bo-Ping Zhang, Jing-Feng Li, Ning Ma. (2010). Effect of sintering temperature on thermoelectric properties of La-doped $SrTiO_3$ ceramics prepared by sol-gel process and spark plasma sintering. *Solid State Sciences, 12,* (8), 1341-1346.

[35] L. H. Yin, R. Ang, L. J. Li, B. C. Zhao, Y. K. Fu, X. B. Zhu, Z. R. Yang, W. H. Song, Y. P. Sun. (2011). Thermoelectric properties of sol-gel derived cobaltite $Bi_2Ca_{2.4}Co_2O_y$. *Physica B: Condensed Matter, 406,* (14), 2914-2918.

[36] H. Cheng, X. J. Xu, H. H. Hng, J. Ma. (2009). Characterization of Al-doped ZnO thermoelectric materials prepared by RF plasma powder processing and hot press sintering. *Ceramics International, 35,* (8), 3067-3072.

Chapter 2

Energy conservative preparation for thermoelectric $SrTiO_3$

2.1 Introduction

The last decade has seen a big surge in research on thermoelectric oxide materials, with primary focus on improving the thermoelectric properties: electrical conductivity, σ (S/cm), Seebeck coefficient, α (μV/K), and thermal conductivity, κ (W/(m·K)). $SrTiO_3$ [1-4], is a promising semiconductor because of its physical properties such as protonic conductivity at high temperatures [5] and photoluminescence at room temperature [6]. Additionally, $SrTiO_3$ possesses a wide band gap and its applications as electrodes for fuel cells and thermoelectrics have been extensively studied [7-11]. There have been many investigations on fabrication of $SrTiO_3$ ceramics: wet-chemical method [12], solid-state reactions (SSR) [13, 14] method and sol-gel processes [15-17], which have already been widely used in the production of many materials. However, these conventional methods involve many processes therefore they are time and energy consuming. Zhang et al. [1, 18] have proposed a combination of combustion synthesis (CS) and spark plasma sintering (SPS) [19-24] for the synthesis of thermoelectric materials. CS is one of chemical reaction method using the energy of exothermic reaction from raw materials. The principle of the CS is that once one end of the starting mixture is ignited, the exothermic sustainable reaction initiates and causes a combustion wave to propagate through the sample, and the desired product is finally formed without additional energy in

pre-calcining step. In addition to energy saving, the CS can produce a non-equilibrium material when strong exothermic reaction makes rapid heating with quenching of the product. The obtained product is homogeneous with high purity [25].

As compared to the conventional hot-press sintering method, SPS has a very high heating rate and mass transfer rate, enabling samples to be densely sintered in a short period at a relatively low temperature. Thus, the grain growth in the sample might be suppressed, leading to low thermal conductivity. Consequently, SPS appears to be more suitable than conventional methods for preparing thermoelectric materials [24]. Sintering conditions affect its microstructures and properties seriously [26-28]. X. Dong et al. [27] reported that the effect of sintering temperature on crystal structure and electrochemical performance of synthesized $La_{0.80}Mg_{0.20}Ni_{3.75}$ alloy, and found that the density of the samples increases with increasing the sintering temperature. In addition, holding time during sintering seriously affect the microstructures and properties of materials. Zhao et al. [29] have reported the effects of holding time and pressure on microstructure and mechanical properties. Significantly, they found that the density increases with holding time, and the fracture toughness value also depends on the holding time. However, the effects of sintering conditions on the thermoelectric properties have never been researched thus far.

As mentioned above, CS is a unique solid-state combustion method using a highly exothermic reaction between metal powders and an oxidizer as raw materials. In Zhang et al.'s work, $NaClO_4$ is used as a strong oxidizer in CS because of its low cost and ease of handling [25]. During the reaction, $NaClO_4$ is decomposed to release oxygen and NaCl. Most of the NaCl is vaporized out of the reaction system by the high reaction heat during the reaction. Any remaining NaCl can be easily removed with water once the reaction has cooled.

However, the NaCl residual tends to prevent the formation of a fully dense article if the product is directly consolidated by CS without post-treatment. Therefore, the large level of heat discharged from the CS reaction cannot be efficiently used at this stage; typically, another form of heat treatment such as SPS is required to produce dense bulky products. Thus, the development of a new CS method without the use of $NaClO_4$ is necessary in order to fabricate dense bulky $SrTiO_3$ while making efficient use of the exothermic heat during the CS process. Several prominent researchers have already proposed the simultaneous synthesis and sintering methods for diamond-dispersed ceramic composite [30], Nb_5Si_3 and Nb_5Si_3/Nb composites [31], and α- TiN_x ($0 < x \leq 0.3$) [32], but no papers have yet been published on single-phase $SrTiO_3$.

2.2 Effects of sintering temperature in CS-SPS method

2.2.1 Objective of section 2.2

To build up the fabricating method using CS with post SPS for thermoelectric materials, it is essential to survey the effects of sintering temperature on thermoelectric properties. Therefore, in this section, I investigated the effects of sintering temperature on the thermoelectric properties and microstructures of polycrystalline La- doped $SrTiO_3$.

2.2.2 Experimental

Polycrystalline samples of La-doped $SrTiO_3$ (SLTO) were prepared from $SrCO_3$ (99.9% purity, Kanto Chemical, Tokyo, Japan), TiO_2 (99.9% purity, Kanto Chemical, Sakado, Japan), Ti (99.9% purity, Kojundo Chemical, Sakado, Japan), $NaClO_4$ (98.0% purity, Sigma-Aldrich, St. Louis, US10), and La_2O_3 (99.9% purity, Kojundo Chemical, Sakado, Japan). After combustion-synthesis, the obtained products were pulverized into powders in a planetary ball mill (Pulverisette 6, Fritsch, Idor-Oberstein, Germany) operated at 350 rpm for 40 min in air. The particle size of the obtained powders was within 5 μm.

The obtained powders were filled in a cylindrical graphite die (inner diameter = 15 mm) and pressed by using a graphite punch at 37.45 MPa [33]. Then, pulverized powders were sintered by SPS (SPS-511S, Sumitomo Coal Mining, Tokyo, Japan) at a heating rate of 30 K/min and a holding time of 15 min in vacuum. During sintering, the mechanical pressure was maintained at 34 MPa by using plungers. In this section, sintering was carried out at different holding temperatures. The oxygen defect content δ in the sintered

samples was determined by measuring the weight of the samples before and after heating in a furnace at 1373 K for 12 h in air. Heating was repeated twice. δ was calculated assuming that the samples were oxidized to $Sr_{0.92}La_{0.08}TiO_{3.00}$ in furnace. The phase composition and morphology of the products were analyzed by using an X-ray diffractometer (Miniflex, Rigaku, Tokyo, Japan) and a scanning electron microscope (SEM) (JSM-7000F, JEOL, Tokyo, Japan). σ and α were simultaneously measured by using a Seebeck coefficient/electric resistance measuring system (ZEM-3, ULVAC-RIKO, Yokohama, Japan) from room temperature to 1073 K in He atmosphere. κ was calculated as:

$$\kappa = DC_pd \tag{2–1}$$

where D, C_p and d are the thermal diffusivity, heat capacity and experimental density, respectively. The densities of the samples were measured by Archimedes method, and the thermal diffusivity and heat capacity were measured by the laser flash thermal constant analyzer (TC-7000, ULVAC-RIKO, Yokohama, Japan) from room temperature to 1105 K in vacuum.

2.2.3 Results and discussions

The equation of the CS reaction is given as follows:

$$(1-x)SrCO_3 + (1-b)Ti + bTiO_2 + \frac{x}{2}La_2O_3 + \frac{(4-4b-x)}{8}NaClO_4$$
$$\rightarrow Sr_{1-x}La_xTiO_3 + (1-x)CO_2 + \tfrac{(4-4b-x)}{8}NaCl \tag{2–2}$$

In Eq. (2–2), *x* denotes the La-doping content and *b* denotes the TiO_2 content. In chapter 2, *x* and *b* are equal to 0.08 and 0.25, respectively.

Table 2–1 Lattice parameters of synthesized powders before SPS calculated from X-ray diffraction (XRD) data and comparison of sintering temperatures and bulk density after SPS. The value of δ for samples sintered at various sintering temperatures is also shown in this table

Holding temperature [K]	Lattice parameter before SPS [nm]	Bulk density after SPS (g/cm^{-3})	(%T.D.)	The value of δ [−]
1513	0.3902	5.03	96.27	0.0097
1543		5.15	98.57	0.034
1573		5.14	98.49	0.030
1603		5.09	97.56	0.026
1633		5.16	98.91	0.053
1663		5.09	97.55	-

T.D. = 5.24 gcm^{-3}

Table 2–1 lists the lattice parameters of synthesized powders before SPS calculated from X-ray diffraction (XRD) data and comparison of sintering temperatures and bulk density after SPS. The value of δ for samples sintered at various sintering temperatures is also shown in this table. As shown in Table 2–1, density of all samples reached more than 96.27% of the theoretical density (T.D.) (T.D. = 5.24 g/cm^3). Lattice parameter of CSed SLTO powders was 0.3902 nm, which was well accorded with the reported papers [1]. In this section, the samples were sintered at different temperatures from 1513 to 1663 K. However, bulk SLTO was not formed at a sintering temperature of 1663 K, because of the

formation of many intercrystalline cracks. Thus, we concluded that sintering of SLTO was successfully carried out at temperatures from 1513 to 1633 K.

Figure 2–1 shows XRD patterns of SLTO before and after sintering at different temperatures, together with the data of reagent $SrTiO_3$ (99.9% purity, Kojundo Chemical, Sakado, Japan) for comparison. All peaks in this figure very well correspond to that of reagent $SrTiO_3$. This result indicates that SLTO with high purity was prepared by CS. There is no difference between the XRD patterns obtained before and after SPS, indicating that secondary-phase has not appeared during sintering.

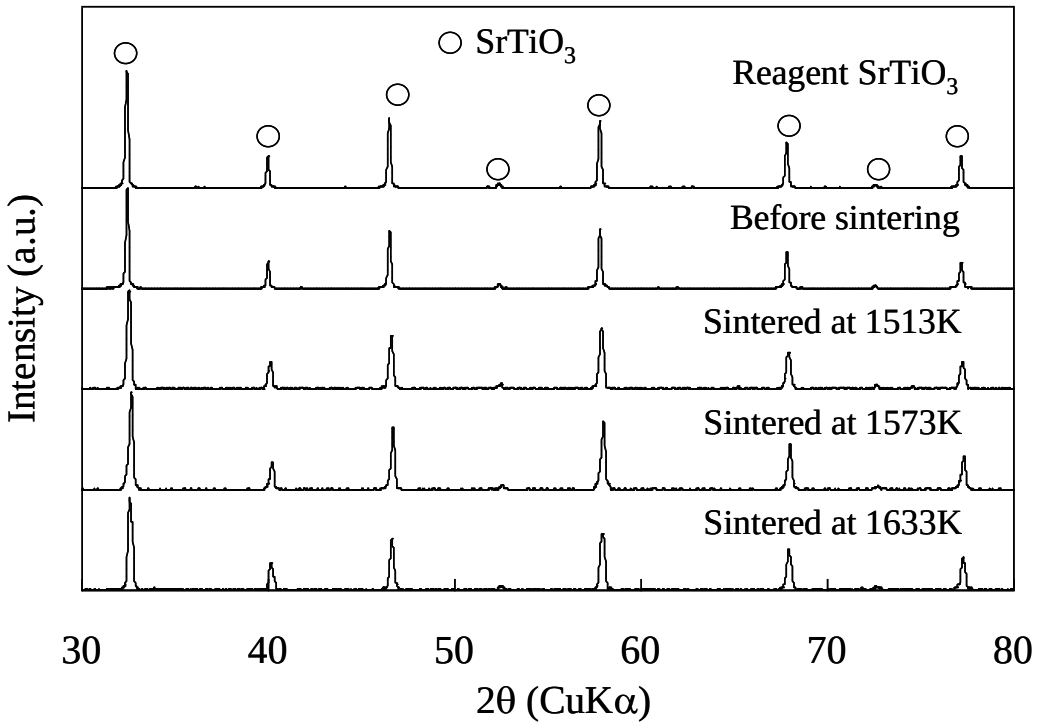
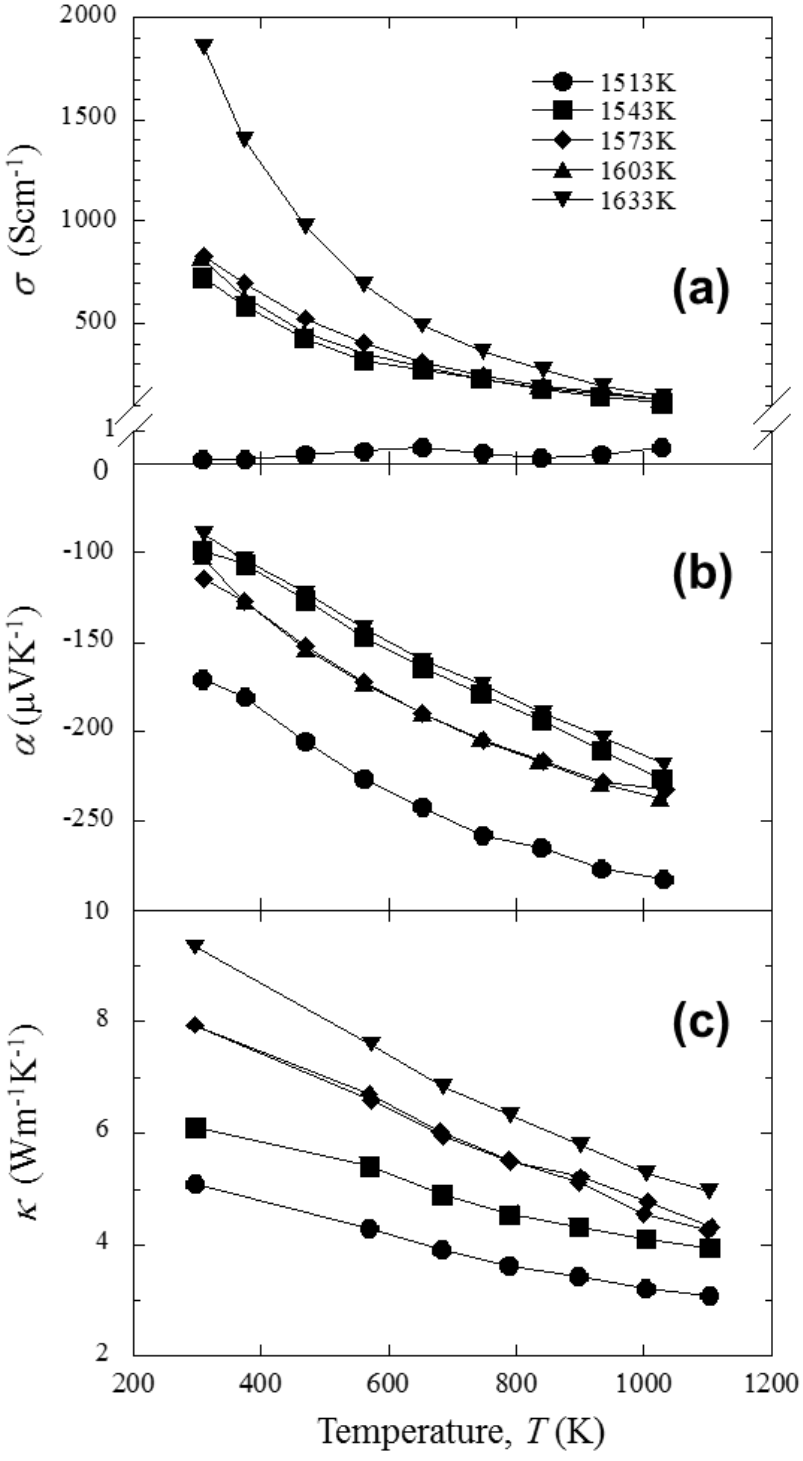


Fig. 2–1 X-ray diffraction patterns of SLTO before and after sintering at different temperatures, together with the data of reagent $SrTiO_3$ for comparison

Figures 2–2 (a), (b) and (c) show the temperature dependence of σ, α and κ of CSed and SPSed SLTO for various sintering temperatures, respectively. As temperature increased, σ decreased and the absolute value of α increased, indicating a metallic behavior. In the experimental temperature range, with an increase in the sintering temperature, σ increased and the absolute value of α decreased due to an increase in the carrier density. When a sample was sintered at high temperature in abutting contact with carbon in vacuum, a lot of oxygen inside particles were liberated. As a result, the sample changed into the nonstoichiometric compound of $Sr_{0.92}La_{0.08}TiO_{3-\delta}$, where δ is the oxygen defect content. Oxygen defects generate electrons as carriers. As shown in Table 2–1, the largest value of δ is 0.053 in a sample sintered at 1633 K, and the smallest value of δ is 0.0097 in a sample sintered at 1513 K. The value of δ of the samples sintered at different temperatures also shows a similar tendency with electric conductivity of the samples. As shown in Figure 2–2 (a), electric conductivity of samples sintered at 1543, 1573, and 1603 K were almost equal values. Therefore, the δ values were also almost equal. Thus, an increase in the sintering temperature leads to an increase in the oxygen defect content, thereby resulting in high σ. Thus, σ increased and the absolute value of α decreased with an increase in the sintering temperature. Thermal conductivity of CSed and SPSed SLTO increased with sintering temperature. With an increase in sintering temperature, average grain size of CSed and SPSed SLTO increased, which caused the decrease of the effects of phonon scattering at grain boundaries. Therefore, thermal conductivity of CSed and SPSed SLTO increased with an increase in sintering temperature.



Figs. 2–2 Temperature dependence on (a) electric conductivity, (b) Seebeck coefficient and (c) thermal conductivity with various sintering temperatures

Figure 2–3 shows temperature dependence on dimensionless figure of merit with various sintering temperatures. In the temperature range considered, ZT of samples sintered at more than 1543 K showed peaks at around 1000 K. ZT of sample sintered at 1513 K showed very low values due to its low electric conductivity shown in Figure 2–2 (c). Among the CSed and SPSed SLTO, sample sintered at 1573 K showed the maximum ZT of 0.16 at 1005 K. These results indicate that for production of SLTO by the combination of CS and SPS, sintering should be done at 1573 K.

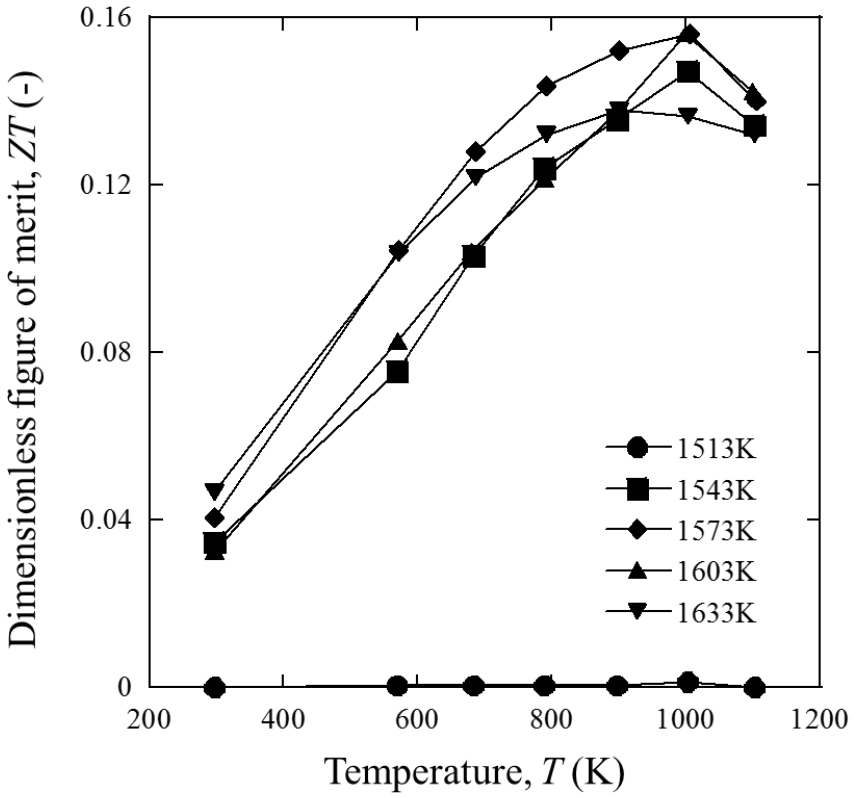


Fig. 2–3 Temperature dependence on dimensionless figure of merit with various sintering temperatures

2.2.4 Summary

I successfully synthesized La-doped $SrTiO_3$ by the combination of CS with post SPS and figured out the effects of sintering temperature on the thermoelectric properties of polycrystalline $Sr_{0.92}La_{0.08}TiO_3$ and following results were obtained:

(1) Spark- plasma- sintering of $Sr_{0.92}La_{0.08}TiO_3$ was successfully carried out at 1513 to 1633 K in temperature. $Sr_{0.92}La_{0.08}TiO_3$ powders were not sintered well at 1663 K due to the formation of many intercrystalline cracks.

(2) High-temperature sintering resulted in introduction of a lot of oxygen defects which produced electrons as carriers. Thus, samples sintered at higher temperature showed large electric conductivity. However, high-temperature sintering also caused an increase in thermal conductivity because of the increase in average grain size, therefore the most optimum sintering temperature maximized ZT was 1573 K.

(3) With increasing temperature, ZT showed an increasing tendency and showed peaks at around 1000 K. The maximum ZT of 0.16 at 1005 K was obtained from the sample sintered at 1573 K.

2.3 Effects of sintering times in CS-SPS method

2.3.1 Objective of section 2.3

The purpose of this section was to investigate figures of merit of La-doped $SrTiO_3$ prepared by CS with post SPS, with the main focus being on the study of the effect of holding time during sintering. The new findings of this study will provide information for maximizing the figures of merit not only of $SrTiO_3$-based materials but also of various other oxide-based materials.

2.3.2 Experimental

Polycrystalline samples of SLTO were prepared from $SrCO_3$ (99.9% purity, Kanto Chemical Co., Inc., Tokyo, Japan), TiO_2 (99.9% purity, Kanto Chemical Co., Ltd., Sakado, Japan), Ti (99.9% purity, Kojundo Chemical Co., Ltd., Sakado, Japan), $NaClO_4$ (98.0% purity, Sigma-Aldrich, St. Louis, MO, USA), and La_2O_3 (99.9% purity, Kojundo Chemical Laboratory Co., Ltd., Sakado, Japan). Details of the experimental procedure have already been already published elsewhere [15]. The combustion-synthesized products were pulverized into powders in a planetary ball mill (Pulverisette 6, Fritsch, Idar-Oberstein, Germany) operated at 350 rpm for 40 min in air. The average particle size of the ground powders was measured using a fiber optic dynamic light-scattering photometer (Otsuka Electronics Co., Ltd., Tokyo, Japan). The powders obtained were placed in a cylindrical graphite die and sintered by SPS (SPS-511S, Sumitomo Coal Mining, Tokyo, Japan) at a heating rate of 30 K/min at 1573 K [27] in a vacuum. In this section, the samples were sintered at holding times of 1, 5, 15, and 30 min under

mechanical pressure conditions of 34 MPa produced using plungers. In a preliminary test, sintered SLTOs (10.0 mg) were heated to 1373 K at a heating rate of 3 K/min and an air-flow rate of 50 ml/min [28]. The weight of the sample gradually increased, and then, it reached a steady state after 12 h, therefore an experimental time of 24 h was enough for perfect oxidation of the sample. In the experiments, the samples were oxidized to $Sr_{0.92}La_{0.08}TiO_{3.00}$ in an electric furnace. The oxygen defect content, δ was determined by measuring the weight increase of the sample after heating at 1373 K for 24 h in air. The phase compositions and morphologies of the products were analyzed using an X-ray diffractometer (Miniflex, Rigaku, Tokyo, Japan) and a scanning electron microscope (SEM) (JSM-7000F, JEOL, Tokyo, Japan). The electrical resistivities and Seebeck coefficients were measured simultaneously using a Seebeck coefficient/electric resistance measuring system (ZEM-3, ULVAC-RIKO, Yokohama, Japan) from room temperature to 1045 K in helium atmosphere. The thermal conductivity was calculated as equation (2–1).

2.3.3 Results and discussions

The CS reaction equation is given as equation (2–2) [25]. Figure 2–4 shows SEM images of cross-sections of SLTO sintered at 1573 K for (a) 1 min, (b) 5 min, (c) 15 min, and (d) 30 min, together with an image of (e) the powder before sintering. The average particle size of the ground powders was found to be 0.722 μm by fiber optic dynamic light-scattering photometer. As shown in Figure 2–4, the grain sizes of the sintered samples gradually increased with holding time up to 15 min. Even for a holding time of 30 min, the grains in the sintered sample did not grow larger than those obtained by sintering for 15 min. In the 30-min-sintered sample, microparticles attached to the large grains grew well.

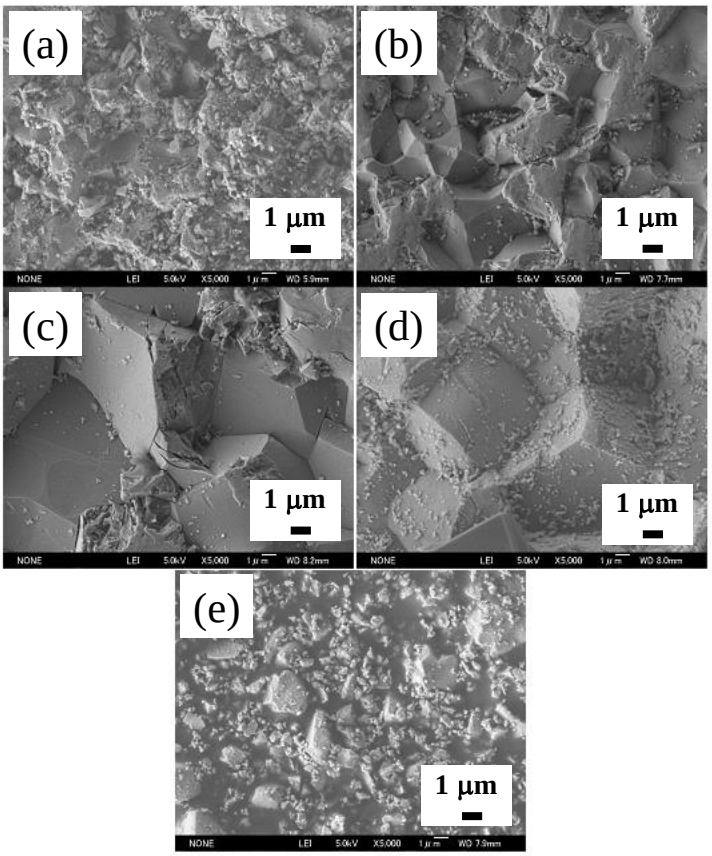


Fig. 2–4 SEM images of cross-sections of SLTO sintered at 1573 K for (a) 1 min, (b) 5 min, (c) 15 min, and (d) 30 min and (e) image of powders before sintering

Table 2–2 lists holding times during sintering, lattice parameters of the synthesized powders before SPS, which were calculated from X-ray diffraction (XRD) data, the bulk densities after SPS, and the δ values for each sample prepared. The densities of the samples sintered for more than 5 min reached 96.8% of the theoretical density (T.D. = 5.24 g/cm^3). The density of the sample sintered for 1 min reached only 66.2% of T.D., which was 46.2% lower than in the other cases. This showed that bulk SLTO was densely

sintered when the sintering times were greater than 5 min. The lattice parameter of the CSed SLTO powders was 0.3902 nm, which agreed well with other reported results [1].

Table 2–2 Lattice parameters of the synthesized powder before SPS and comparison of sintering temperatures and bulk density after SPS

Holding time [min]	Lattice parameter before SPS [nm]	Bulk density after SPS		The value of δ [–]
		[g・cm^{-3}]	[%T.D.]	
1	0.3902	3.47	66.2	0.019
5		5.12	97.7	0.031
15		5.14	98.5	0.030
30		5.07	96.8	0.061

T.D.: Theoritical dencity, T.D.=5.24 [g・cm^{-3}]

Figure 2–5 shows XRD patterns for SLTO before and after sintering for different holding times, together with data for the raw materials before CS. All the product peaks corresponded very well to those of $SrTiO_3$. This result shows that the prepared SLTO was of high purity. The positions of all the peaks shifted to lower angles with increasing holding times. This was probably because prolonging sintering introduced more oxygen defects. No new peaks were observed in the XRD patterns of the samples after SPS. This means that a secondary phase did not emerge during sintering.

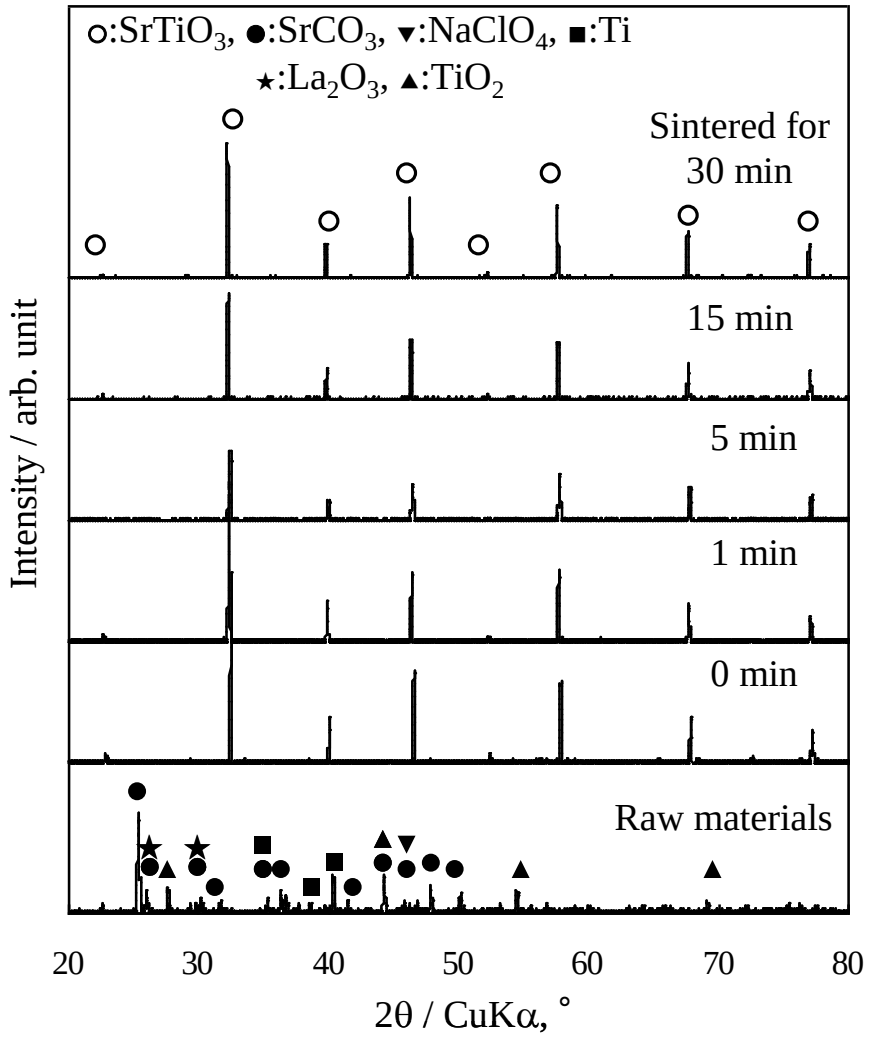


Fig. 2–5 XRD patterns of SLTO before and after sintering for different holding times, together with the data for raw materials before CS

Figures 2–6 (a), (b), and (c) show the temperature dependence of the electrical conductivities, the Seebeck coefficients, and the thermal conductivities, respectively, of the products obtained by sintering for different times. With increasing temperature, the electrical conductivities decreased and the absolute values of the Seebeck coefficients increased, as is seen with metals. With increasing sintering times, the electrical conductivities increased and the absolute values of the Seebeck coefficient decreased,

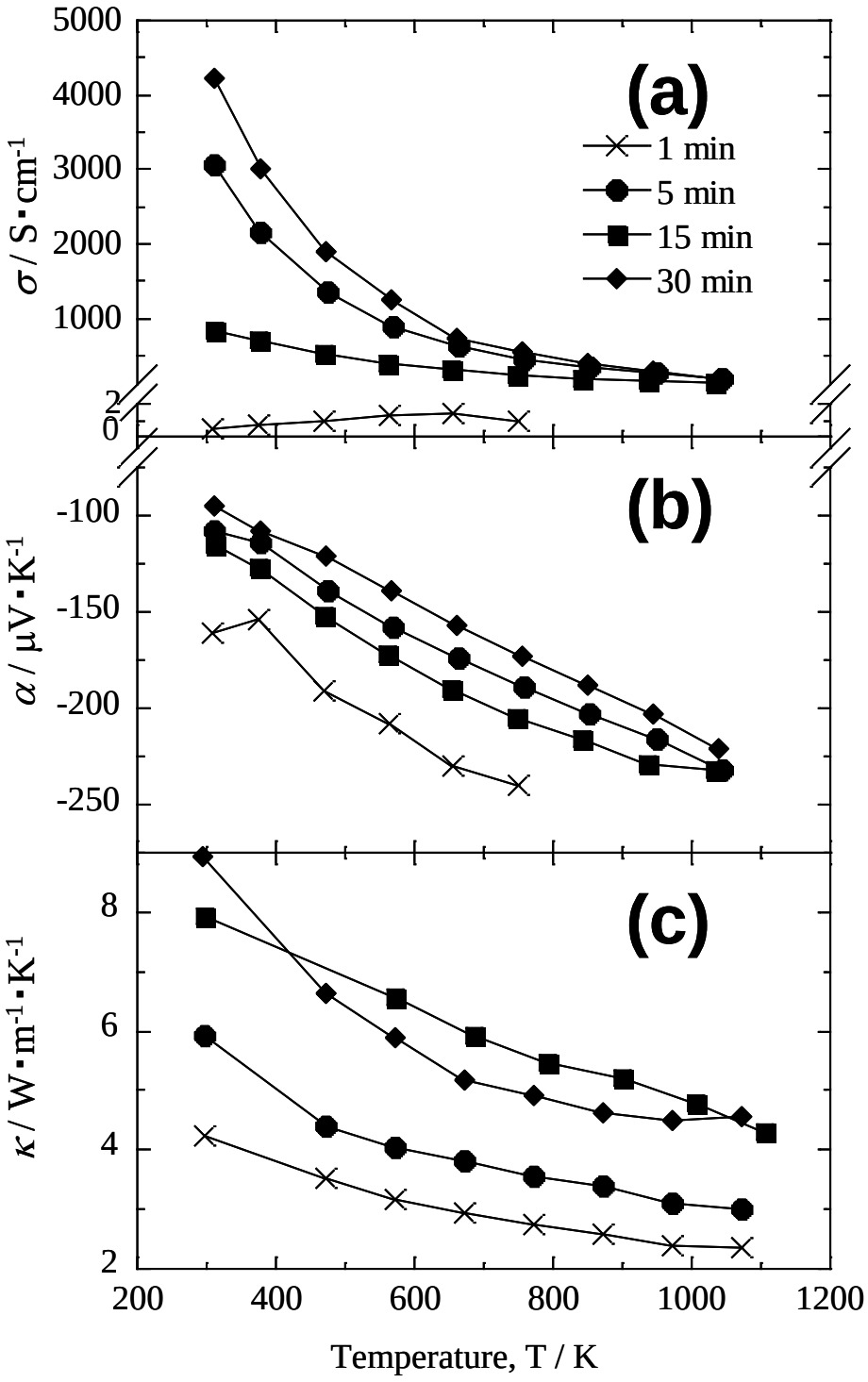
other than in the case of the 5-min-sintered sample. The sample of SLTO powder was placed in a cylindrical graphite die and sintered by SPS, and carbon could gradually reduce SLTO at high temperatures. As a result, the product obtained after prolonged sintering was the nonstoichiometric compound $Sr_{0.92}La_{0.08}TiO_{3-\delta}$, where δ is the oxygen defect content. Oxygen defects generate carrier electrons. Therefore, the value of δ can be treated as the carrier density. The electrical conductivity and Seebeck coefficient [29] can be expressed by the following equations:

$$\sigma = ne\mu. \tag{2–3}$$

$$\alpha = -\frac{k_B}{e}\left\{r + 2 + ln\frac{nh^3}{2(2\pi m^* k_B T)^{\frac{2}{3}}}\right\}. \tag{2–4}$$

In equations. (2–3) and (2–4), n, e, μ, k_B, r, h, m^*, and T are the carrier density, elementary charge, mobility, Boltzmann's constant, scattering factor, Planck's constant, effective mass, and absolute temperature, respectively. From equations. (2–3) and (2–4), it is obvious that the electrical conductivity and Seebeck coefficient are proportional to the carrier density; in other words, they are proportional to the value of δ because the elementary charge and Seebeck coefficient have negative values in n-type semiconductors. Table 2–2 shows that the δ values for the different SLTO sintering times follow the order 30 min > 5 min > 15 min > 1 min, and the δ value of the 5-min-sintered sample is slightly higher than that of the 15-min-sintered sample. This tendency agrees well with Figures. 2–6 (a) and (b), which show that the order of the sizes of the electrical conductivities and Seebeck coefficients for the different SLTO sintering times is 30 min > 5 min > 15 min > 1 min, which is the same order as that of the δ values. The δ values of CSed and SPSed SLTO increased with increasing holding times, which caused the electrical conductivities

and Seebeck coefficients to increase. Thus, an increase in the holding time leads to an increase in the oxygen defect content, resulting in high electrical conductivities and Seebeck coefficients.



Figs. 2–6 Temperature dependence of (a) electrical conductivity, (b) Seebeck coefficient, and (c) thermal conductivity of CSed and SPSed SLTO for various holding times

The thermal conductivities of CSed and SPSed SLTO decreased with temperature. The 15- and 30-min-sintered samples showed a systematic decrease in thermal conductivity with increasing temperature, indicating that phonon–phonon scattering is dominant in the experimental temperature range. The thermal conductivities of the 1- and 5-min-sintered samples were lower and less dependent on the temperature. This is because of the relative increase in temperature-independent phonon–impurity scattering. The order of the sizes of the thermal conductivities of the SLTO samples obtained using different sintering times is 30 min ≈ 15 min > 5 min > 1 min, which is the same sequence as that of the average grain sizes. With an increase in holding time, the average grain size of CSed and SPSed SLTO increased, causing a decrease in the effect of phonon scattering at grain boundaries. Sample density also affected the thermal conductivity. The 1-min-sintered sample, with 66.2% T.D., had the lowest thermal conductivity at respective temperatures. Therefore, longer holding times during sintering increased the average grain size of the sintered samples, and densified them. As a result, the thermal conductivities of the sintered samples increased with holding time.

Figure 2–7 shows the temperature dependence of dimensionless figures of merit for various holding times. I compared our data with reference data [1,10] for polycrystalline $SrTiO_3$-based bulk ceramics reported by Zhang et al. and Ohta et al. In the temperature range considered, *ZT* values of the sample sintered for 1 min were very low because of the sample's low electrical conductivity, as shown in Figure 2–6 (a). The *ZT* values of the 5-min-sintered sample increased with temperature, and the values have a tendency to increase at even higher temperatures; this showed that this sample is suitable for high-temperature applications. Among my samples, SLTO sintered for 5 min showed the maximum *ZT* of 0.37 at 1045 K. This value is the largest value ever reported for $SrTiO_3$-based bulk semiconductors, apart from that of Nb-doped $SrTiO_3$ epitaxial films

reported by Ohta et al. [9]. Generally, thermoelectric modules are composed of bulk polycrystalline materials. Our sample can be used for this application because of its high *ZT* values and suitability for high-temperature usage. The optimum holding time for sintering was 5 min at 1573 K [27]. All of these results proved that CS with post SPS is a promising method for the fabrication of thermoelectric materials.

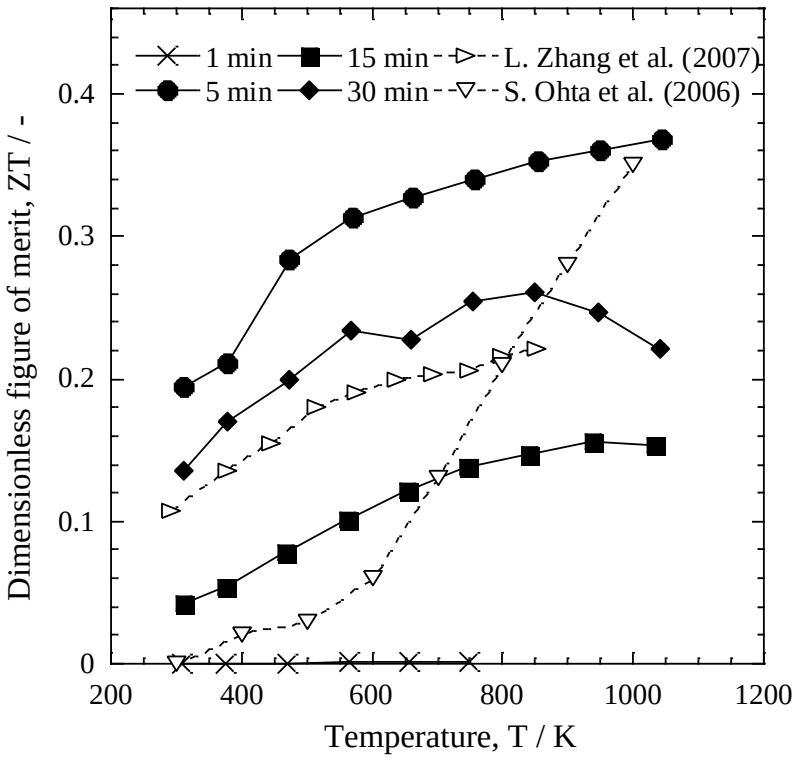


Fig. 2–7 Temperature dependence of dimensionless figure of merit for various holding times during sintering, compared with *ZT* data for heavily Nb-doped $SrTiO_3$ and La-doped $SrTiO_3$ reported by Ohta et al. [10] and Zhang et al. [1], respectively

2.3.4 Summary

I studied the effect of sintering time on figures of merit of La-doped $SrTiO_3$ prepared by a combination of CS with post SPS. The following results were obtained:

(1) Prolonged sintering introduced more oxygen defects into the sample, which can produce carrier electrons. Thus, samples sintered for longer times, except for the sample sintered for 15 min, showed higher electrical conductivities.

(2) Prolonged sintering increased the grain size of the samples, which caused higher thermal conductivities.

(3) The sample sintered for only 5 min recorded the maximum *ZT* value of 0.37 at 1045 K. This is the largest value reported thus far for $SrTiO_3$-based bulk semiconductors.

The results also suggest that the combination of CS with post SPS can be used to commercially produce thermoelectric oxides for use in efficient electricity generation.

2.4 Combustion synthesis of $SrTiO_3$ without $NaClO_4$ for in-situ densification

2.4.1 Objective of section 2.4

The purpose of section 2.3 was to obtain highly pure $SrTiO_3$ powders in a CS reaction without using $NaClO_4$ to establish an in situ densification method of $SrTiO_3$ ceramics.

2.4.2 Experimental

Polycrystalline samples of $SrTiO_3$ were prepared from SrO_2 (98.0% purity, Sigma-Aldrich, St. Louis, MO, USA), TiO_2 (97.0% purity, Alfa Aesar, A Johnson Matthey Company, Ward Hill, MA, USA), and Ti (99.0% purity, Alfa Aesar, A Johnson Matthey Company, Ward Hill, MA, USA). These chemicals were mechanically mixed for 4 h in a ball mill (U.S. Stoneware, Mahwah, NJ, USA) in air and pressed into pellets 2.0 cm in diameter under a load of 0.5 metric tons. Reactant pellets were placed inside a custom-made CS reactor (Figure 2–8) and ignited under an oxygen atmosphere using a graphite igniter controlled by a variable autotransformer (Staco Inc., Dayton, OH, USA). The ignition period was about 2 s. After ignition, the igniter was turned off and the combustion front moved forward and converted the reactants to product. In this CS reaction scheme, Ti powder is a fuel source providing the heat required to sustain the combustion front movement. SrO_2 and TiO_2 served as both the solid oxidizer and the filler. The oxygen decomposed from SrO_2 and TiO_2 oxidized the adjacent Ti powder, making the reaction less dependent on oxygen diffusing from the surrounding atmosphere. A

temperature profile of the CS reaction was recorded by a K-type thermocouple (Omega CHAL-020, Stamford, CT, USA) inserted into the centerline of the pellet. The surface temperature of the pellet was recorded by an IR camera. Upon completion of the CS, the products were analyzed by XRD (Bruker D8 Discover GADDS) to determine their phase purity.

The thermal behaviors of the reactants were studied using an SDT Q600 DSC/TGA (TA Instrument, New Castle, Delaware, USA). In all thermal analyses, alumina powders were used as a reference. A loose mixture of SrO_2, Ti, and TiO_2 (SrO_2:Ti:TiO_2 = 1.00:0.175:0.825) was analyzed by TG/DSC under an oxygen atmosphere to further investigate the reaction mechanism during CS. Additionally, loose powders of the reactants, i.e., SrO_2, and a mixture of Ti and TiO_2 powders, were analyzed. Loose powders were used to minimize oxygen diffusion resistance. Oxygen at a flow rate of 60 mL/min was used. The heating rate was set at 2 °C/min (slow heating rate) or based on a DTA temperature program (fast heating rate). Fast heating rates of 188 °C/min at room temperature to 1050 °C and 88 °C/min at 1050 to 1300 °C were employed to simulate CS reaction conditions. A slow heating rate (2 °C/min) was used to study the activation energy of the CS reaction.

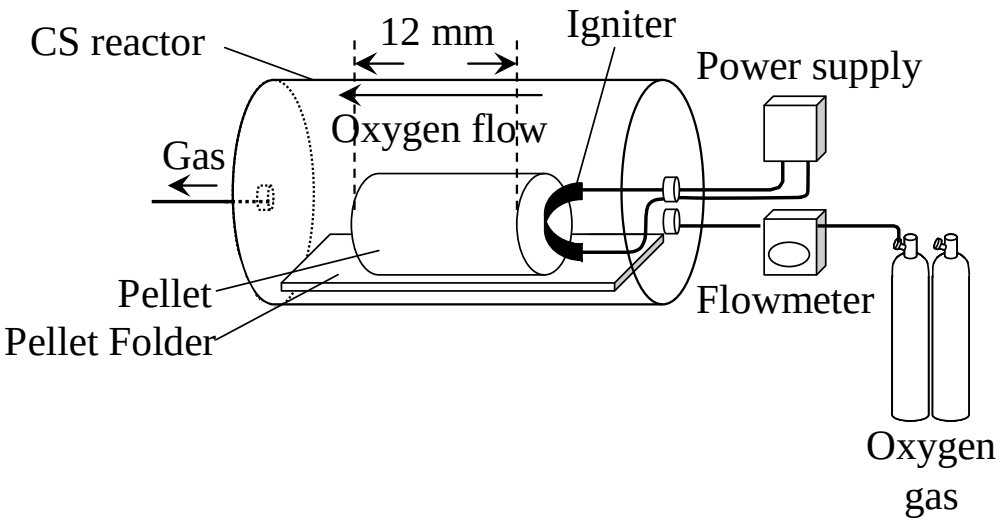


Fig. 2–8 Sketch of CS reactor

2.4.3 Results and discussion

Thermal gravimetric analysis of SrO_2 heated at a fast heating rate in oxygen is shown in Figure 2–9. Three mass losses started at about 450, 550, and 730 °C. The abrupt mass loss is attributed to the decomposition of SrO_2, forming SrO and O_2. This decomposition is endothermic, as indicated by a negative DSC peak. The endothermic peak reaches a minimum at 147 °C. The mass loss (17%) caused by decomposition of SrO_2 is in agreement with a complete decomposition of SrO_2 to SrO. The decomposition of SrO_2 in oxygen during the CS reaction can be described by Equation (2–5):

$$SrO_2 \rightarrow SrO + \frac{1}{2}O_2 \quad (450-1005\ ^\circ C) \qquad (2–5)$$

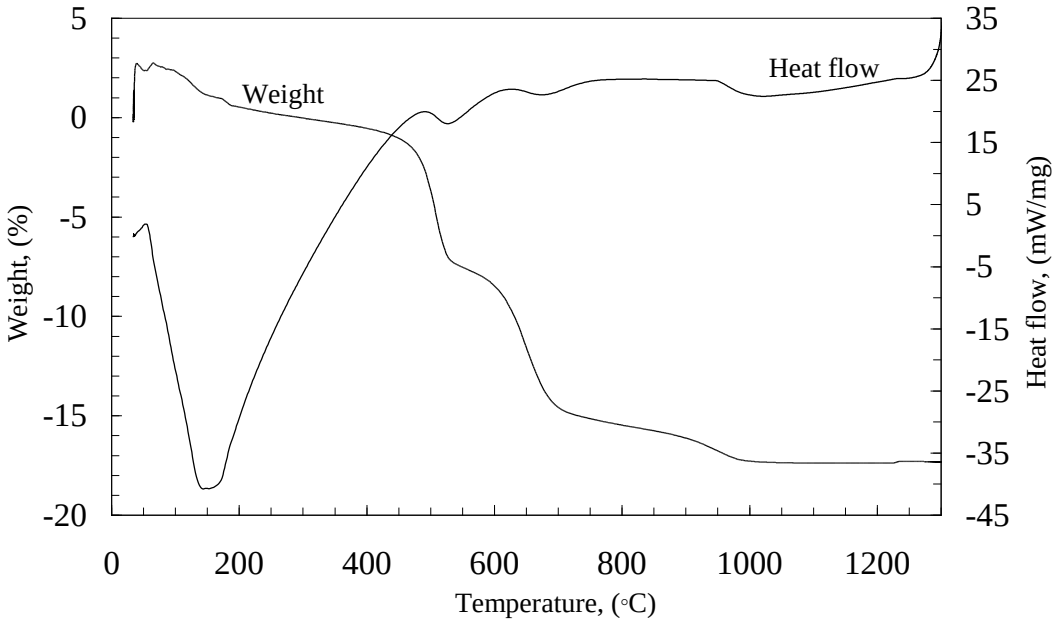


Fig. 2–9 TG/DSC of SrO_2 in oxygen heated at rate of 50 ^oC/min

Figure 2–10 depicts the TG curve for TiO_2 heated at a fast heating rate in oxygen. Small negative DSC peaks can be seen at 196 and 258 °C. The mass change during heating was under ±1%, indicating that TiO_2 is stable at high temperatures and no chemical change occurs.

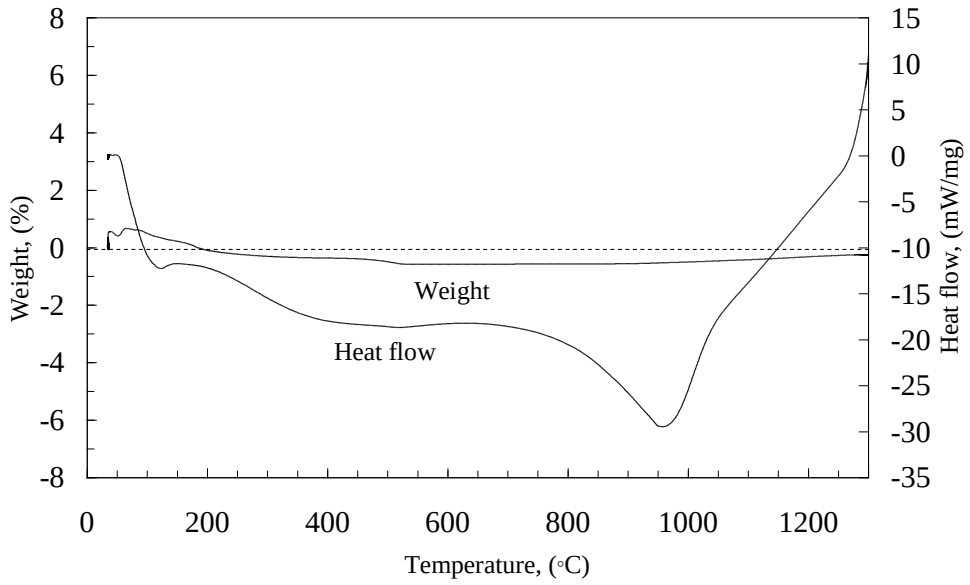


Fig. 2–10 TG/DSC of TiO_2 powders in oxygen heated at rate of 50 ^oC/min

Figure 2–11 shows the TG curve for Ti metal on TiO_2 heated at a fast heating rate in oxygen. The TiO_2 powders were placed at the bottom of the sample holder to protect the sample holder. The mass change and heat flow below 200 °C, shown in Figure 2–11, were broadly similar to those shown in Figure 2–10, demonstrating that any mass change and heat flow around 200 °C can be attributed to TiO_2. Oxidation between 700 and 750 °C is illustrated in Figure 2–11. The mass gain during the oxidation (~56%) is in agreement with complete oxidation of Ti to TiO_2. Equation (2–6) describes the oxidation of Ti in oxygen during the CS reaction:

$Ti + O_2 \rightarrow TiO_2$ (700－750 °C) (2–6)

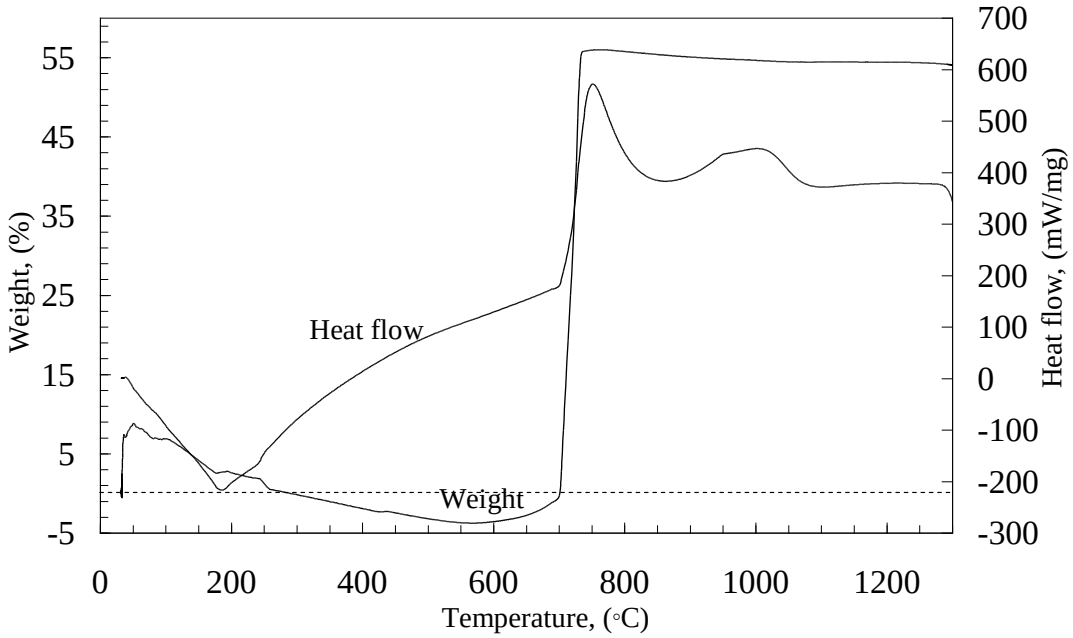


Fig. 2–11 TG/DSC of Ti on TiO_2 in oxygen heated at rate of 50 ^{o}C/min

Figure 2–12 shows a TG curve for a sample containing a mixture of reactants heated at a fast heating rate in oxygen. A loose mixture with the molar ratio of reactants SrO_2:Ti:TiO_2 = 1.00:0.175:0.825 was prepared. Two main reaction steps are observed during the analysis.

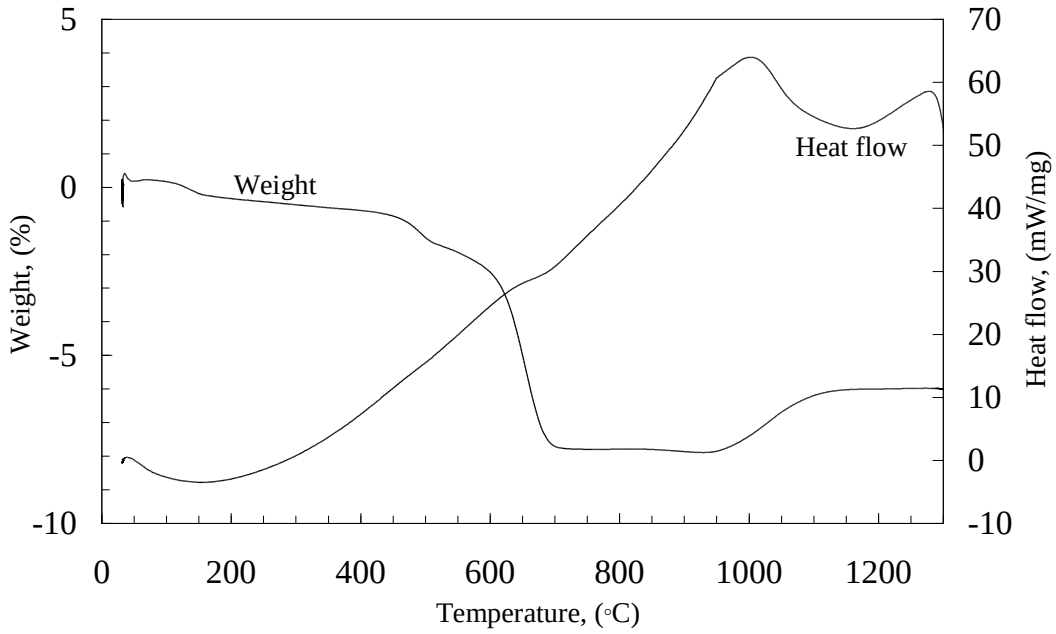


Fig. 2–12 TG/DSC of a loose mixture of reactants (SrO2: Ti: TiO_2 = 1.00: 0.175: 0.825) in oxygen heated at a rate in oxygen heated at rate of 50 ^{o}C/min

The first step is the decomposition of SrO_2 to SrO and O_2 between 350 and 700 °C, similar to the thermal behavior of SrO_2 in isolation (Figure 2–9). The second step is Ti oxidation between 950 and 1150 °C.

The CS reaction can be written as follows:

$$SrO_2 + aTi + (1-a)TiO_2 \rightarrow SrTiO_3 + \frac{(1-2a)}{2} O_2 \qquad (2\text{–}7)$$

In this CS reaction scheme, the Ti powder acts as a fuel, providing the necessary heat to sustain the combustion front movement. SrO_2 serves as both the solid oxidizer and the filler. The oxygen decomposed from SrO_2 oxidized the adjacent Ti powder, making the

reaction less dependent on the oxygen diffusing from the surrounding atmosphere. In Eq. (2–7), *a* denotes the Ti content. TiO_2 was used as a diluent to control the combustion temperature. In this section, *a* was varied from 0.175 to 0.300 in increments of 0.025. The specific heat capacities of reactants and products of Eq. (2–7) are listed in Table 2–3.

Table 2-3 Molar specific heat capacities of the products

Products	Specific heat, C_p [J·mol^{-1}·K^{-1}] $C_p = A + 10^{-3}BT + 10^{5}CT^{-2} + DT^{-1/2} + 10^{-6}ET^{2} + 10^{-9}FT^{3}$						Temperature range [K]	Reference
	A	*B*	*C*	*D*	*E*	*F*		
$SrTiO_3$	134.581	4.5567	-11.979	-414.3	0	0	270-1800	*(15)*
O_2(g)	31.32234	-20.2353	-0.07374	0	57.86644	-36.5062	100-700	*(16)*
O_2(g)	30.03235	8.772972	-7.41599	0	-3.98813	0.788313	700-2000	*(16)*
O_2(g)	20.91111	10.72071	92.45722	0	-2.0205	0.146449	2000-6000	*(16)*

Equation (2–8) was used to calculate the adiabatic temperature of the process.

$$\int_{298}^{T_{ad}} \left(\sum_i n_i C_{pi}\right) dT = -\Delta H_r \qquad (2\text{–}8)$$

In this equation, n_i is the stoichiometric number of product i, i is $SrTiO_3$ and O_2 (g), and C_{pi} is the molar specific heat capacity of the product. The reaction heats and adiabatic temperatures for all a values are listed in Table 2–4.

Table 2–4 Calculated adiabatic temperature (T_{ad}) and heat of reaction (ΔH_r)

a	T_{ad} (°C)	ΔH_r (kJ)
0.175	1876	-259.5
0.200	2044	-283.1
0.225	2213	-306.8
0.250	2383	-330.4
0.275	2554	-354.0
0.300	2725	-377.6

Generally, it has been empirically judged that reactions will not be self-sustaining when T_{ad} is less than 1527 °C (1800 K). It can be seen from Table 2–4 that T_{ad} of the reactions are much higher than 1800 K. Ignition of the sample occurred in about 2 s after the igniter was turned on. The reaction front propagated through the pellet from the ignition region towards the unreacted remainder of the pellet. During the CS reaction, the color of the

pellet changed from light grey to creamy yellow. Synthesized samples with a lower *a* value are more porous and easier to grind. CSed (combustion-synthesized) samples were analyzed by XRD to determine their phases. Figure 2–13 shows the XRD patterns of the synthesized $SrTiO_3$ for a = 0.200, 0.250, and 0.300. All peaks in Figure 2–13 are in good agreement with those obtained for $SrTiO_3$. Unreacted raw materials were not detected in the product, indicating that CS reactions with various *a* values were successful. High-purity $SrTiO_3$ materials were fabricated.

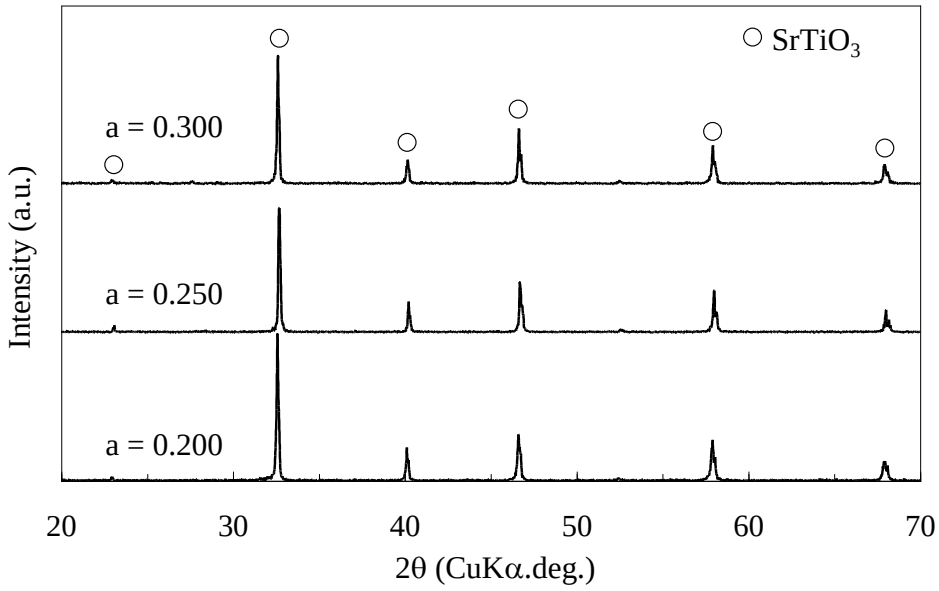


Fig. 2–13 XRD patterns of combustion-synthesized $SrTiO_3$ with different Ti ratios

Figure 2–14 illustrates the temperature profiles at the centerline of the pellet during the CS when *a* is equal to 0.200 and 0.250. The temperature sharply increased to more than 1700 °C and then cooled. This rapid increase in temperature occurred when the

propagation front reached the point at which the thermocouples were inserted. The highest temperatures recorded during CS reactions for a = 0.200 and 0.250 were 1740 °C and 1770 °C, respectively. The peak temperatures for each a value were lower than the calculated adiabatic temperatures as a result of heat loss by convection from the pellet surface. By using two pairs of thermocouples inserted into the centerline of the pellet at a known distance apart, the velocity of the combustion wave was calculated to be 3.69 × 10^{-3} m/s when a = 0.200.

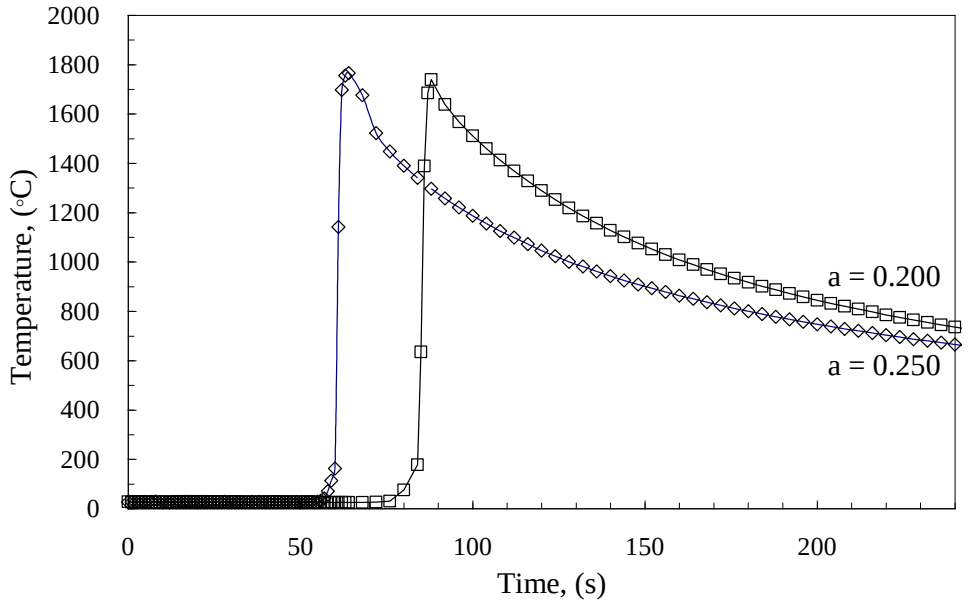


Fig. 2–14 Temperature histories of CS reaction at the centerline of reactant pellet with different Ti ratios

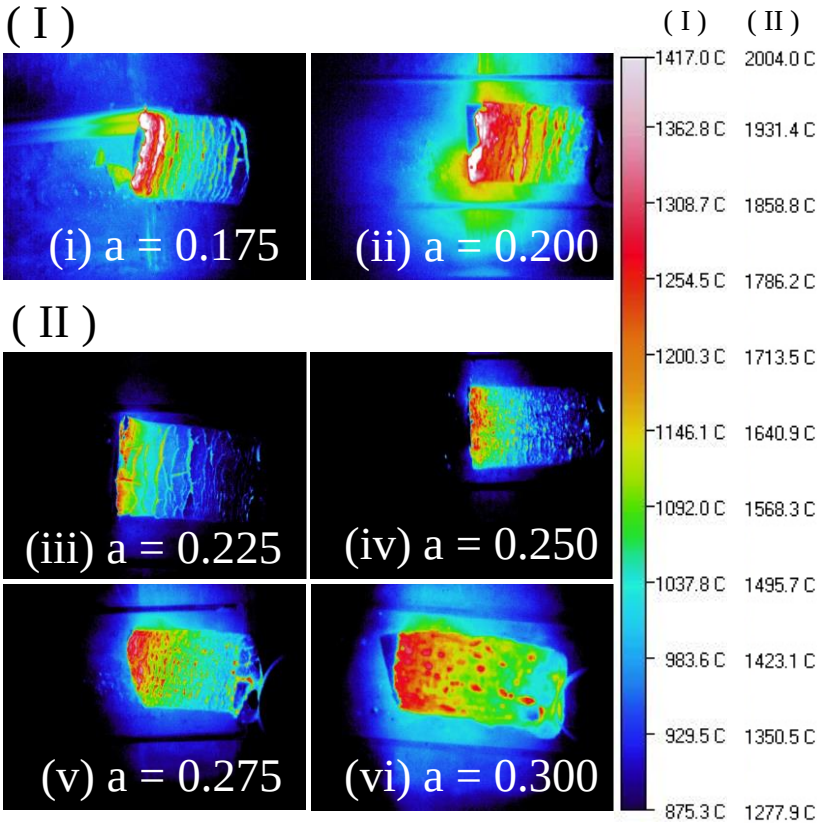


Fig. 2–15 IR thermographical images of reactant pellets during CS reaction with various Ti ratios

Figure 2–15 shows IR thermographic images of the pellet surfaces during CS reactions for various *a* values, showing the temperature distribution at the surface of the pellets. As the *a* value increases, the surface temperature and the high-temperature area increase. The highest temperatures at the surface of the pellet for *a* = 0.200 and 0.250 were around 1400 and 1800 °C, respectively. The internal temperatures of the pellets, as determined by inserted thermocouples, were higher than those at the surface.

The apparent activation energy of the CS reaction can be calculated from TG curves using the Friedman method [34] as follows:

$$ln\left(\frac{d\alpha}{dt}\right) = ln[Af(\alpha)] - \frac{E}{RT} \quad (2–9)$$

where α is the reaction degree, t is the time, A denotes the frequency factor, $f(\alpha)$ is a differential function, E represents the apparent activation energy, R is the gas constant, and T is the absolute temperature. Figure 2–16 shows the Arrhenius plot of the CS reaction for various α values. The apparent activation energy of reaction (2–7) was calculated to be 287.6 kJ/mol. This value is very close to 271 and 268 kJ/mol reported as the kinetics of $SrTiO_3$ formation from $SrCO_3$ and TiO_2 through a solid state reaction [35]. It is pointed out that, from the calculated apparent activation energy of 287.6 kJ/mol, the overall reaction was controlled by the diffusion of Sr^{2+} ions [36].

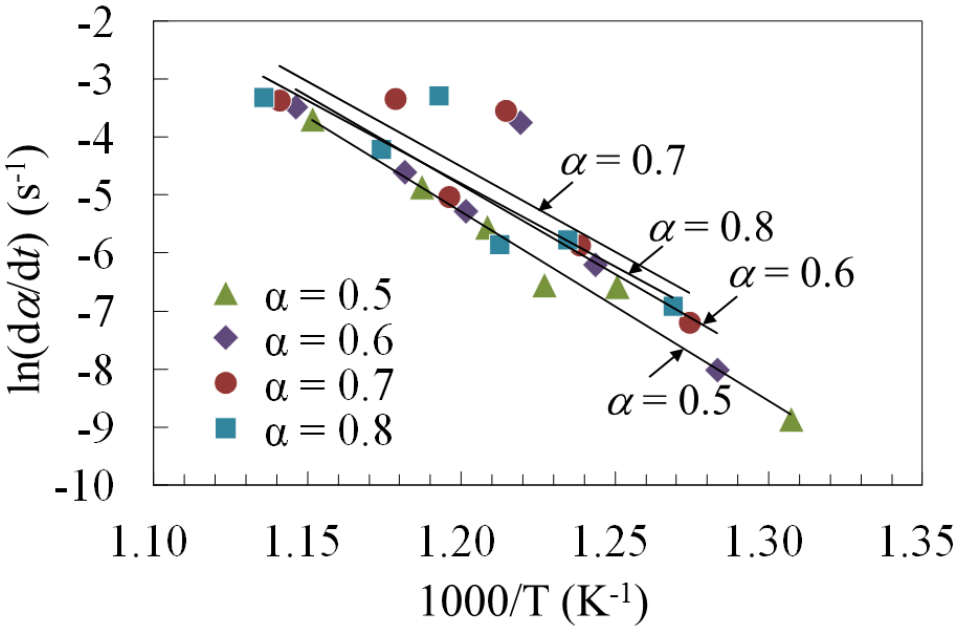


Fig. 2–16 Arrhenius plot of TG data used to calculate apparent activation energy of CS of $SrTiO_3$

2.4.4 Summary

I developed a new CS method of fabricating $SrTiO_3$ powders of high purity without using $NaClO_4$. The following results were obtained.

(1) $SrTiO_3$ was successfully synthesized from SrO_2, TiO_2, and Ti in the absence of $NaClO_4$ at various $Ti/(Ti+TiO_2)$ ratios from 0.175 to 0.300.

(2) TG/DTA measurements were conducted to study the reaction mechanism during the CS of $SrTiO_3$.

(3) The apparent activation energy of the CS reaction was calculated as 287.6 kJ/mol, showing that the overall reaction was controlled by the diffusion of Sr^{2+} ions.

(4) $SrTiO_3$ of high purity was prepared by this new CS process. No detectable amounts of impurities were observed in the synthesized $SrTiO_3$. The results suggest that a one-step CS process without post-heat treatment can be employed to produce commercially available ceramics.

2.5 Conclusions

In Chapter 2, the effects of operating conditions of spark plasma sintering were investigated. The following useful findings were obtained:

(1) Spark- plasma- sintering of $Sr_{0.92}La_{0.08}TiO_3$ was successfully carried out at 1513 to 1633 K in temperature. $Sr_{0.92}La_{0.08}TiO_3$ powders were not sintered well at 1663 K due to the formation of many intercrystalline cracks.

(2) High-temperature sintering resulted in introduction of a lot of oxygen defects which produced electrons as carriers. Thus, samples sintered at higher temperature showed large electric conductivity. However, high-temperature sintering also caused an increase in thermal conductivity because of the increase in average grain size, therefore the most optimum sintering temperature maximized ZT was 1573 K.

(3) With increasing temperature, ZT showed an increasing tendency and showed peaks at around 1000 K. The maximum ZT of 0.16 at 1005 K was obtained from the sample sintered at 1573 K.

(4) Prolonged sintering introduced more oxygen defects into the sample, which can produce carrier electrons. Thus, samples sintered for longer times, except for the sample sintered for 15 min, showed higher electrical conductivities.

(5) Prolonged sintering increased the grain size of the samples, which caused higher thermal conductivities.

(6) The sample sintered for only 5 min recorded the maximum *ZT* value of 0.37 at 1045 K. This is the largest value reported thus far for $SrTiO_3$-based bulk semiconductors.

(7) Bulk densities of sintered samples varied from 4.98 $g \cdot cm^{-3}$ of 95.0 %T.D. to 5.14 $g \cdot cm^{-3}$ of 98.1 %T.D., when sintering was carried out under the same conditions of heating rate of 30 $K \cdot min^{-1}$ at 1573 K for 5 min.

(8) Samples showed larger displacement during sintering became dense and showed higher electric conductivity.

(9) $SrTiO_3$ was successfully synthesized from SrO_2, TiO_2, and Ti in the absence of $NaClO_4$ at various $Ti/(Ti+TiO_2)$ ratios from 0.175 to 0.300.

(10) TG/DTA measurements were conducted to study the reaction mechanism during the CS of $SrTiO_3$.

(11) The apparent activation energy of the CS reaction was calculated as 287.6 kJ/mol, showing that the overall reaction was controlled by the diffusion of Sr^{2+} ions.

(12) $SrTiO_3$ of high purity was prepared by this new CS process. No detectable amounts of impurities were observed in the synthesized $SrTiO_3$. The results suggest that a one-step CS process without post-heat treatment can be employed to produce commercially available ceramics.

2.6 References

[1] Lihua Zhang, Tsuyoshi Tosho, Noriyuki Okinaka, Tonohiro Akiyama. (2007). Thermoelectric Properties of Combustion-Synthesized Lanthanum-Doped Strontium Titanate. *Mater. Trans.*, *48,* 1079-1083.

[2] Hiroaki Muta, Ken Kurosaki, Shinsuke Yamanaka. (2004). Thermoelectric properties of doped BaTiO3–SrTiO3 solid solution *J. Alloy. Compd.*, *368,* (1-2), 22-24.

[3] Takuji Maekawa, Ken Kurosaki, Hiroaki Muta, Masayoshi Uno, Shinsuke Yamanaka. (2005). Thermoelectric properties of perovskite type strontium ruthenium oxide *J. Alloy. Compd.*, *387,* (1-2), 56-59.

[4] Hiroaki Muta, Ken Kurosaki, Shinsuke Yamanaka. (2005). Thermoelectric properties of reduced and La-doped single-crystalline SrTiO3. *J. Alloy. Compd.*, *392,* (1-2), 306-309.

[5] H. Yukawa, K. Nakatsuka, M. Morinaga. (1999). Electronic structures of hydrogen in perovskite-type oxide, SrTiO3. *Solid State Ionics*, *116,* (1-2), 89-98.

[6] Jaehoon Rho, Eunjip Choi. (2011). Evidence of the primary-color photoluminescence in ion (H+,H2+,C-) irradiated and thermal annealed SrTiO3. *J. Lumin.*, *131,* (1), 69-71.

[7] T. Okuda, K. Nakanishi, K. Yamanaka. (2001). Large thermoelectric response of metallic perovskites: Sr1-xLaxTiO3 (0<x<0.1). *Phys. Rev. B Mat.*, *63,* 113104-113101.

[8] Hiroaki Muta, Ken Kurosaki, Shinsuke Yamanaka. (2003). Thermoelectric properties of rare earth doped SrTiO3. *J. Alloy. Compd.*, *350,* (1-2), 292-295.

[9] H. Obara, A. Yamamoto, C. H. Lee, K. Kobayashi, A. Matsumoto, R. Funahashi. (2004). Thermoelectric Properties of Y-Doped Polycrystalline SrTiO3. *Jpn. J. Appl. Phys.*, *43,* 540-542.

[10] S. Ohta, T. Nomura, H. Ohta, M. Hirano, H. Hosono, K. Koumoto. (2005). Large thermoelectric performance of heavily Nb-doped SrTiO3 epitaxial film at high temperature. *Jpn. J. Appl. Phys.*, *87,* 092108-092101-092103.

[11] S. Ohta, T. Nomura, H. Ohta, K. Koumoto. (2005). High-temperature carrier transport and thermoelectric properties of heavily La- or Nb-doped SrTiO3 single crystals. *Jpn. J. Appl. Phys.*, *97,* 034106-034101–034106-034104.

[12] P. Balaya, M. Ahrens, M. L. Kienle, J. Maier, B. Rahmati, S. B. Lee, W. Sigle. (2006). Synthesis and characterization of nanocrystalline SrTiO3. *J. Am. Ceram. Soc.*, *89,* 2804.

[13] A. J. Zhou, T. J. Zhu, X. B. Zhao. (2006). Thermoelectric properties of perovskite-type oxide La1-xSrxCoO3 (x = 0, 0.1) prepared by solid state reactions. *Mater. Sci. Eng. B*, *128,* (1-3), 174-178.

[14] N. V. Nong, Chia-Jyi Liu, M. Ohtaki. (2011). High-temperature thermoelectric properties of late rare earth-doped Ca3Co4O9+[delta]. *Journal of Alloys and Compounds*, *509,* (3), 977-981.

[15] L. H. Yin, R. Ang, L. J. Li, B. C. Zhao, Y. K. Fu, X. B. Zhu, Z. R. Yang, W. H. Song, Y. P. Sun.

(2011). Thermoelectric properties of sol-gel derived cobaltite Bi2Ca2.4Co2Oy. *Physica B: Condensed Matter*, *406,* (14), 2914-2918.

[16] Peng-Peng Shang, Bo-Ping Zhang, Jing-Feng Li, Ning Ma. (2010). Effect of sintering temperature on thermoelectric properties of La-doped SrTiO3 ceramics prepared by sol-gel process and spark plasma sintering. *Solid State Sciences*, *12,* (8), 1341-1346.

[17] Chia-Jyi Liu, Pradipta K. Nayak, Yong-Zhi Chen. (2009). A simple approach of fabricating thermoelectric [gamma]-NaxCoO2 and superconductive Nax(H2O)yCoO2-[delta] films using the sol-gel spin-coating method. *Thin Solid Films*, *518,* (1), 91-93.

[18] Lihua Zhang, Tsuyoshi Tosho, Noriyuki Okinaka, Tomohiro Akiyama. (2007). Thermoelectric Properties of Combustion Synthesized and Spark Plasma Sintered Sr1－xRxTiO3 (R=Y, La, Sm, Gd, Dy, $0 \leq x \leq 0.1$). *Mater. Trans.*, *48,* (8), 2088-2093.

[19] H. Simizu, M. Yoshinaka, K. Hirota. (2002). Fabrication and mechanical properties of monolithic MoSi2 by spark plasma sintering. *Mater. Res. Bull.*, *37,* 1557-1563.

[20] T. Nishimura, M. Mitomo, H. Hirotsuru, M. Kawahara. (1995). Fabrication of silicon nitride nano-ceramics by spark plasma sintering. *J. Mater. Sci. Lett.*, *14,* 1046-1047.

[21] I. J. Shon, Z. A. Munir, K. Yamazaki, K. Shoda. (1996). Simultaneous Synthesis and Densification of MoSi2 by Field-Activated Combustion. *J. Am. Ceram. Soc.*, *79,* (7), 1875-1880.

[22] J. J. Petrociv, R. E. Honnell. (1990). Partially stabilized ZrO2 particle-MoSi2 matrix composites. *J. Mater. Sci.*, *25,* (10), 4453-4456.

[23] Y. Liu, Y. Lin, Z. Shi, C. -W. Nan, Z. Shen. (2005). Preparation of Ca3Co4O9 and Improvement of its Thermoelectric Properties by Spark Plasma Sintering. *J. Am. Ceram. Soc.*, *88,* 1337-1340.

[24] Y. -H. Lin, Z. Shi, C. -W. Nan, Y. Liu, J. Li. (2007). High-Temperature Electrical Transport and Thermoelectric Power of Partially Substituted Ca3Co4O9-Based Ceramics. *J. Am. Ceram. Soc.*, *90,* 132-136.

[25] H. Ishikawa, K. Oohira, T. Nakajima, Tomohiro Akiyama. (2008). Combustion synthesis of SrTiO3 using different raw materials. *J. Alloys Compd.*, *454,* 384-388.

[26] Q. Hu, P. Luo, Y. Yao. (2008). Influence of spark plasma sintering temperature on sintering behavior and microstructure of bulk MoSi2. *J. Alloy. Compd.*, *459,* 163-168.

[27] X. Dong, F. Lti, L. Yang, Y. Zhang, X. Wang. (2008). Influence of spark plasma sintering temperature on electrochemical performance of La0.80Mg0.20Ni3.75 alloy. *Mater. Chem. Phys.*, *112,* 596-602.

[28] R. -C. Chang, S. -Y. Chu, Y. -P. Wong, C. -S. Hong, H. -H. Huang. (2008). The effect of sintering temperature on the properties of lead-free (Na0.5K0.5)NO3－SrTiO3 ceramics. *J. Alloy. Compd.*, *456,* 308-312.

[29] Y. Zhao, L. -J. Wang, G. -J. Zhang, W. Jiang, L. -D. Chen. (2009). *Int. J. Refract. Met. Hard Mater.*, *27,* 177.

[30] Manshi Ohyanagi, Mitsue Koizumi. (1994). Simultaneous Combustion Synthesis and

Sintering of Diamond Dispersed Ceramics Composite Materials. *J. Soc. Mat. Sci. Japan*, *43,* (493), 1379-1380.

[31] E. M. Carrillo-Heian, C. Unuvar, J. C. Gibeling, G. H. Paulino, Z. A. Munir. (2001). Simultaneous synthesis and densification of niobium silicide/niobium composites. *Scripta Materialia*, *45,* (4), 405-412.

[32] O. Yamada, M. Hachiya, S. Nakane, M. Yoshinaka, K. Hirota, O. Yamaguchi. (1999). Simultaneous synthesis and sintering of alpha-Ti(N) by self-propagating high-temperature combustion under nitrogen pressure. *Journal of Materials Science Letters*, *18,* (5), 363-365.

[33] Asami Kikuchi, Lihua Zhang, Noriyuki Okinaka, Tsuyoshi Tosho, Tomohiro Akiyama. (2009). Effects of Sintering Temperature on Thermoelectric Device of La-Doped Strontium Titanate in the Combination of Combustion Synthesis and Spark Plasma Sintering. *Mater. Trans.*, *50,* (11), 2675-2679.

[34] H.L. Friedman. (1964). Kinetics of thermal degradation of char-forming plastics from thermogravimetry. *J. Polym. Sci., Part A-Polymer Symposium*, *6,* 183-195.

[35] Luo Shiyong, Zhang Jiayun, Wang Ning. (2006). Kinetics of Strontium Titanate Formation from Solid State Reaction between Strontium Carbonate and Anatase. *High Temperature Materials and Processes*, *26,* (1), 33-42.

[36] Luis Amaral, Ana M. R. Senos, Paula M. Vilarinho. (2009). Sintering kinetic studies in nonstoichiometric strontium titanate ceramics. *Mater. Res. Bull.*, *44,* 263-270.

Chapter 3

Energy conservative preparation for thermoelectric Fe_2VAl

3.1 Introduction

Fe_2VAl [1-5] is a promising candidate for thermoelectric semiconductors due to its rich resources, good mechanical strength, and high electrical response. The arc-melting method [3-5] and the solid-state reaction [6] are the major methods of fabricating Fe_2VAl. However, Fe_2VAl prepared by these conventional fabricating methods sometimes require additional heat treatment to achieve homogenization, which lead to energy- and time-consuming. In these conventional methods, metals powders with high purity are used, resulting in high costs of the final products. These problems of being time-, energy-, and cost-intensive are major issues which prevent Fe_2VAl thermoelectrics from widespreading.

Thermite reaction [7] is a major solid-state combustion methods which uses a highly exothermic reaction between metal powders and oxides in raw materials. Particularly, thermite reaction using Al as a strong reducing agent is called aluminothermic reduction and utilized for many industrial manufacturing processes such as vanadium refining process [8, 9]. With thermite reaction including aluminothermic reduction, external energy supply is only needed for a few seconds during ignition. However, a large amount of heat discharged from the reduction

reactions is left unused and emitted into the atmosphere. This suggests that there is still great potential for efficient energy utilization. The use of thermite reactions, instead of an external energy/heat supply, is quite attractive from the viewpoint of efficient usage of energy. Moreover, thermite synthesis enables inexpensive oxides to be utilized in place of expensive pure metals, resulting in inexpensive products. Compared to conventional methods, the great benefits of proposed thermite synthesis for Fe_2VAl are the availability of metal oxides as raw materials, efficient utilization of exothermic heat, and inexpensive product due to the former reasons. Meanwhile, possible disadvantage of the proposed thermite synthesis is the increase in the amount of aluminum.

The conventional estimation of energy consumption is based on the first law of thermodynamics. An energy analysis on the basis of the principle of conservation of energy essentially accounts of the in-flowing and out-flowing energies. The out-flowing energy can be fallen apart into products and wastes. Efficiencies are often assessed as ratios of energetic quantities, and often used to evaluate and compare various systems. However, energy efficiencies are not always absolute measures of how ideal systems they are. Furthermore, the thermodynamic losses (energy and material losses) within a system are not assessed with energy analysis and the results of energy analysis may show the technological efficiency differ from the actual efficiency. On the other hand, exergy analysis [10-12] permits lots of disadvantages of energy analysis. The exergy analysis is an evaluation method based on the second law of thermodynamics which supplies an alternative method of evaluating and comparing several systems. The exergy analysis is a very strong way to identify the causes, positions, and magnitudes of process inefficiencies. The concept of exergy has been widely applied to evaluate various systems [13-15] in which the qualitative loss of

energy is expressed by the exergy loss (*EXL*) in each process. Therefore, the purpose of this chapter is to study new synthesis methods using thermite reactions for obtaining Fe_2VAl and to compare new methods with the conventional arc-melting method, using thermodynamic theory for system analysis and focusing on enthalpy and exergy.

3.2 Theory

The enthalpy–exergy diagram, which was originally proposed and named the thermodynamic compass by M. Ishida, C.-C. Chunag [16], is an innovative method for graphically designing a chemical/thermal process. In this research, it is employed for the analysis of the three methods to produce Fe_2VAl because of its simplicity. Details of this concept were explained by M. Ishida, C.-C. Chunag [16], T. Akiyama et al. [17], and M. Yamamoto et al. [18], thus only its framework is explained here. The enthalpy and exergy of a material at temperature *T* and constant pressure can be calculated by the following equations:

$$H = mC_{p,s}(T_m - T_0) + mQ_L + mQ_{p,l}(T - T_m) \text{ and} \tag{3–1}$$

$$\varepsilon = mC_{p,s}\left\{(T_m - T_0) - T_0 \ln\left(\frac{T_m}{T_0}\right)\right\} + mQ_L\left(1 - \frac{T_0}{T_m}\right) + mC_{p,l}\left\{(T - T_m) - T_m \ln\left(\frac{T}{T_m}\right)\right\}. \tag{3–2}$$

In the case of an objective system accompanied by a chemical reaction at T and constant pressure, the chemical reaction can be expressed as:

$$v_A A + v_B B \longrightarrow v_C C + v_D D \tag{3–3}$$

The ΔH and $\Delta\varepsilon$ of the system can be calculated using Equations (3–1) and (3–2) as follows:

$$\Delta H = \sum \upsilon_p H_p - \sum \upsilon_r H_r. \text{ and} \quad (3\text{–}4)$$

$$\Delta\varepsilon = \sum \upsilon_p(\varepsilon_p^0 + \varepsilon_p) - \sum \upsilon_r\,(\varepsilon_r^0 + \varepsilon_r). \quad (3\text{–}5)$$

The standard chemical exergy, ε^0, is a reference value based on a fixed environmental state; that is, 298.15 K, 0.1 MPa, and a steam-saturated air composition (N_2: 78.57 kPa, O_2: 20.61 kPa, H_2O: 3.20 kPa, CO_2, 0.03 kPa, Ar: 0.91 kPa). Note that as the reaction occurred in a standard state, the following equation must be true:

$$\Delta\varepsilon^0 = \Delta G^0. \quad (3\text{–}6)$$

In evaluating a system thermodynamically, summations of ΔH and $\Delta\varepsilon$ in each process are restricted by *the first and second laws of thermodynamics*, as expressed in the following equations:

$$\sum \Delta H = 0 \quad \text{and} \quad (3\text{–}7)$$

$$\sum \Delta\varepsilon \leq 0. \quad (3\text{–}8)$$

An individual process can be expressed as a vector (ΔH, $\Delta\varepsilon$) in the thermodynamic compass. Then the system is simply evaluated by the resultant vector of all the processes on the Δε axis (y-axis). According to *the first and second laws of thermodynamics,* the resultant vector must be a downward or a zero vector. For each vector in a process, the ratio of $\Delta\varepsilon$ to ΔH gives the slope, called the energy level, *A*, indicating energy quality. In particular, the energy level of thermal energy is simply

expressed by the following equation when specific heat is assumed to be constant:

$$A = \frac{T - T_0}{T}. \tag{3–9}$$

By using the thermodynamic compass, the possibility of a system can be determined very easily because the direction of the resultant vector must always be located on the $\Delta\varepsilon$ axis (y-axis) with a negative value, and the length of vertical vector corresponds to net exergy consumption. To promoting the efficient utilization of energy, the system should have a shorter resultant vector.

3.3 System Definition

3.3.1 Conventional arc-melting method

At present, the arc-melting method is the most commonly used conventional method for preparing Fe_2VAl. Therefore, it is analyzed for comparison purposes in this chapter. Figure 3–1 shows a material flow chart for the conventional arc-melting method to produce Fe_2VAl. The flow charts of the Al_2O_3 production process (the Bayer process) and the V refining process were quoted from Ullmann's Encyclopedia of Industrial Chemistry [19]. The Fe in the raw materials is generally manufactured in steelworks from iron ore and coals, the Al is manufactured by the Bayer process (*2 in Fig. 3–1) followed by the Hall–Héroult process (*3 in Fig. 3–1), and the V is manufactured by the aluminothermic reduction through V_2O_5 from vanadinite ore. Commercially available high–purity metal powders of Fe, Al, and V are mixed and then arc-melted. They are then heated for several hours for homogenization.

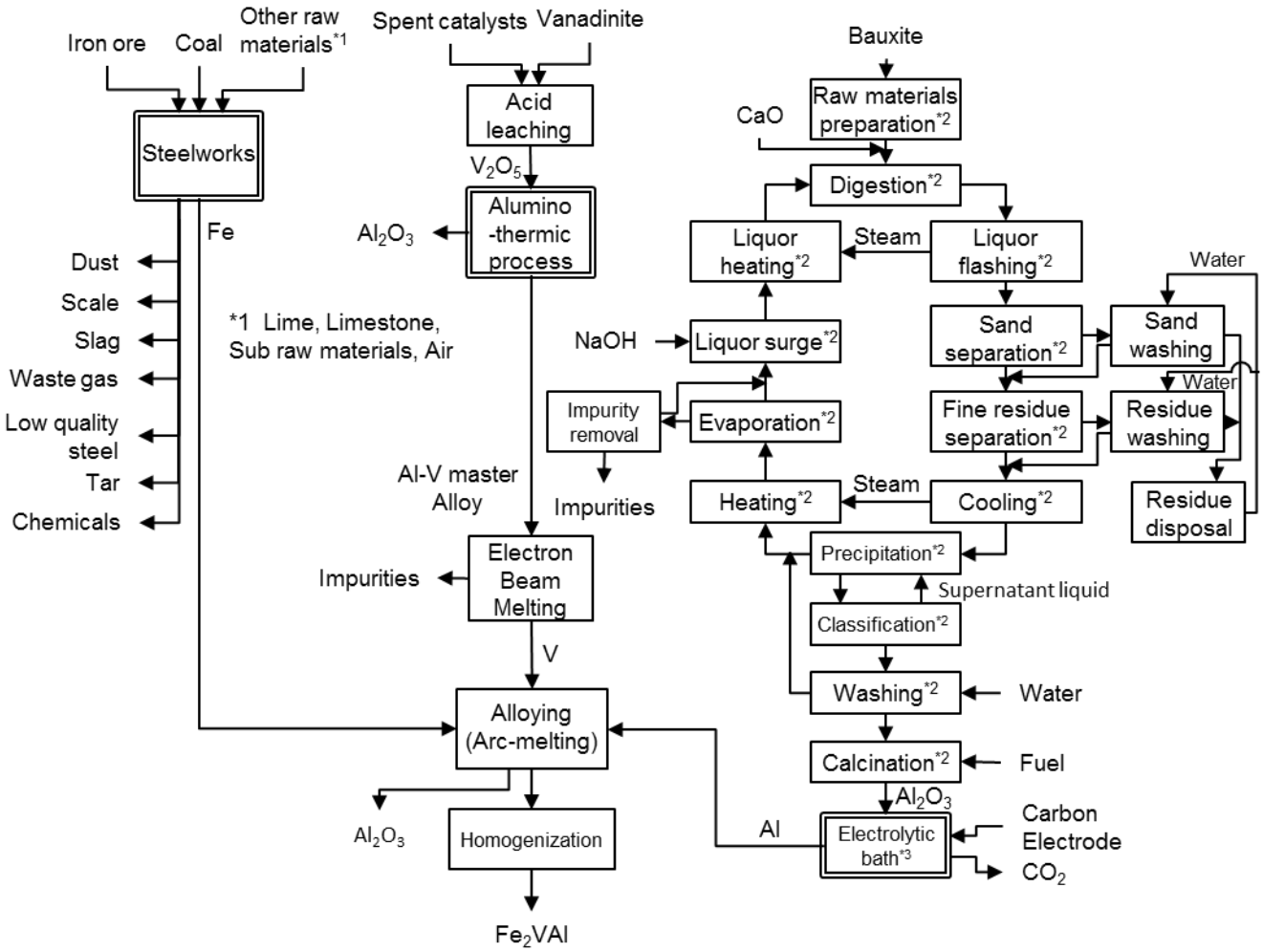


Fig. 3–1 Flow chart for the conventional arc-melting method to produce Fe_2VAl. The flow charts for refining Al and V were quoted from Ullmann's Encyclopedia of Industrial Chemistry [19]. The Bayer process and the Hall–Héroult process for refining Al are presented in the stages labeled *2 and *3, respectively

According to Akiyama et al. [17], the five core processes to produce carbon steel are: reduction, complete combustion, partial combustion, hot metal production with 4.8% carbon, and slag by-production with 43CaO-3SiO_2-15Al_2O_3-7MgO gangue and ash. Carbon-based ironmaking methods can be summarized as:

(i) Carbon-based ironmaking:

$$Fe_2O_3 + C \rightarrow \{Fe(952kg) + C(48kg)\} + \text{slag} + CO_2 + CO$$

$$\begin{pmatrix}\Delta H\\ \Delta\varepsilon\end{pmatrix} = \begin{pmatrix}0\\ -1458\end{pmatrix} \text{(Units; MJ/t-hot metal)}$$

In addition, decarburization and oxygen production are also significant processes for producing pure Fe. Here, gas produced from decarburization was assumed to be 100% CO for simplicity. Decarburization and oxygen production can be expressed as:

(ii) Decarburization:

$$\{Fe(952kg, 1783K) + C(48kg, 1783K)\} + 2000O_2(298K)$$
$$\rightarrow \text{Fe}(952\text{kg}, 298\text{K}) + 4000\text{CO}(298\text{K})$$

$$\begin{pmatrix}\Delta H\\ \Delta\varepsilon\end{pmatrix} = -\begin{pmatrix}2323\\ 2069\end{pmatrix}J - 2000\begin{pmatrix}0\\ 0.94\end{pmatrix}J + \begin{pmatrix}1682\\ 1500\end{pmatrix}J + 4000\begin{pmatrix}67.59\\ 65.81\end{pmatrix}J$$
$$= \begin{pmatrix}1129\\ 1091\end{pmatrix}J \text{ (Units; MJ)}$$

(iii) Oxygen production:

$$Air(O_2 + 3.72N_2 + 0.155H_2O + 0.0146CO_2 + 0.442Ar)$$

$$\rightarrow \text{Air without } O_2 + (3.72N_2 + 0.155H_2O + 0.0146CO_2 + 0.442Ar)$$

$$\begin{pmatrix}\Delta H\\ \Delta\varepsilon\end{pmatrix} = -\begin{pmatrix}0\\0\end{pmatrix}J + \begin{pmatrix}0\\0.94\end{pmatrix}J = \begin{pmatrix}0\\3.93\end{pmatrix}J \text{ (Units; kJ)}$$

Therefore, a system of steelworks can be defined as combination of three processes from (i) to (iii).

The Hall–Héroult process in an Al manufacturing system can be expressed as:

(iv) Hall–Héroult process:

$$\frac{1}{2}Al_2O_3 + \frac{3}{4}C = Al + \frac{3}{4}CO_2$$

$$\begin{pmatrix}\Delta H\\ \Delta\varepsilon\end{pmatrix} = \begin{pmatrix}543\\495\end{pmatrix} \text{ (Units; kJ)}$$

The thermite synthesis of V and the cooling process of V in a V manufacturing system can be described by:

(v) Thermite synthesis of V:

$$\frac{1}{2}V_2O_5 + \frac{5}{3}Al = V(2183K) + \frac{5}{6}Al_2O_3(2183K)$$

$$\begin{pmatrix}\Delta H\\ \Delta\varepsilon\end{pmatrix} = \begin{pmatrix}-432\\-479\end{pmatrix} \text{ (Units; kJ)}$$

(vi) Cooling of V:

$$V(2183\text{K}) \rightarrow V(298\text{K})$$

$$\begin{pmatrix}\Delta H \\ \Delta \varepsilon\end{pmatrix} = \begin{pmatrix}-64.4 \\ -47.3\end{pmatrix} \text{ (Units; kJ)}$$

Since the alloying of Fe_2VAl requires heat for the melting process, the heat must be compensated by an external energy/heat supply in the case of arc-melting. The necessary enthalpy and exergy for alloying Fe_2VAl were calculated on the assumption that the necessary enthalpy and exergy are equal to that needed to melt all reactants. Alloying Fe_2VAl with commercially available high-purity metal powders of Fe, V, and Al can be described by:

(vii) Alloying (arc-melting):

$$2Fe + V + Al \rightarrow Fe_2VAl$$

$$\begin{pmatrix}\Delta H \\ \Delta \varepsilon\end{pmatrix} = \begin{pmatrix}246 \\ 151\end{pmatrix} \text{ (Units; kJ)}$$

A system of conventional arc-melting is, therefore, defined as combination of processes from (i) to (vii).

Figure 3–2 shows system diagrams of the processes of the conventional arc-melting method to produce Fe_2VAl. Dotted lines, solid arrows, white arrows, and solid circles indicate the system boundary, material flows, intermediary energy flows,

and a process, respectively. The conventional arc-melting system consists of four independent subsystems for steelworks, the Hall–Héroult process (aluminum production), vanadium production, and alloying (arc-melting).

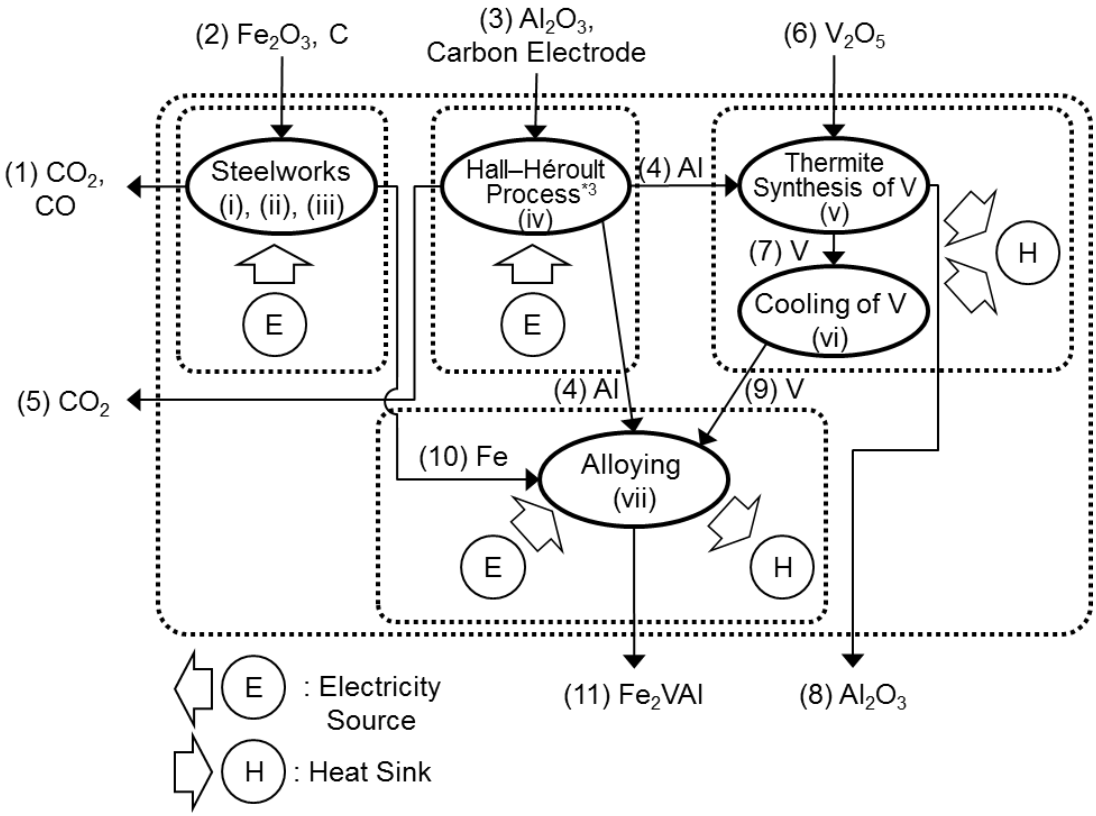
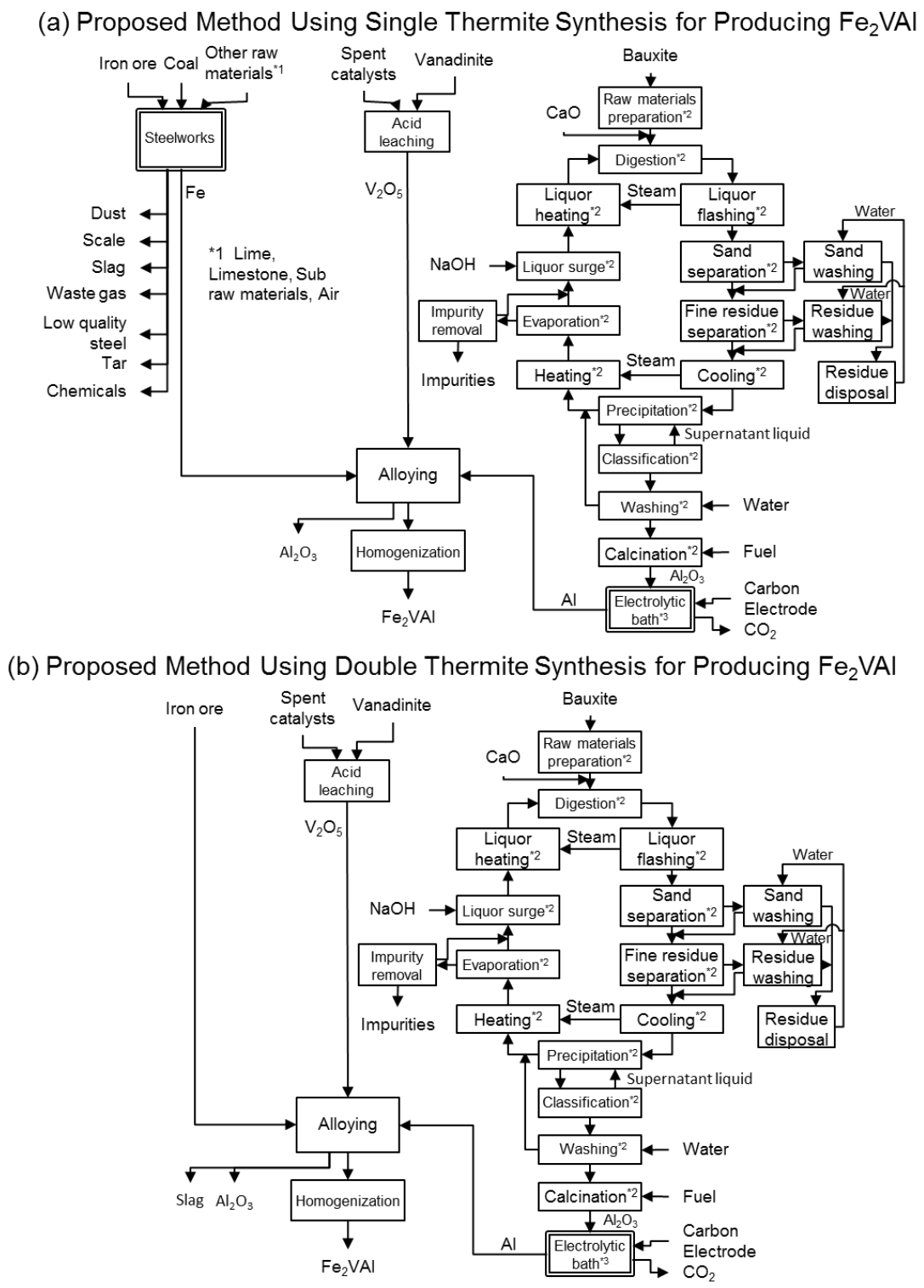


Fig. 3–2 Diagram of processes of the conventional arc-melting method to produce Fe_2VAl. The dotted lines, solid arrows, white arrows, and solid circles indicate the system boundary, material flows, intermediary energy flows, and a process, respectively

3.3.2 Single thermite synthesis

To produce Fe_2VAl via thermite reactions, thermite synthesis of V should be the core reaction, wherein the V and Al sources have to be supplied in the form of V_2O_5 and Al, respectively. With surplus Al to the stoichiometry of Equation (v), V_2O_5 becomes reduced by Al, some Al (by the stoichiometry of Equation (v)) is oxidized and becomes Al_2O_3, while the remaining surplus Al has no involvement in the thermite reaction and becomes diffused in molten V as a constituent element. However, the Fe source can be supplied in both metal Fe and Fe_2O_3 forms, because Fe is not involved with the thermite synthesis of V. In the case of using Fe, the reaction can be initiated by the exothermic heat discharged from thermite synthesis of V. The Fe and surplus Al are diffused in the molten V and then became a Fe_2VAl alloy. Meanwhile, with Fe_2O_3, alloying can be triggered by reaction heat from the thermite synthesis of both V and Fe, where V_2O_5 and Fe_2O_3 are reduced by Al and become V and Fe, respectively. In other words, the two thermite reactions of V_2O_5 and Fe_2O_3 drive the alloying process. In addition, surplus Al has to be supplied to be the constituent element. In this chapter, former system using Fe is named as “single thermite synthesis”, and the latter system with Fe_2O_3 is named as “double thermite synthesis”. Figures 3-3 show the material flow charts of proposed methods using (a) single thermite synthesis and (b) double thermite synthesis, respectively.



Figs. 3–3 Material flow charts for the proposed methods using (a) single thermite synthesis and (b) double thermite synthesis. Material flows of Al and V refining were quoted from Ullmann's Encyclopedia of Industrial Chemistry [19]. The Bayer process and Hall–Héroult process for refining Al are presented in the stages labeled *2 and *3, respectively

The critical difference between the conventional arc-melting method and single thermite synthesis is the timing of the alloying reaction. In the case of single thermite synthesis proposed in this chapter, the thermite synthesis of V and alloying can proceed simultaneously, resulting in a large amount of heat discharged from the thermite reaction of V that can be utilized to efficiently alloy Fe_2VAl, as shown in Figures 3–3(a), by premixing Fe and surplus Al in the raw materials in advance. Alloying to obtain Fe_2VAl via single thermite synthesis can be described by:

(viii) Alloying (single thermite synthesis):

$$2Fe + V(2183K) + Al \rightarrow Fe_2VAl$$

$$\begin{pmatrix} \Delta H \\ \Delta \varepsilon \end{pmatrix} = \begin{pmatrix} 181 \\ 104 \end{pmatrix} \text{ (Units; kJ)}$$

The single thermite synthesis process is, therefore, defined as a combination of processes of (i) to (v), and (viii).

3.3.3 Double thermite synthesis

In double thermite synthesis, the alloying process and the two thermite reactions of V_2O_5 and Fe_2O_3 proceed simultaneously, which results in a larger amount of heat discharged from two thermite reactions that can be utilized. The thermite synthesis of Fe and alloying to obtain Fe_2VAl by double thermite synthesis can be expressed by:

(ix) Thermite synthesis of Fe:

$$\frac{1}{2}Fe_2O_3 + Al = Fe + \frac{1}{2}Al_2O_3$$

$$\binom{\Delta H}{\Delta \varepsilon} = \binom{-426}{-421}$$ (Units; kJ)

(x) Alloying (double thermite synthesis)

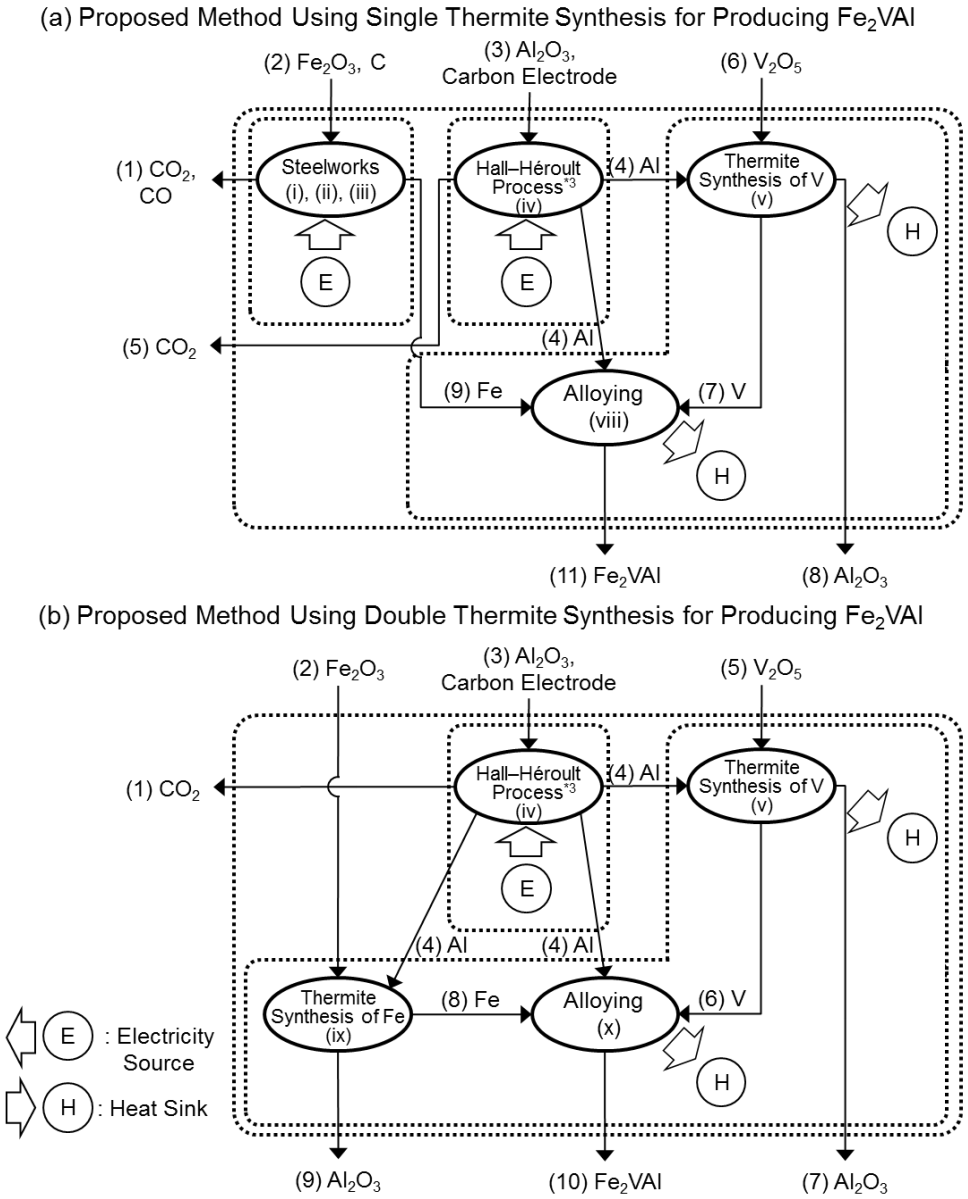
$$2Fe(1811K) + V(2183K) + Al \rightarrow Fe_2VAl$$

$$\binom{\Delta H}{\Delta \varepsilon} = \binom{56.6}{38.7}$$ (Units; kJ)

A system of double thermite synthesis is, therefore, defined as combination of processes of (iv), (v), (ix), and (x). All values of H and ε in (i) to (x) are evaluated from reliable thermodynamic data.

Figures 3–4 show process system diagrams of the processes of the proposed methods using (a) single thermite synthesis, and (b) double thermite synthesis. The single thermite synthesis system is made up of three independent subsystems for steelworks, the Hall-Héroult process (aluminum production), and vanadium production combined with alloying (single thermite synthesis), while the double thermite synthesis is made up of two independent subsystems for the Hall-Héroult process (aluminum production), and vanadium production combined with iron production and alloying (double thermite synthesis). The alumina production process and the V_2O_5 production process were not considered in the evaluation of the conventional arc-melting system and the two proposed methods under the same conditions, as these processes are common to all three methods. The mass of Fe_2VAl crossing the system boundary to the

outside was also equalized.



Figs. 3–4 System diagrams of the processes of the proposed methods using (a) single thermite synthesis and (b) double thermite synthesis

Table 3–1 lists the assumed temperatures of the in- and out- flowing materials in each system.

Table 3–1 Assumed temperature of the in- and out-flowing materials in each system

Arc melting			Single thermite synthesis			Double thermite synthesis		
No.	Materials	T (K)	No.	Materials	T (K)	No.	Materials	T (K)
(1)	CO_2	298	(1)	CO_2	298	(1)	CO_2	298
	CO	298		CO	298	(2)	Fe_2O_3	298
(2)	Fe_2O_3	298	(2)	Fe_2O_3	298	(3)	Al_2O_3	298
	C	298		C	298		Carbon Electrode	298
(3)	Al_2O_3	298	(3)	Al_2O_3	298	(4)	Al	298
	Carbon Electrode	298		Carbon Electrode	298	(5)	V_2O_5	298
(4)	Al	298	(4)	Al	298	(6)	V	2183
(5)	CO_2	298	(5)	CO_2	298	(7)	Al_2O_3	2183
(6)	V_2O_5	298	(6)	V_2O_5	298	(8)	Fe	1811
(7)	V	2183	(7)	V	2183	(9)	Al_2O_3	1811
(8)	Al_2O_3	2183	(8)	Al_2O_3	2183	(10)	Fe_2VAl	298
(9)	V	298	(9)	Fe	298			
(10)	Fe	298	(10)	Fe_2VAl	298			
(11)	Fe_2VAl	298						

3.4 Results and discussion

The thermodynamic compass of the conventional arc-melting system is shown in Figure 3–5. The vectors of (iv) the Hall–Héroult process and the corresponding electric power, shown as white circles, have a unit of 10 kJ per 1 mol of Fe_2VAl. In the case of conventional arc-melting, the vectors of (ii) Decarburization, (iv) the Hall–Héroult process, and (vii) Alloying of Fe_2VAl are placed in the first quadrant and their slopes are less than 1, which means that these three processes are heat-receiving processes. The vectors of (v) Thermite Synthesis of V and (vi) Cooling of V are in the third quadrant. The slope of vector (v) is greater than 1 and that of vector (vi) is less than 1, showing that process (v) is a mixing process and that process (vi) is a heat-giving process. The sum of vectors of (i) to (vii), and the corresponding electric power and heat sink, is expressed by a white arrow, directed downward on the y-axis, which obeys the second law of thermodynamics, Eq. (3–8). The length of the white vector, 808 kJ/mol-Fe_2VAl, indicates the total *EXL* of the system.

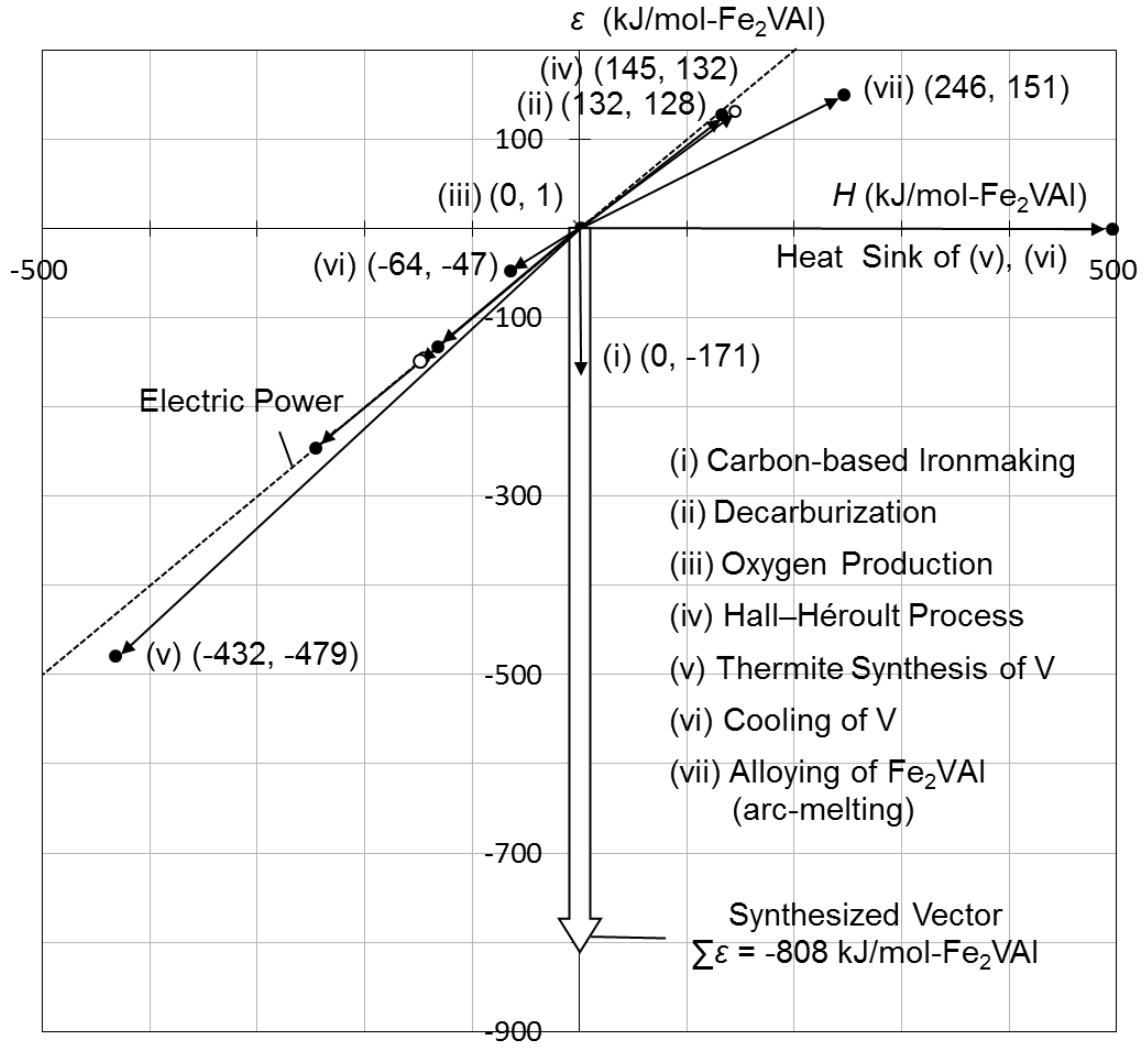


Fig. 3–5 An enthalpy–exergy diagram showing vectors of each phenomenon in the conventional arc-melting method to produce Fe_2VAl. The vectors of (iv) and the corresponding electric power, shown as white circles, have a scale of 10 kJ/mol-Fe_2VAl. The direction of the synthesized vector is vertically down, showing a total exergy consumption of −808 kJ/mol-Fe_2VAl

Similarly, Figure 3–6 and 3–7 show the thermodynamic compasses of the proposed systems using single thermite synthesis and double thermite synthesis,

respectively. The vectors of (iv) the Hall–Héroult process and the corresponding electric power shown as white dots have a unit of 10 kJ per 1 mol of Fe_2VAl. The vectors of (viii) Alloying (single thermite synthesis) in Figure 3–6 and (x) Alloying of Fe_2VAl (double thermite synthesis) in Figure 3–7 are in the first quadrant and the slopes of vectors (viii) and (x) are less than 1, showing that processes (viii) and (x) are heat-receiving process. The vector of (ix) Thermite synthesis of Fe in Figure 3–7 is placed in the third quadrant and the slope of vector (ix) is less than 1, showing that process (ix) is a heat-giving process. The directions of the synthesized vectors are also vertically down, indicating total *EXL*s of 562 kJ/mol-Fe_2VAl and 1313 kJ/mol-Fe_2VAl, respectively.

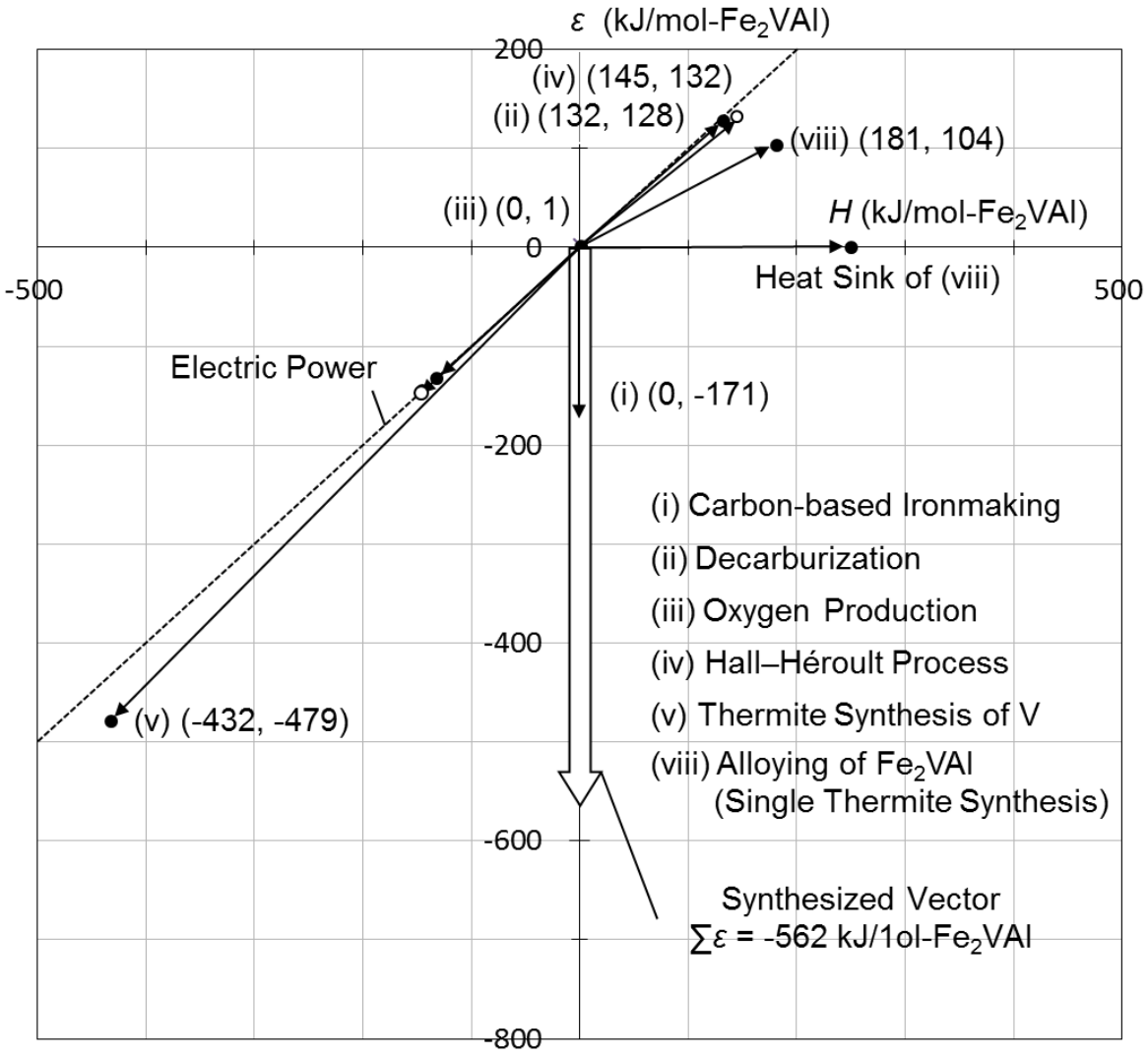


Fig. 3–6 An enthalpy–exergy diagram showing vectors of each phenomenon in the proposed method using single thermite synthesis to produce Fe_2VAl. The vectors of (iv) and the corresponding electric power, shown as white circles, have a scale of 10 kJ/mol-Fe_2VAl. The direction of the synthesized vector is vertically down, showing a total exergy consumption of −562 kJ/mol-Fe_2VAl

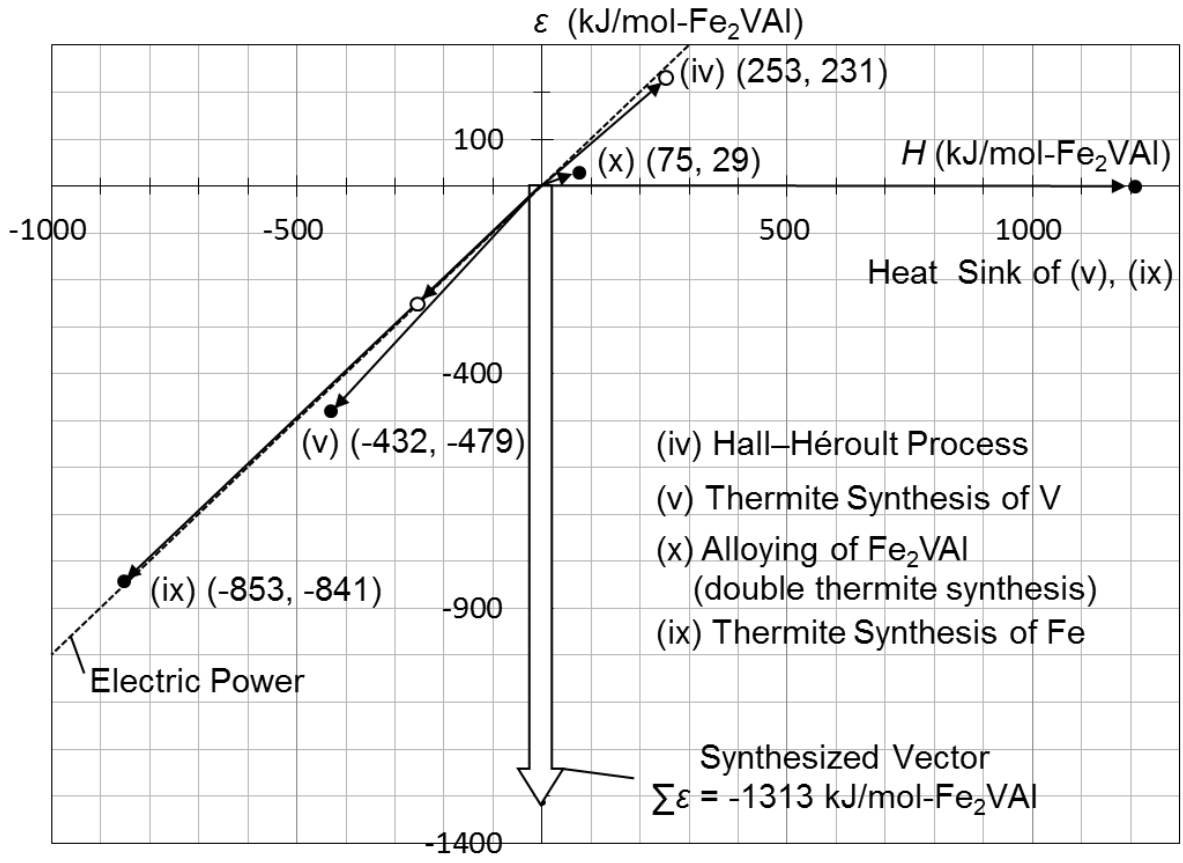


Fig. 3–7 An enthalpy–exergy diagram showing vectors of each phenomenon in the proposed method using double thermite synthesis to produce Fe_2VAl. The vectors of (iv) and the corresponding electric power, shown as white circles, have a scale of 10 kJ/mol-Fe_2VAl. The direction of the synthesized vector is vertically down, showing a total exergy consumption of −1313 kJ/mol-Fe_2VAl

Figure 3–8 shows a comparison of the conventional and proposed methods in terms of the *EXL* and required amount of C and Al during production of 1 mol of Fe_2VAl. The proposed method using single thermite synthesis showed the least *EXL*, 562 kJ/mol-Fe_2VAl, compared to the conventional arc-melting method with 808 kJ and the other proposed method of double thermite synthesis with 1313 kJ per 1 mol of Fe_2VAl. Despite the same amount of required C and Al, the proposed single thermite synthesis method thus decreased the *EXL* by 30%. The differences in the *EXL* between conventional arc-melting and proposed single thermite synthesis are the vectors (vi) Cooling of V (which is considered only for arc-melting and not for single thermite synthesis) and (vii) Alloying of Fe_2VAl (arc-melting) and (viii) Alloying of Fe_2VAl (single thermite synthesis) differ by the sensible heat of V. For single thermite synthesis, the thermite synthesis of V and alloying of Fe_2VAl occur simultaneously, which results in less *EXL* and the beneficial use of sensible heat of V that can be utilized for alloying of Fe_2VAl. For the double thermite synthesis, Fe is provided through thermite synthesis so that the sensible heat of Fe can be used for alloying of Fe_2VAl in addition to the sensible heat of V. However, thermite synthesis of Fe is a more exergy-consuming process compared to steelworks, which consist of carbon-based ironmaking, decarburization, and oxygen production. As a result, utilization of the thermite reaction of Fe for alloying Fe_2VAl resulted in the consumption of more exergy.

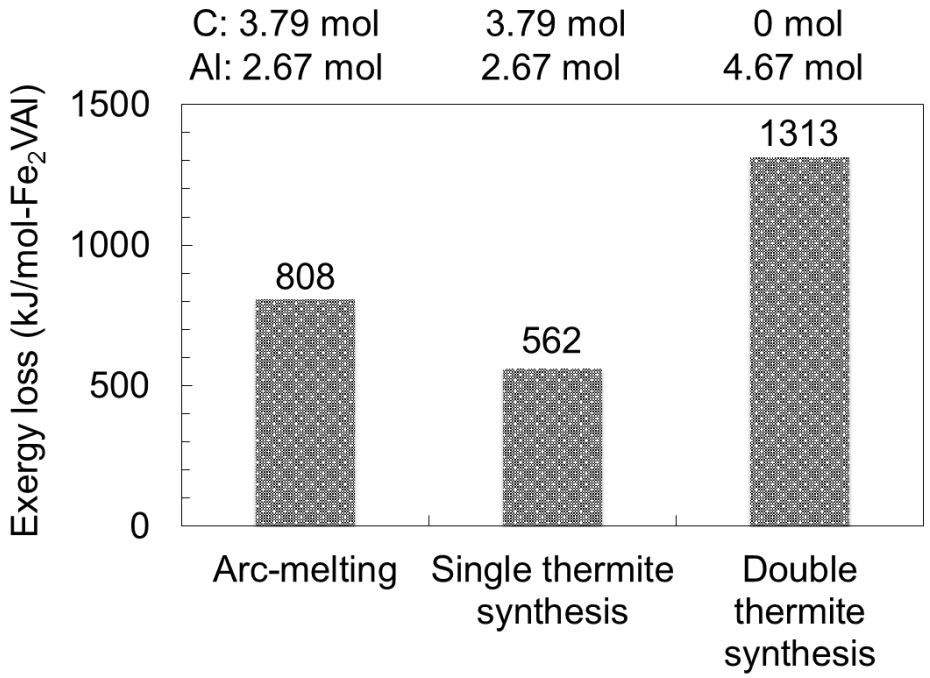


Fig. 3–8 Comparison of the conventional and proposed methods in terms of the *EXL* and required amount of C and Al during production of 1 mol of Fe_2VAl

3.5 Conclusions

In this chapter, new methods to synthesize Fe_2VAl based on utilizing the reaction heat of thermite reactions was studied by means of an enthalpy–exergy diagram and a thermodynamic comparison focusing on enthalpy and exergy. The following results were obtained:

(1) *EXL* of single thermite synthesis decreased by 751 kJ per 1 mol of synthesized Fe_2VAl compared to that of double thermite synthesis due to the reduction method of Fe. From the standpoint of exergy, the Fe should be prepared through steelworks, including carbon-based ironmaking, decarburization, and oxygen production, rather than in a thermite reaction using Al.

(2) By comparing *EXL* of systems, the production method consuming the least exergy was found to be the proposed single thermite synthesis method. The main reason why the single thermite synthesis method is the most suitable for producing Fe_2VAl is that the sensible heat of V can be utilized for the alloying of Fe_2VAl effectively.

(3) The total *EXL* of conventional arc-melting method and two proposed methods, single thermite synthesis and double thermite synthesis, were calculated to be 808 kJ, 562 kJ, and 1313 kJ per 1 mol of synthesized Fe_2VAl, respectively. The proposed single thermite synthesis decreased the *EXL* by 30% compared to that of the conventional arc-melting method.

3.6 References

[1] Masashi Mikami, Keizo Kobayashi, Tetsuya Kawada, Kazuya Kubo, Naoki Uchiyama. (2008). Development and Evaluation of High-Strength Fe_2VAl Thermoelectric Module. *Jpn J Appl Phys*, *47*, (3), 1512–1516.

[2] M. Mikami, A. Matsumoto, K. Kobayashi. (2008). Synthesis and thermoelectric properties of microstructural Heusler Fe_2VAl alloy. *J Alloys Compd*, *461*, (1–2), 423–426.

[3] Hiroyuki Nakayama, Naoki Ide, Yoichi Nishino. (2008). Thermoelectric Properties of P-Type Heusler Compounds $(Fe_{2-x}Co_x)(V_{1-y}Ti_y)Al$. *Mater. Trans.*, *49*, (8), 1858–1862.

[4] Y. Nishino, S. Deguchi, U. Mizutani. (2006). Thermal and transport properties of the Heusler-type $Fe_2VAl_{1-x}Ge_x(0\leq x\leq 0.20)$ alloys: Effect of doping on lattice thermal conductivity, electrical resistivity, and Seebeck coefficient. *Phys Rev B*, *74*, (11),

[5] Ryosuke O. Suzuki, Takashi Kyono. (2004). Thermoelectric properties of Fe_2TiAl Heusler alloys. *J Alloys Compd*, *377*, (1–2), 38–42.

[6] Dwi Nanto, Dong-Seok Yang, Seong-Cho Yu. (2013). Magnetic properties and EXAFS study of nanocrystalline $Fe_2Mn_{0.5}Cu_{0.5}Al$ synthesized using mechanical alloying technique. *Physica B: Condensed Matter*,

[7] L. L. Wang, Z. A. Munir, Y. M. Maximov. (1993). Review Thermite reactions: their utilization in the synthesis and processing of materials. *J Mater Sci 28*, 3693–3708.

[8] T. K. Mukherjee, C. K. Gupta. (1972). Open aluminothermic reduction of vanadium oxides. *J. Less-Commom Metals*, *27*, 251–254.

[9] Danieli Aparecida Pereira De Souza, Carlos Angelo Nunes, Hugo Ricardo, Zschommler Sandim, Alfeu Saraiva Ramos, Angelo Capri Neto. (2000). The effect of excess Al and fabrication environment on the composition and microstructure of V–Al alloys. *Int J Refract Metals Hard Mater*, *18*, 55–60.

[10] Hitesh Bindra, Pablo Bueno, Jeffrey F. Morris, Reuel Shinnar. (2013). Thermal analysis and exergy evaluation of packed bed thermal storage systems. *Applied Thermal Engineering*, *52*, (2), 255–263.

[11] Chao Xu, Zhifeng Wang, Xin Li, Feihu Sun. (2011). Energy and exergy analysis of solar power tower plants. *Applied Thermal Engineering*, *31*, (17–18), 3904–3913.

[12] İbrahim Dinçer, A. Rosen Marc. (2007). *Exergy, energy, environment and sustainable development*, Amsterdam: Elsevier/JAI.

[13] Takehito Hiraki, Tomohiro Akiyama. (2009). Exergetic life cycle assessment of new waste aluminium treatment system with co-production of pressurized hydrogen and aluminium hydroxide., *Int J Hydrogen Energy*, *34*, 153–161.

[14] Naoto Yasuda, Tohru Tsuchiya, Noriyuki Okinaka, Tomohiro Akiyama. (2012). Exergy

analysis of self-ignition combustion synthesis for producing rare-earth-based hydrogen storage alloy. *Int J Hydrogen Energy*, *37*, 9706–9715.

[15] Nobuhiro Maruoka, Hadi Purwanto, Tomohiro Akiyama. (2010). Exergy Analysis of Methane Steam Reformer Utilizing Steelmaking Waste Heat. *ISIJ Int*, *50*, (9), 1311–1318.

[16] Masaru Ishida, Chia-Chin Chunag. (1997). New approach to thermodynamics. *Energy Convers Mgmt*, *38*, (15-17), 1543-1555.

[17] Tomohiro Akiyama, Junichiro Yagi. (1998). Methodology to Evaluate Reduction Limit of Carbon Dioxide Emission and Minimum Exergy Consumptionfor Ironmaking. *ISIJ Int*, *38*, (8), 896–903.

[18] M Yamamoto, M Ishida. (2002). Process vectors both to create functional structures and to represent characteristics of an entire system. *Energy Conversion and Management*, *43*, 1271-1282.

[19] L. Keith Hudson, Chanakya Misra, Anthony J. Perrotta, Karl Wefers, F. S. Williams. (2003). "*Ullmann's encyclopedia of industrial chemistry: Aluminum Oxide*": 6th ed., New York: John Wiley & Sons.

Nomenclature

H: Enthalpy (J)

ε: Exergy (J)

m: Mass (g)

C_p: Specific heat at constant pressure (J/gK)

T: Temperature (K)

T_m: Melting point (K)

Q_L: Latent heat (J/g)

T_0: Environmental temperature (K)

ε^0: Standard chemical exergy (J)

G: Standard Gibbs energy of formation (J)

EXL: Exergy loss (J)

Subscripts:

s: Solid

l: Liquid

p: Product

r: Reactant

Superscripts:

0: Standard state

Chapter 4

Life cycle assessment of thermoelectric power generation system

4.1 Introduction

Thermoelectric power generation (TEG) is an energy conversion technology that employs the Seebeck effect to generate electricity directly from heat, utilizing thermoelectric elements. TEG has several merits, such as quietness, maintenance-free long-term operation owing to the absence of moving parts, and a lack of emission of greenhouse gases (*GHG*) during power generation. For example, a thermoelectric generator has been built in a Jupiter exploration satellite and a communication device for military purposes [1]. Recently, thermoelectric technology has attracted much attention because it can generate electricity by recovering waste heat discharged from industrial sectors. SWCC Showa Holdings Co., Ltd. reported a successful long-term power generation experiment using a TEG module with cobalt oxide thermoelectric elements developed by the National Institute of Advanced Industrial Science and Technology [2]. The power generation experiment operated for more than 3000 h. The generated electricity was converted to AC 100 V, and successfully charged a secondary battery. In the Japanese town of Kusatsu, the Toshiba Corporation carried out verification tests of a TEG system using heat from a thermal spring [3]. Thermoelectric modules with Bi-Te elements developed by Toshiba were used to generate electricity, which was utilized to power lighting and television in the spa center, and for emergency power.

While the practical application of TEG technology proceeds, there are several reported energy analyses of TEG systems. Y. Hori et al. [4] conducted energy analysis of a TEG system using Bi-Te thermoelectric elements, and found that the input energy for the raw materials of the thermoelectric modules was 2248 GJ, which accounted for 5.3% of the total materials energy. In that study, total energy requirement for the TEG system, including materials, processing, transportation, and construction, was 2.7 TJ. Based on the energy balance, the authors concluded that the TEG system should be approved as a power generation system. In a different study, Y. Hori et al. [5] investigated the relationship between environmental load and the design of the thermoelectric module. Life cycle CO_2 emission was established, particularly at the manufacturing stage of the module, and they concluded that a module design with 90% elemental occupancy and 3 mm height of element would minimize life cycle CO_2 emissions. P. E. Martinez et al. [6] studied a methodology to select the configuration and unit operating loads of interconnected to the Argentinean electricity network, minimizing life cycle *GHG* emissions and operating cost. They formulated mixed-integer linear programming problems solved in GAMS, and concluded that there was a general trend toward the use of hydroelectric, nuclear, and toward the most efficient and less polluting thermoelectric units operating a combined cycle, burning natural gas.

The above studies have demonstrated the environmental benefits and potential of TEG as a power generation system. To evaluate the possible benefits of TEG as a power generation technology, several studies have evaluated the reduction of CO_2 emissions and energy consumption [4–6]. However, those studies ignored the major environmental impacts associated with the mining and smelting of rare metals [7]. Furthermore, previous studies did not investigate the composition and characteristics of individual thermoelectric elements. Therefore, the assessment of environmental impacts throughout

the life cycle, from cradle to grave, is imperative for the establishment of a sustainable TEG system. The purpose of this chapter is to investigate the environmental impacts of a TEG system using three kinds of thermoelectric pairs by means of life cycle assessment (LCA). LCA is a technique to estimate the environmental impact of a product or system, which has been implemented by the International Organization for Standardization (ISO 14040 [8] and ISO 14044 [9]). As described in Chapter 1, since there are abundant sources of waste heat from steelworks, the present analysis investigated the recovery of radiant heat from continuous casting equipment used in steelworks. Energy payback time (*EPBT*) and life cycle *GHG* emissions were each estimated upon both current and future technologies. The present study follows earlier research and development that reported on an energy-saving TEG technology using waste heat from the iron-making process, which was developed by the New Energy and Industrial Technology Development Organization (NEDO) [10–12].

4.2 Life cycle of TEG system

4.2.1 Specification of a TEG system

Figure 4–1 shows a conceptual diagram of the TEG unit and TEG system, designed for recovery of exhaust radiant heat discharged from the slab in continuous casting equipment in steelworks. The TEG unit consists of modules, a heat–absorbing plate, and a heat–emitting plate. The TEG system is composed of the modules and the balance of system (BOS) components, which refers to components of the TEG system other than the module that comprises the heat-absorbing plate, heat-emitting plate, power conditioner, piping, pump, and support structure. Since the module is sandwiched between the heat-absorbing plate and the heat-emitting plate, the modules thereby take heat from the heat source. The modules are then water–cooled on one side, with the result that a temperature difference is maintained in the unit and power is generated. The operational lifetime of the system is assumed to be 10 years [13], and the present study assumes that half of the power generation units used in the system are renewed at 5 years. In this study, the slab at the horizontal portion of the continuous casting equipment was assumed to be the heat source for the TEG system. Figure 4–2 (a) shows the installation of the TEG system to the continuous casting equipment in the steelworks, (b) shows the appearance of the installed TEG system [10, 12]. In this chapter, TEG units of total area 8 m^2 were assumed to be placed on top of the slab [10, 12]. In order to allow the repair and replacement of units, each 8 m^2 section comprises 56 individual units, each approximately ISO A3 size (297 × 420 mm).

The utilization rate of the system was assumed to be the same as that of the continuous casting equipment. Statistical data on the utilization of continuous casting equipment were not collected in this study, but the integrated steel plant operates

continuously so that the molten steel that has passed through the converter from the blast furnace is poured. Therefore, the utilization of continuous casting equipment and utilization of the TEG system was assumed to be 80% [10].

The specifications of the TEG system assumed in this study are shown in Table 4–1. Three types of element pairs were investigated in cases A to C. In case A, Bi_2Te_3-type was studied; this is one of the thermoelectric materials presently available that offers excellent properties. Bi_2Te_3-type has already been put to practical use in thermoelectric cooling, and also there is no doubt that it is the most feasible as TEG [14] , despite several natural resource and environmental issues that remain to be solved. Additionally, forthcoming thermoelectric element pairs of $SrTiO_3$ and NiMo types and Fe_2VAl type were investigated in cases B and C, respectively. Detailed specifications of the thermoelectric modules for each case are described in sections 4.3.2 and 4.3.3. Previous studies have reported a power density of TEG module is small, so that the typical numerical values of power density of the TEG module with objective elements were used in this chapter. The output densities of the TEG modules were taken to be 1.0 [15], 0.47 [16], and 0.73 [17] W/cm^2 for case A, B, and C respectively. Taking into account the gaps between modules, the output density of the TEG system is lower than that of the modules. The installation rate of modules in the TEG system was determined to be 25 %. In order to investigate the feasibility of the TEG system using the next generation thermoelectric elements, such as $SrTiO_3$ and Fe_2VAl, the effects of improvement of the output density of the module if 10 % and 20 % higher were also examined for case B and C as a future technological scenario.

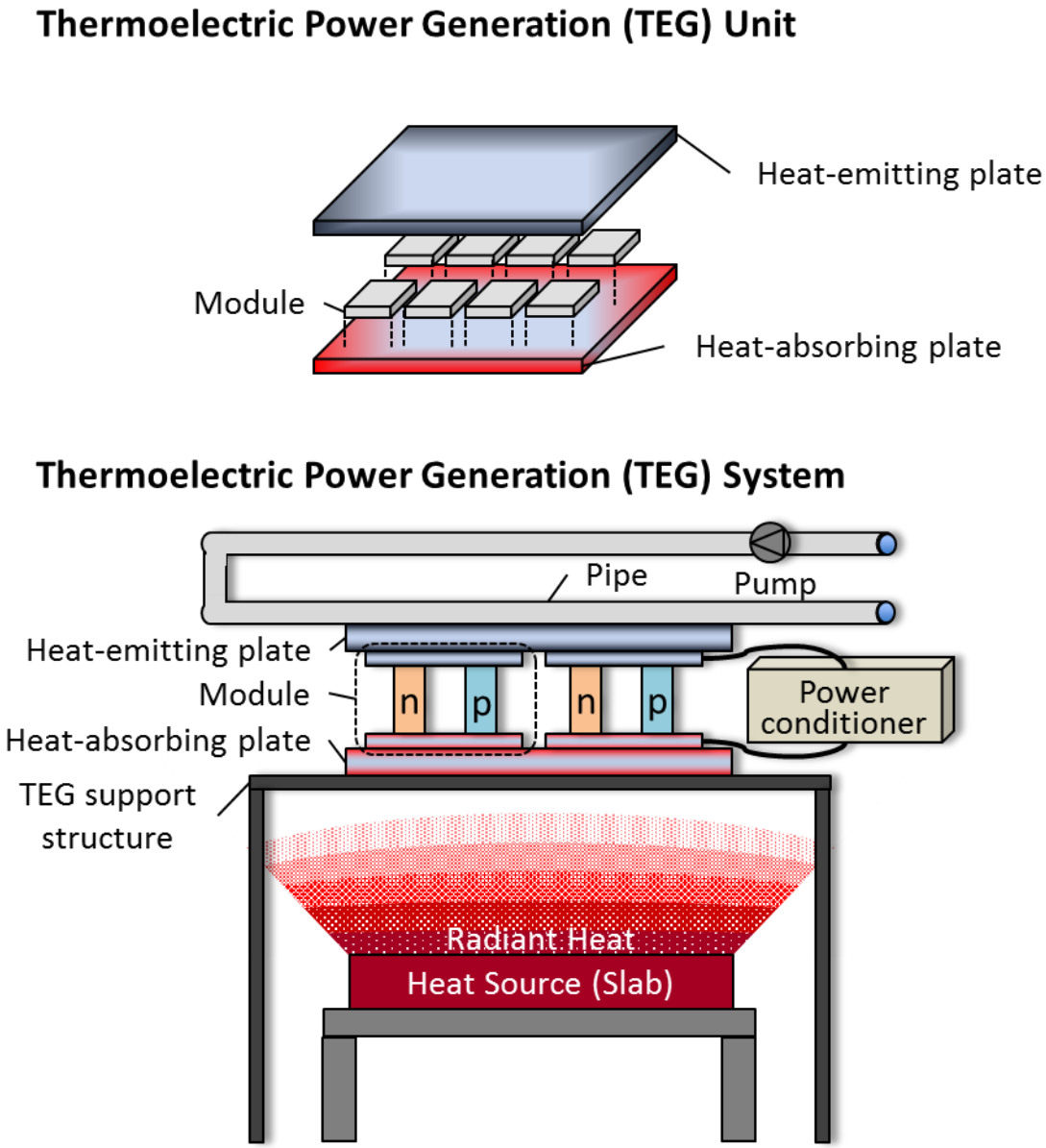


Fig. 4–1 Conceptual diagram of a thermoelectric power generation system. A thermoelectric power generation (TEG) unit consists of modules, a heat-absorbing plate, and a heat-emitting plate. The TEG system comprises the TEG unit and the balance of system (BOS)

Table 4–1 Specifications of the thermoelectric power generation system assumed in this study

		Specifications						
		Case A	Case B			Case C		
Type of element	p–type	$(Bi_{0.5}Sb_{1.5})Te_3$ [4]	$Ni_{0.9}Mo_{0.1}$ [16]			$Fe_2(V_{0.6}Ti_{0.3}W_{0.1})Al$ [18]		
	n–type	$Bi_2(Te_{2.85}Se_{0.15})$ [4]	$(La_{0.035}Sr_{0.965})TiO_3$ [16]			$Fe_2(V_{0.9}W_{0.1})Al$ [19]		
Output density of module (W/cm^2)		1.00* [15]	0.470** [16]			0.730*** [17]		
Output density of the system, E_A (kW/m^2)		Current technology	Current technology	Future technology		Current technology	Future technology	
		2.50	1.18	1.29 (10% up)	1.41 (20% up)	1.83	2.01 (10% up)	2.19 (20% up)
Installation rate of modules in system		25.0%						
System component		Unit; Module, Heat-absorbing plate, Heat-emitting plate, BOS; Power conditioner, Piping, Pump, and Support structure						
Lifetime of the system, $t_{lifetime}$ (years)		10 [13]						
Utilization rate, u**** (%)		80 [10]						

* The output density of the thermoelectric module refers to [15] (1.0 W/cm^2 was reported when the temperature of high temperature side was 553 K; the temperature difference is at 250 K).

** Output density of thermoelectric module 0.47 W/cm^2 refers to [16] (0.47 W/cm^2 was reported when the temperature of cold side was 293 K, the temperature difference was at 372 K).

*** Output density of 0.73 W/cm^2 for thermoelectric module refers to [17] (0.73 W/cm^2 was reported when the temperature of cold temperature side was 293 K, the temperature difference is at 380 K).

**** The utilization rate was assumed to be the same as that of continuous casting equipment in integrated steelworks, namely 80 % [10]

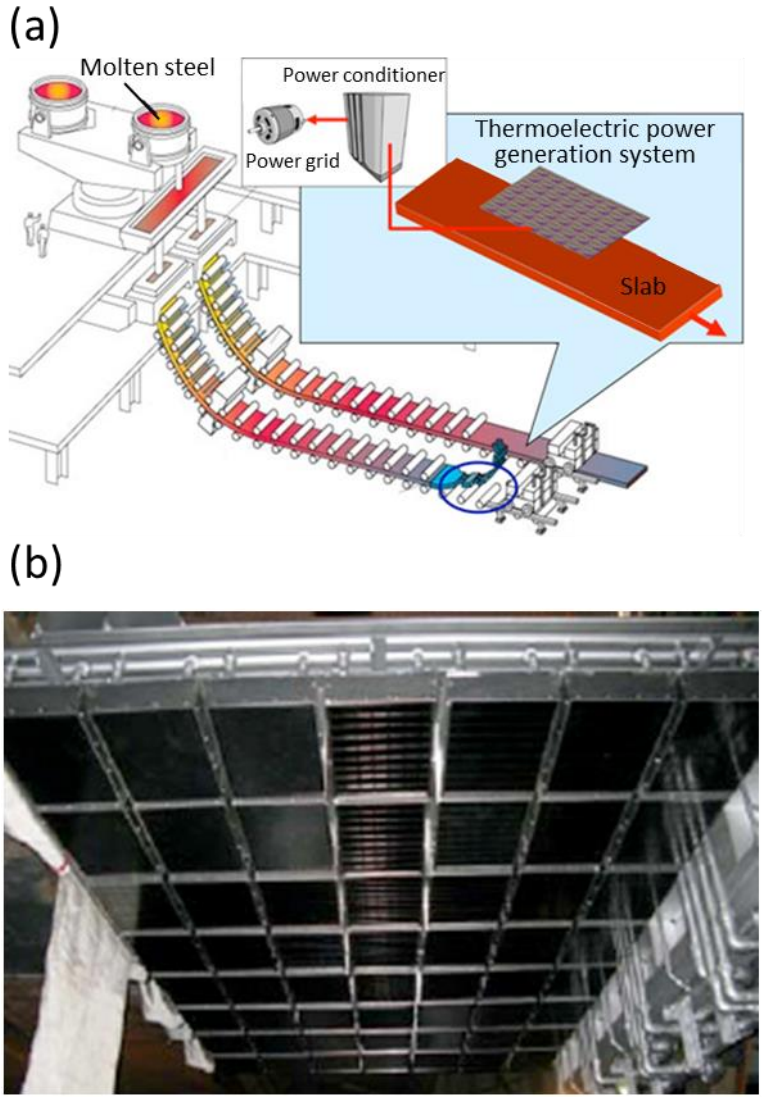


Fig. 4–2 (a) Image of thermoelectric power generation (TEG) system installed with continuous casting equipment in steelworks, and (b) appearance of installed TEG system (Source: modified from JFE Steel Corporation) [10]

4.2.2 Functional unit and evaluation indicator

The functional unit was the amount of power generation, which was determined as 1 kWh.

As the evaluation indicator of the TEG system, specific environmental impact per generated electric energy and *EPBT* were evaluated. One of the most common metrics of power generation systems is the rate of GHG emissions per unit of electricity generated [20–25]. *GHG* emission rate is defined in equation (4–1):

$$GHG_{e-rate} = \frac{GHG_{e-total}}{E_{output-total}} \tag{4–1}$$

where GHG_{e-rate} is the *GHG* emission rate per unit electricity power generated, $GHG_{e-total}$ is the total amount of *GHG* emission throughout the life cycle, $E_{output-total}$ is the total electricity generated by the TEG system during its life cycle, and GHG_{module} and GHG_{BOS} are the total *GHG* emissions with respect to the TEG modules and BOS components, respectively.

The *EPBT* indicator is defined as the number of years required for a TEG system to generate a certain amount of energy (converted into equivalent primary energy) to offset the energy embedded in TEG manufacture, assembly, installation, operation, maintenance, and system post-treatment and transportation. *EPBT* is excellent shorter. *EPBT* can be described by equation (4–2):

$$EPBT = \frac{E_{input}+E_{BOS,E}}{E_{output}} \tag{4–2}$$

where E_{input} is the primary energy requirement of the TEG module during the life cycle, including the energy requirements of manufacturing, transportation, operation, maintenance, and post–treatment. $E_{BOS,E}$ is the energy input for BOS components, which include the heat–absorbing plate, heat–emitting plate, pump, piping, support structure, and power conditioner. E_{output} is the NET annual energy savings due to electricity generation by the TEG system. In carrying calculate the *EPBT*, it is necessary to calculate the input and output of energy by aligning primary energy and secondary energy. Along the definition of *EPBT* in photovoltaic power generation, in this study, *EPBT* of TEG system is defined by rewriting equation (4–2) as following:

$$EPBT = \frac{E_{input,ele} \times f_{ele} + E_{input,fossil}}{(E_{output,ele} - E_{operate,ele}) \times f_{ele} - E_{operate,fossil}}. \quad (4–3)$$

Where $E_{input,ele}$, f_{ele}, $E_{input,fossil}$, $E_{output,ele}$, $E_{operate,ele}$, $E_{operate,fossil}$ are the initial electricity requirement of the TEG system, primary energy conversion factor of electricity, initial fossil fuels requirement of the TEG system, the annual energy savings due to electricity generation by the TEG system, the annual electricity requirement of the operation of the TEG system, and the annual fossil fuels requirement of the operation of the TEG system.

The *EPR* indicator represents the magnification of the energy that can be saved by power generation against the energy that is introduced into the life cycle. *EPR* is excellent as it is large. In this study, *EPR* of TEG system is defined as following:

$$EPR = \frac{\{(E_{output,ele} - E_{operate,ele}) \times f_{ele} - E_{operate,fossil}\} \times t_{lifetime}}{E_{input,ele} \times f_{ele} + E_{input,fossil}}. \quad (4–4)$$

Where $t_{lifetime}$ is lifetime of the TEG system.

EPBT is required to be sufficiently smaller that its lifetime, and *EPR* is required to be sufficiently larger than 1 for the power generation system. When the *EPR* is 1 or more, *EPR* can be rewritten as following:

$$EPR = \frac{t_{lifetime}}{EPBT}. \quad (4–5)$$

4.2.3 System boundary

Figure 4–3 shows the life cycle flow chart of the TEG system. Processes considered in this study include the following:

- mining of raw materials;
- manufacturing of materials and the components (module, heat-absorbing plate, heat-emitting plate, power conditioner, piping, pump, support structure) of the TEG system;
- operation of the system and maintenance of the system, including manufacturing replacement units;
- decommissioning and disposal or recycling; and
- transportation of main raw materials, intermediate products, parts, and the TEG unit.

In this study, the assembly stage was not considered, since statistical data on assembling the TEG system were unavailable. Consequently, the energy requirement for assembly was estimated to be quite small through a paper-based survey among manufacturers of thermoelectric module. At the materials processing stage, by-products associated with materials within the system boundary were assumed to cross the system boundary. For processes that discharge multiple products, allocated data were used for the analysis. In the recycling stage, recycled materials were assumed to exit the system

boundary. In addition, during the operating stage, electricity generated by using waste radiant heat from the slab of the continuous casting equipment can substitute for electricity produced by hydroelectric and thermal power. Therefore, the electricity generated by the TEG system was assumed to be able to reduce the energy input to the system power, so that the environmental impact (based on the average power demand) was reduced according to the amount of electricity generated.

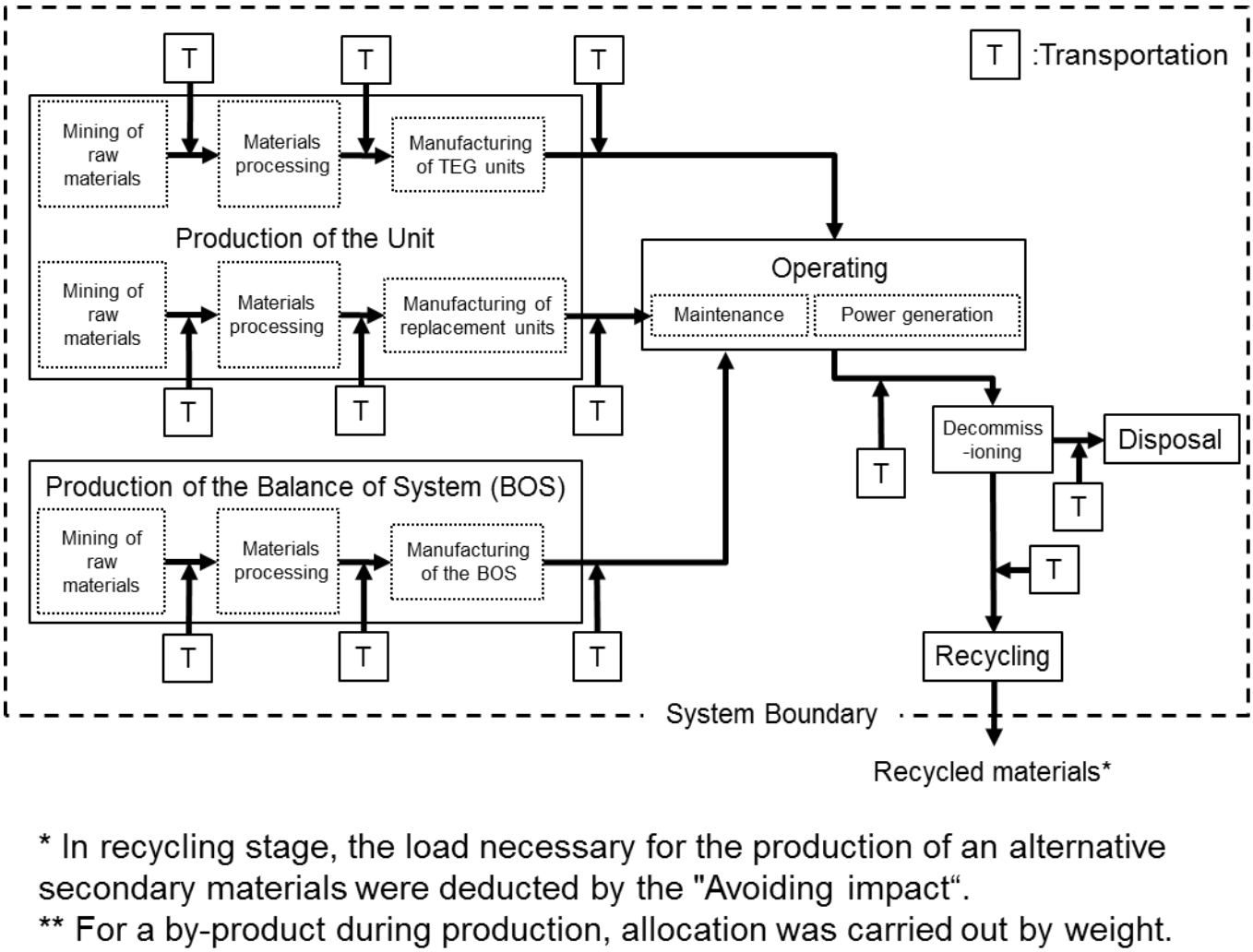


Fig. 4–3 Flow chart of life cycle stages of thermoelectric generation system

4.2.4 Collection of data for calculation

SimaPro LCA software [26] was used to calculate and evaluate the environmental impacts throughout the life cycle of the TEG system, and to calculate inventory elements and create product and systems assemblies. The SimaPro libraries and databases were mainly used to calculate inventories, supplemented by the Inventory Database for Environmental Analysis (IDEA) [27]. The processes and data that were newly created in this study rather than obtained from databases and literature are described in detail in section 4.3.1.1. A list of the data used in this study is shown in Appendix A.

4.3 Data setting for the TEG system

4.3.1 Case A: Case A: With a bismuth telluride (Bi_2Te_3)-type element

4.3.1.1 Materials input

Table 4–2 shows the materials requirements for the TEG system in case A, including process loss, together with the weight fraction of the TEG module and system. In the TEG system, the bismuth telluride–based thermoelectric module is mainstream. The elements were assumed to have the typical compositions that have been reported to give high performance for each p-type and n-type [4]. Bismuth and tellurium, which are major constituents, are produced as byproducts of lead and copper smelting, respectively. Heavy use of bismuth and tellurium is one of the major features of case A, so that the life cycle of the thermoelectric module should start with the mining of lead ores and copper ores. Figure 4–4 shows a simplified flow chart of the production of the TEG system, from mining to system manufacturing stages. Lead ores are processed through mineral processing, smelting, and then electrorefining. Purified lead and anode slimes are diverted from the electrorefining process and then go through slime processing, bismuth smelting, and bismuth refining. Other elements such as antimony, silver, and arsenic are also extracted following slime processing. As in the bismuth refining flow chart, tellurium is recovered after treating copper electrowinning slimes. Bismuth and tellurium are combined to synthesize bismuth telluride thermoelectric elements.

Table 4–2 Materials requirements for TEG system in case A including process loss

Case A	Components	Constituents	Amount used Mass (kg)	Yield rate* (%)	Input** Mass (kg)
Unit	p–type element	$(Bi_{0.5}Sb_{1.5})Te_3$ [4]	10.7	40	40.1
	n–type element	$Bi_2(Te_{2.85}Se_{0.15})$ [4]	13.0	40	48.9
	Solder	$Sn_{95.5}Ag_{3.9}Cu_{0.6}$	0.95	90	1.58
	Electrode	Copper	11.9	90	19.8
	Cable	Copper	0.83	90	1.39
	Substrate	Alumina ceramics	15.6	90	25.9
	Frame	Polyethylene	2.38	95	3.76
	Heat-absorbing plate	Copper	756	90	840
	Heat-emitting plate	Copper	756	90	840
Balance of system (BOS)	Pump for emitted heat	Complex of steel, non-ferrous metals, and plastic	106	–	111
	Piping	Steel	396	80	495
	Support structure	Steel	163	80	204
	Power conditioner	Complex of steel, non-ferrous metals, and plastic	162	–	162

* See Appendix B

** Calculation of inputs took into account maintenance, which was carried out once during the system lifetime, in which half of the thermoelectric power generation (TEG) units are renewed.

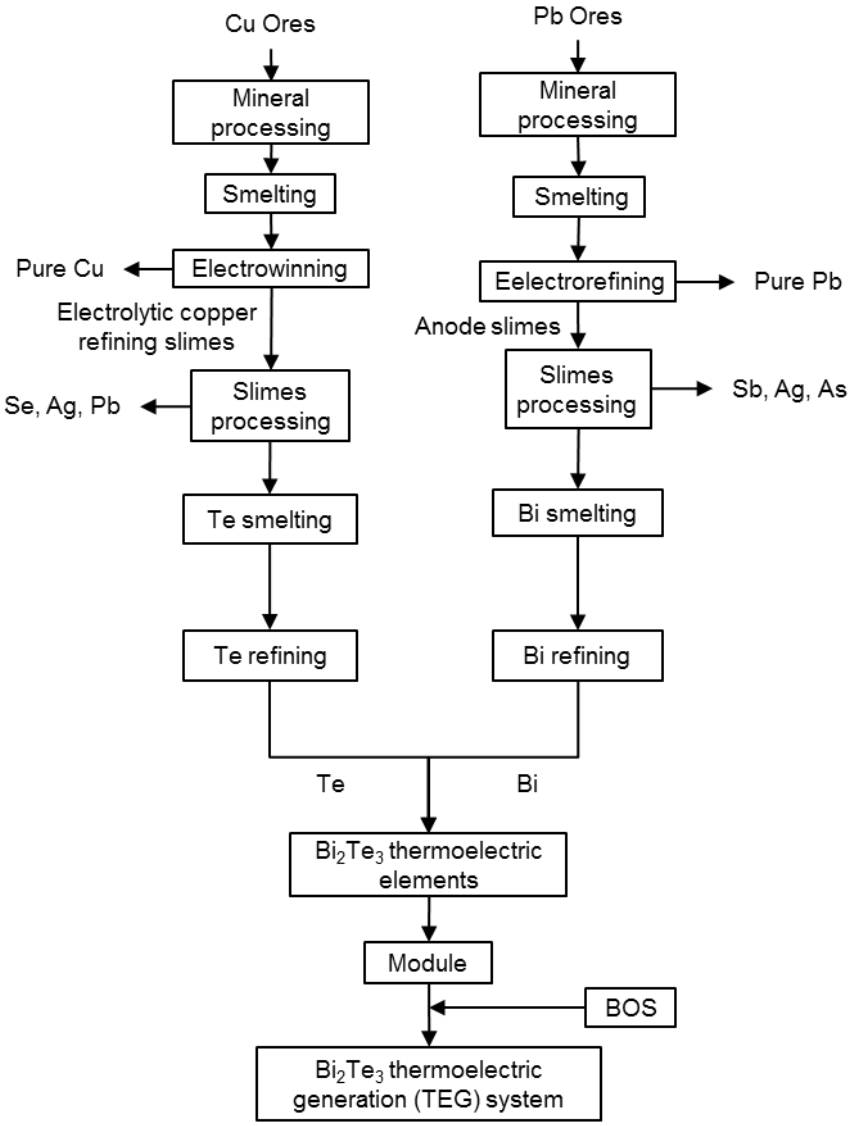


Fig. 4–4 Simplified flow chart of the production of thermoelectric generation (TEG) system, from mining to system manufacturing stages

4.3.1.2 Installation and power generation

It is generally said that thermoelectric generation systems produce no emissions of environmental impact during power generation; however, in practice, electricity will be used to operate the power conditioner and the pump on the cooling side.

Here, power generation by the TEG system and electricity consumption by the power conditioner and the pump on the cooling side were considered.

The output density of the TEG system, E_A was determined to be the product of the power density of the module and the installation rate. Therefore, the output density of the TEG system was 2.5 kW/m^2 for current technology. $E_{output,ele}$ can be calculated as follows:

$$E_{output,ele} = E_A \times A_{system} \times u \quad (4–6).$$

Where E_A, A_{system}, u are the output density of the TEG system, occupied area of the TEG system, and the utilization rate. As mentioned above, the total area of the TEG system was assumed to be 8 m^2 and utilization rate (80%) was the same as that of the continuous casting equipment [10].

The energy requirement of the power conditioner was determined from the website of SHINDENGEN Electric Manufacturing Co., Ltd. [28]. Input and output data for the cooling-side pump were from the LCI database [27]. The operation rates of the power conditioner and the pump were set to 100%. In order to cool one side of the power generation unit, it must be continuously supplied with cooling water, which was assumed to be 500 L/min. The energy and water balance of the generating stage for the TEG system in case A are shown in Table 4–3.

Table 4–3 Energy and water balance of the power generating stage for the thermoelectric generation system in case A

Case A	**Output density of the TEG system, E_A (kW/m^2)** **2.50**
Output density of module* (W/cm^2)	1.00 [15]
Installation rate of module (%)	25
Occupied area, A_{system} (m^2)	8.0
Utilization rate, u (%)	80
Annual generated electricity, $E_{output,ele}$ (MWh/year)	140
Lifetime generated electric energy, (MWh/life time)	1402
Power requirement of the power conditioner (MWh/year)	13.1
Power requirement of the pump (MWh/year)	48.2
Water requirement (L/min)	500

* The output density of the thermoelectric module was obtained from [15] (1.0 W/cm^2 was reported when the temperature of high temperature side was 553 K; the temperature difference is at 250 K).

4.3.1.3 Maintenance

In order to avoid performance degradation due to a decline in device performance, or accidents such as ground fault during power generation, the renewal of the power generation units was taken into account in the maintenance stage. It was assumed that half of the units (28 of 56 units) used in the TEG system were replaced mid–way through the 10–year lifetime. The energy requirement and effluents for the units to be replaced were taking into account in the materials processing, parts processing, and assembly stages. Therefore, the energy requirement and effluents at the maintenance stage were set to zero.

4.3.1.4 Waste recycling and management

The need to recycle the TEG system has not yet arisen, due to the difficulty in collecting generation units [13]. Therefore, no system and processing techniques for recycling TEG systems have been established in Japan. In this section, it was assumed that the TEG system was removed at the end of life, and that every component (assumed collection rate of 100%) was subject to post-processing for disposal, recycling, or recovery and re-use through existing technology. In addition, transportation after removal was considered. Transportation from the collection point to the final disposal site or recycling plant via intermediate treatment plant (crushing and screening) are considered. In all cases, the transportation distance was set at 50 km and was assumed to be via a 3.5-ton truck. The assumptions used in the regeneration and disposal rates of the TEG components are shown in Table 4–4.

Table 4–4 Assumed regeneration and disposal rates of module construction materials

	Components	Materials (mass %)	Recycle rate (%)	Disposal rate (%)
Unit	p-ype element		0	100
	n-type element		0	100
	Solder		0	100
	Electrode		96	3
	Cable		96	3
	Substrate		0	100
	Frame		52	22
	Heat-absorbing plate		96	3
	Heat-emitting plate		96	3
Balance of system (BOS)	Pump for emitted heat			
		Steel (98.3)	100	0
		Copper and brass products (1.64)	96	3
		Plastic (0.06)	52	22
	Piping		100	0
	Support structure		100	0
	Power conditioner			
		Steel (64.6)	100	0
		Copper and brass products (2.01)	96	3
		Aluminum rolled products (1.39)	96	3
		Plastic (32.0)	52	22

Table 4–5 shows the regeneration and waste amounts generated during post-processing of the TEG system. Since half of the units are to be renewed during the lifetime at the maintenance stage, note that an amount 1.5 times the initial input was assumed to be collected and processed. Process inventories were obtained from the SimaPro libraries and databases [26]. Detail definitions of recycling and disposal are described in Appendix C.

Table 4–5 Recycling and disposal quantities for the thermoelectric power generation (TEG) system in case A

Case A	Components	Materials (Ratio (%))	Initial weight (kg/system)	Collected (kg)	Crushed (kg)	Recycled (kg)	Disposed (kg)
Unit	p-type element		10.7	16.0	16.0	0	16.0
	n-type element		13.0	19.6	19.6	0	19.6
	Solder		0.95	1.43	1.43	0	1.43
	Electrode		11.9	17.8	17.8	17.1	0.534
	Cable		0.83	1.25	1.25	1.20	0.0374
	Substrate		15.6	23.3	23.3	0	23.3
	Frame		2.38	3.57	3.57	1.86	0.785
	Heat-absorbing plate		756	756	0	726	30
	Heat-emitting plate		756	756	0	726	30
Balance of system (BOS)	Pump for emitted heat		106	106			
		Steel (98.3)			104	104	0
		Copper and brass products (1.64)			1.79	1.72	0.0537
		Plastic (0.06)			0.0600	0.0312	0.0132
	Piping		396	396	0	396	0
	Support structure		163	163	0	163	0
	Power conditioner		162	162			
		Steel (64.6)			105	105	0
		Copper and brass products (2.01)			3.20	3.0816	0.0963
		Aluminum rolled products (1.39)			2.20	2.11	0.0660
		Plastic (32.0)			52.0	27.0	11.4

* The amount collected took into account maintenance, which was carried out once during the lifetime of the plant, in which half of the TEG units were renewed.

4.3.1.5 Transportation

In this section, the transportation requirements for major constituents of each component, associated raw materials, and system components were taken into account. Table 4–6 shows the transported raw material, weight, distance, and means of transportation for system components in case A. Detailed information is described in Appendix D.

Table 4–6 Transported raw material, weight, distance, and means of transportation in case A

Case A	Components	Major constituent (mass %)	Input mass (kg)	Transported major raw material	Distance	
					In producing country (km)	In Japan (km)
Unit	p-type element	Tellurium (57%)	17.4	Imported copper ore	222 (land) 12586 (marine)	100
	n-type element	Bismuth (53%)	19.7	Imported lead ore	705 (land) 7752 (marine)	100
	Solder	Tin (96%)	1.15	Imported tin ingot	5511 (Marine)	100
	Electrode	Copper (100%)	15.0	Imported copper ore	222 (land) 12586 (marine)	100
	Cable	Copper (100%)	1.05	Imported copper ore	222 (land) 12586 (marine)	100
	Substrate	Alumina (100%)	19.7	Imported aluminum hydroxide	8000 (marine)	100
	Frame	Polyethylene (100%)	2.86	–	–	100
	Heat-absorbing plate	Copper (100%)	840	Imported copper ore	222 (land) 12586 (marine)	100
	Heat-emitting plate	Copper (100%)	840	Imported copper ore	222 (land) 12586 (marine)	100
Balance of system (BOS)	Pump for emitted heat	Steel (91%)	101	Imported iron ore	8000 (marine)	100
	Piping	Steel (100%)	495	Imported iron ore	8000 (marine)	100
	Support structure	Steel (100%)	204	Imported iron ore	8000 (marine)	100
	Power conditioner	Steel (58%)	93.8	Imported iron ore	8000 (marine)	100

4.3.2 Case B: With $SrTiO_3$-type thermoelectric element

4.3.2.1 Materials input

This section investigates the life cycle inventory of a TEG system with $SrTiO_3$ thermoelectric elements. For comparison with cases A and C, it is necessary to determine the inputs to the TEG elements. From the amounts of input materials for p-type and n-type elements in case A, and the densities of Bi_2Te_3 (7.74 g/cm^3 [29]), Sb_2Te_3 (6.50 g/cm^3 [30]), and Bi_2Se_3 (7.50 g/cm^3 [31]), the volumes required for p-type and n-type elements were calculated as 4471 cm^3 and 4810 cm^3, respectively, by using a weighted average the values. The material requirements for p-type ($Ni_{0.9}Mo_{0.1}$) and n-type ($La_{0.035}Sr_{0.965}TiO_3$) were established using the required volumes shown above, and the densities of Ni (8.90 g/cm^3 [29]), Mo (10.2 g/cm^3 [29]), and $SrTiO_3$ (5.10 g/cm^3 [30]). Table 4–7 shows the materials requirements of $SrTiO_3$-type thermoelectric element in case B, including process losses. The input materials for components other than the thermoelectric elements of TEG system are shown in Table 4–2. Ni and Sr are major constituents of both the p-type and n-type elements. According to the mineral resource material flow of Ni [32], Ni metal is supplied via domestic production and imports, accounting for 42000 t and 41000 t respectively (on the basis of pure metal). Raw materials for Ni metal produced in Japan are mainly imported matte [33, 34], which is refined in ore-producing countries. On the other hand, Sr is distributed in the form of strontium nitrate or strontium carbonate in Japan, and both are imported rather than domestic production. Strontium carbonate is the most important industrial compound of strontium, and is produced from strontium sulfide (SrS), which can be obtained by reduction of celestite ore with carbon [35]. Therefore, the life cycle of the TEG system in case B should start with mining of nickel ores and strontium ores. Figure 4–5 shows a simplified flow chart of the production of a TEG system in case B, from mining to system

manufacturing stages.

Table 4–7 Materials requirements of $SrTiO_3$-type thermoelectric element in case B including process loss

Case B	Components	Constituents	Amount used Mass (kg)	Yield rate* (%)	Input** Mass (kg)
Module	p-type element	$Ni_{0.9}Mo_{0.1}$	14.7	40	55.1
	n-type element	$La_{0.035}Sr_{0.965}TiO_3$	8.30	40	31.1

* See Appendix B

** Inputs were calculated taking into account maintenance, which was carried out once during the lifetime of the plant, in which half of the thermoelectric power generation (TEG) units were renewed.

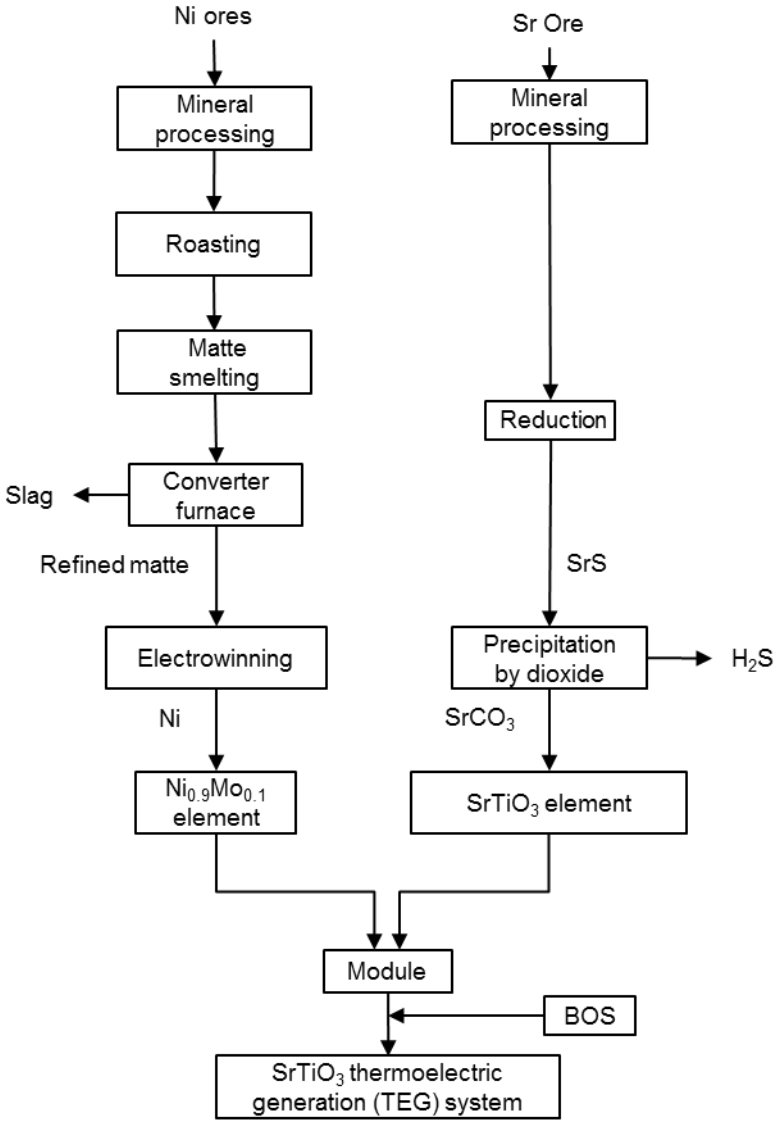


Fig. 4–5 Simplified flow chart of the production of thermoelectric generation (TEG) system in case B, from mining to system manufacturing stages

4.3.2.2 Installation and power generation

The energy and water balance of the TEG system at the generating stage are shown in Table 4–8. The specification for power generation was assumed to be the same as case A shown in Table 4–3, other than the output density of the TEG unit. The output density of the thermoelectric module was assumed to be 0.14 W/cm^2 (when the temperature of the cold side was 293 K, the temperature difference was 203 K) [16]. Similarly to case A, the gaps between modules were considered and the output density of the TEG system was assumed to be 1.18 kW/m^2 for current technology. To investigate the feasibility of the TEG system using $SrTiO_3$-type thermoelectric elements, the effects of improvement of the output density of the module if 10% and 20% higher were also examined as future technological scenarios. $E_{output,ele}$ can be calculated via equation (4–6) to be 6.59×10^4, 7.25×10^4, and 7.91×10^4 kWh/year respectively.

Table 4–8 Energy and water balance of the thermoelectric generation system at power generating stage

Case B	Output density of the TEG system, E_A (kW/m^2)		
	1.18	**1.29**	**1.41**
Output density of module* (W/cm^2)	0.47 [16]		
Installation rate of module (%)	25		
Occupied area, A_{system} (m^2)	8.0		
Utilization rate, u (%)	80		
Annual generated electric energy, $E_{output,ele}$ (kWh/year)	6.59×10^4	7.25×10^4	7.91×10^4
Lifetime generated electric energy, (kWh/life time)	6.59×10^5	7.25×10^5	7.91×10^5
Power requirement of the power conditioner (MWh/year)	13.1		
Power requirement of the pump (MWh/year)	48.2		
Water requirement (L/min)	500		

* Output density of thermoelectric module was 0.47 W/cm^2 [16] (0.47 W/cm^2 was reported when the temperature of the cold side was 293 K; the temperature difference was at 372 K)

4.3.2.3 Maintenance

In the same way as case A, it was assumed 28 units were replaced at the maintenance stage. Materials, energy requirement, and effluents for the units to be replaced were taken into account at the materials processing, parts processing, and assembly stages.

4.3.2.4 Waste recycling and management

As in case A, post-treatment was assumed. The assumed regeneration and disposal rates and the amount processed at the post-processing stage of the TEG system in case B are shown in Table 4–9. The assumed regeneration and disposal rates for components other than the thermoelectric elements of the TEG system are shown in Table 4–5.

Table 4–9 Assumed regeneration and disposal rates of thermoelectric elements at the post–processing stage in case B

Case B	Components	Initial weight (kg/system)	Collected (kg)	Crushed (kg)	Recycled (kg)	Disposed (kg)
Module	p-type element	14.7	22.1	22.1	0	22.1
	n-type element	8.30	12.5	12.5	0	12.5

*The amount collected was calculated taking into account maintenance, which was carried out once during the system lifetime, in which half of the thermoelectric power generation (TEG) units were renewed.

4.3.2.5 Transportation

Table 4–10 shows the transported raw material, weight, distance, and means of transportation for thermoelectric elements in case B. Transportation parameters in relation to system components other than the thermoelectric elements were the same as those for case A, shown in Table 4–6. Detail information is described in Appendix E.

Table 4–10 Transported raw material, weight, distance, and means of transportation in case B

Case B	Components	Major constituent (mass%)	Input mass (kg)	Transported major raw material	Distance	
					In producing country (km)	In Japan (km)
Module	p-type element	Nickel (84.6%)	46.66 (metal)	Imported nickel matte	4326 (marine)	100
	n-type element	Strontium (72.7%)	23.95 (carbonate)	Imported strontium carbonate	422 (land) 13700 (marine)	100

4.3.3 Case C: With Fe_2VAl-type thermoelectric element

4.3.3.1 Materials input

Similarly to case B, the material requirements of the Fe_2VAl-type thermoelectric element in case C were calculated from the required volume used in section 4.3.2 and the density of Fe_2VAl (6.60 g/cm^3 [36]). Table 4–11 shows the material requirements for Fe_2VAl-type thermoelectric elements in case C including process loss, together with the weight fraction of the TEG module and system. As in case B described in section 4.3.2, the input materials for components of the TEG system other than thermoelectric elements are shown in Table 4–2. Fe is the main constituent of both p-type and n-type elements. In this section, Fe for thermoelectric elements of case C was assumed to be domestically produced converter steel, so that the life cycle of the TEG system in case C was assumed to start with the mining of iron ores. Figure 4–6 shows a simplified process flow chart for iron production, together with production of the TEG system in case C, from mining to system manufacturing stages.

Table 4–11 Materials requirements of Fe_2VAl-type thermoelectric element in case C including process loss, together with the weight fraction of the TEG module and system

Case C	Components	Constituents	Amount used Mass (kg)	Yield rate* (%)	Input** Mass (kg)
Module	p-type element	$Fe_2(V_{0.6}Ti_{0.3}W_{0.1})Al$ [18]	10.8	40	40.3
	n-type element	$Fe_2(V_{0.9}W_{0.1})Al$ [19]	10.8	40	40.3

* See Appendix B

** Input was calculated taking into account maintenance, which was carried out once during the system lifetime, in which half of the thermoelectric power generation (TEG) units were renewed.

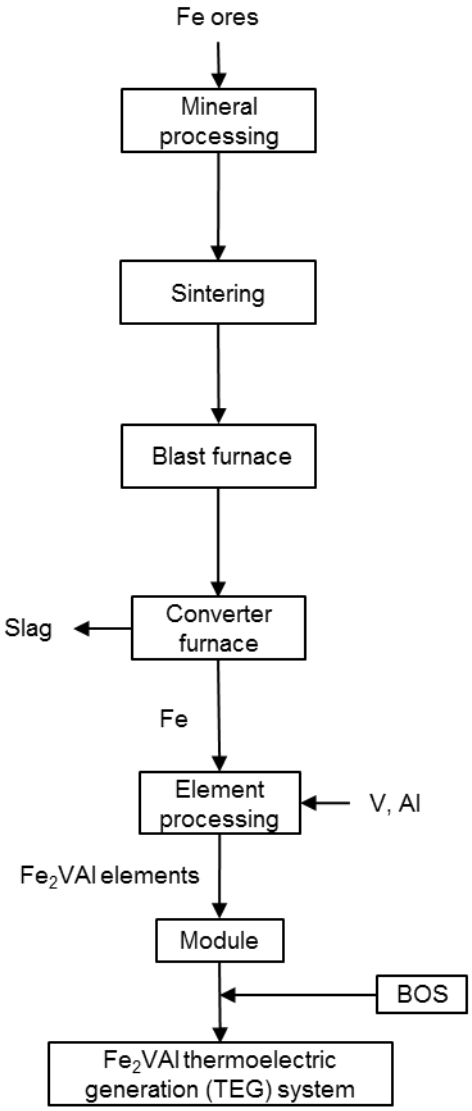


Fig. 4–6 Simplified flow chart of the production of thermoelectric generation (TEG) system in case C, from mining to system manufacturing stages

4.3.3.2 Installation and power generation

The energy and water balance of the thermoelectric generation system at the generating stage is shown in Table 4–12. The specification on power generating was assumed to be same as cases A and B shown in Table 4–3, other than the output density of the TEG unit. The output density of the thermoelectric module was assumed to be 0.51 W/cm^2 [17] (when the temperature of the cold side was 293 K, the temperature difference was 280 K) [16]. Similarly to case A, the gaps between modules were considered and then the output density of the TEG system was assumed to be 1.83 kW/m^2 for current technological scenario. As in case B, output densities 10 % and 20 % higher than that of current technology were also investigated for future technological scenarios.

Table 4–12 Energy and water balance of the thermoelectric generation system at power generating stage

Case C	Output density of the TEG system, E_A (kW/m^2)		
	1.83	**2.01**	**2.19**
Output density of module* (W/cm^2)		0.73 [17]	
Installation rate of module (%)		25	
Occupied area, A_{system} (m^2)		8.0	
Utilization rate, u (%)		80	
Annual generated electric energy, $E_{output,ele}$ (kWh/year)	1.02×10^5	1.12×10^5	1.23×10^5
Lifetime generated electric energy, (kWh/life time)	1.02×10^6	1.12×10^6	1.23×10^6
Power requirement of the power conditioner (MWh/year)		13.1	
Power requirement of the pump (MWh/year)		48.2	
Water requirement (L/min)		500	

* The output density of 0.73 W/cm^2 for the thermoelectric module was obtained from [17] (0.73 W/cm^2 was reported when the temperature of the cold temperature side was 293 K; the temperature difference is at 380 K)

4.3.3.3 Maintenance

As in cases A and B, it was assumed that 28 units were replaced at the maintenance stage. The materials, energy requirement, and effluents for the units to be replaced were taken into account at the materials processing, parts processing, and assembly stages.

4.3.3.4 Waste recycling and management

As in cases A and B, post-treatment was assumed. The assumed regeneration and disposal rates and the amount processed at the post-processing stage of the TEG system in case C are shown in Table 4–13. The regeneration and disposal rates assumed for components other than the thermoelectric elements of the TEG system are shown in Table 4–5.

Table 4–13 Assumed regeneration and disposal rates of thermoelectric elements at the post–processing stage in case C

Case C	Components	Initial weight (kg/system)	Collected* (kg)	Crushed (kg)	Recycled (kg)	Disposed (kg)
Module	p-type element	10.75	16.13	16.13	0	16.13
	n-type element	10.75	16.13	16.13	0	16.13

* The amount collected took into account maintenance, which was carried out once during the lifetime of the system, in which half of the thermoelectric power generation (TEG) units were renewed.

4.3.3.5 Transportation

Table 4–14 shows the transported raw materials, weight, distance, and means of transportation for system components in case C. Transportation parameters for system components other than the thermoelectric elements were shown in Table 4–6.

Table 4–14 Transported raw materials, weight, distance, and means of transportation in case C

Case C	Components	Major constituent (mass %)	Input mass (metal-kg)	Transported major raw material	Distance	
					In producing country (km)	In Japan (km)
Module	p-type element	Iron (55.3%)	22.3	Imported iron ore	8000 (marine)	100
	n-type element	Iron (55.0%)	22.2	Imported iron ore	8000 (marine)	100

4.4 Results and discussion

The emissions of CO_2 gas and primary energy consumption during the life cycle of the TEG system were estimated. The results of inventory analysis for CO_2 emissions, primary energy consumption at each life cycle stage in cases A to C are listed in Table 4–15, 4–16, respectively. In Tables 4–15 and 4–16, reduction of the CO_2 emissions and primary energy consumptions due to the recycling and power generation are also listed. Life cycle CO_2 emissions and primary energy consumption in the operating stage were the highest in the case of all. In this study, cooling water was assumed to be used industrial water. Use of chemicals and some emissions for the treatment of water used in power plants are included in the process data of industrial water used. If a source of cooling water is assumed from nature such as rivers and oceans, CO_2 emissions and primary energy consumptions at operation stage will be greatly reduced. Also, compared to the CO_2 emissions at the production stages of the elements and the system components other than the elements in case A, CO_2 emissions of the elements production was larger. On the other hand, CO_2 emissions at the production stage of the system components other than the elements were larger in the case B and C, showing that CO_2 emissions during the purification of the constituent metals such as Bi and Te, and Se was larger than those of the case B and C. The tendency that the load due to the elements of the constituent metals in case A was larger compared with the case B and C was also similar in Table 4–16.

Table 4–15 Life cycle emissions of CO_2 at each life cycle stage in cases A to C

CO_2 (kg)	Production of elements	Production of the system other than elements	Operating	Post-treatment and disposal	Transportation	Total	Power generation	Recycling
Case A	6345 (17%)	4575 (12%)	21308 (58%)	4245 (12%)	335 (1%)	36808 (100%)	-722239	-3635
Case B	1880 (6%)	4575 (14%)	21308 (66%)	4222 (13%)	190 (1%)	32175 (100%)	-339452	-3635
Case C	1578 (5%)	4575 (14%)	21308 (67%)	4166 (13%)	154 (1%)	31781 (100%)	-527235	-3635

Table 4–16 Life cycle primary energy consumption; (a) crude oil, (b) natural gas, (c) lignite, and (d) hard coal at each life cycle stage in cases A to C

(a) Crude oil

Crude oil (kg)	Production of elements	Production of the system other than elements	Operating	Post-treatment and disposal	Transportation	Total	Power generation	Recycling
Case A	656 (21%)	161 (5%)	1756 (57%)	434 (14%)	89 (3%)	3096 (100%)	-34563	-136
Case B	252 (10%)	161 (6%)	1756 (68%)	355 (14%)	49 (2%)	2574 (100%)	-16244	-136
Case C	503 (18%)	161 (6%)	1756 (63%)	349 (12%)	39 (1%)	2808 (100%)	-25231	-136

(b) Natural gas

Natural gas (m^3)	Production of elements	Production of the system other than elements	Operating	Post-treatment and disposal	Transportation	Total	Power generation	Recycling
Case A	655 (28%)	253 (11%)	1126 (49%)	260 (11%)	12 (1%)	2306 (100%)	-124748	-213
Case B	168 (9%)	253 (13%)	1126 (60%)	336 (18%)	7 (0%)	1889 (100%)	-58631	-213
Case C	320 (16%)	253 (12%)	1126 (55%)	332 (16%)	5 (0%)	2036 (100%)	-91066	-213

(c) Lignite

Lignite (kg)	Production of elements	Production of the system other than elements	Operating	Post-treatment and disposal	Transportation	Total	Power generation	Recycling
Case A	382 (20%)	265 (14%)	810 (42%)	464 (24%)	14 (1%)	1936 (100%)	-5075	-404
Case B	155 (9%)	265 (16%)	810 (48%)	460 (27%)	8 (0%)	1699 (100%)	-2385	-404
Case C	314 (17%)	265 (14%)	810 (44%)	453 (24%)	6 (0%)	1849 (100%)	-3705	-404

(d) Hard coal

Hard coal (kg)	Production of elements	Production of the system other than elements	Operating	Post-treatment and disposal	Transportation	Total	Power generation	Recycling
Case A	1306 (24%)	393 (7%)	2626 (48%)	1083 (20%)	13 (0%)	5422 (100%)	-199388	-1434
Case B	200 (5%)	393 (9%)	2626 (61%)	1079 (25%)	7 (0%)	4305 (100%)	-93713	-1434
Case C	621 (13%)	393 (8%)	2626 (56%)	1069 (23%)	6 (0%)	4715 (100%)	-145553	-1434

Based on the results of inventory analysis shown as a representative in Tables 4–15 and 4–16, impact analysis was performed using the characteristic model LIME1. Table 4–17 lists the results of impact analysis on (a) global warming impact and (b) resource consumption (calorific value) per unit generated electricity at each life cycle stage in cases A to C. Reduction of the global warming potential and resource consumptions due to the recycling and power generation, and total score including the loads and reduction of the load are also listed. Total lifetime electricity generation in cases A, B, and C were calculated as 1.40×10^5, 6.59×10^4, and 1.02×10^5 kWh, respectively, as shown in Tables

4–3, 4–8, and 4–12. As expected, the environmental impacts of the production of the thermoelectric elements were highest in the case of BiTe-type elements in case A. Global warming impact in case A was about three times as large as that of case C which was smallest in production of the elements in cases A to C.

Table 4–17 Life cycle (a) global warming impact and (b) resource consumption (calorific value) per unit generated electricity at each life cycle stage in cases A to C

(a) Global warming impact

($kg\ CO_2\ eq./kWh_p$)	Production of elements	Production of the system other than elements	Operating	Post-treatment and disposal	Transportation	Power generation	Recycling	Total
Case A	0.00469	0.00124	0.0146	0.00155	0.000155	-0.532	-0.00274	-0.513
Case B	0.00295	0.00264	0.0310	0.00326	0.000101	-0.532	-0.00583	-0.498
Case C	0.00164	0.00170	0.0199	0.00204	0.000029	-0.532	-0.00375	-0.511

(b) Resource consumption (calorific value)

($MJ/\ kWh_p$)	Production of elements	Production of the system other than elements	Operating	Post-treatment and disposal	Transportation	Power generation	Recycling	Total
Case A	0.0525	0.000621	0.119	0.0236	0.00202	-5.04	-0.0424	-4.88
Case B	0.0307	0.00132	0.254	0.0497	0.00132	-5.04	-0.0902	-4.79
Case C	0.0212	0.000851	0.163	0.0313	0.000345	-5.04	-0.0581	-4.88

Figure 4–7 compares *GHG* emission rates of the TEG system in cases A to C, together with the predicted reductions in *GHG* emission rate when future technology is realized. It can be seen that the *GHG* emission rate is large in the BiTe-type scenario of case A, Fe_2VAl-type in case C, and $SrTiO_3$-type in case C is the state-of-the-art. This was mainly due to large power density of BiTe-based modules. In the Fe_2VAl scenario of case C, if the power density of the module s increased by 10%, the *GHG* emission rate will be comparable to that of BiTe, and will be less than that of BiTe in the case that the output density of the module increased by 20% in future. On the other hand, for the $SrTiO_3$-based element in case B, higher output density of the module was not expected to result in lower *GHG* emission rate.

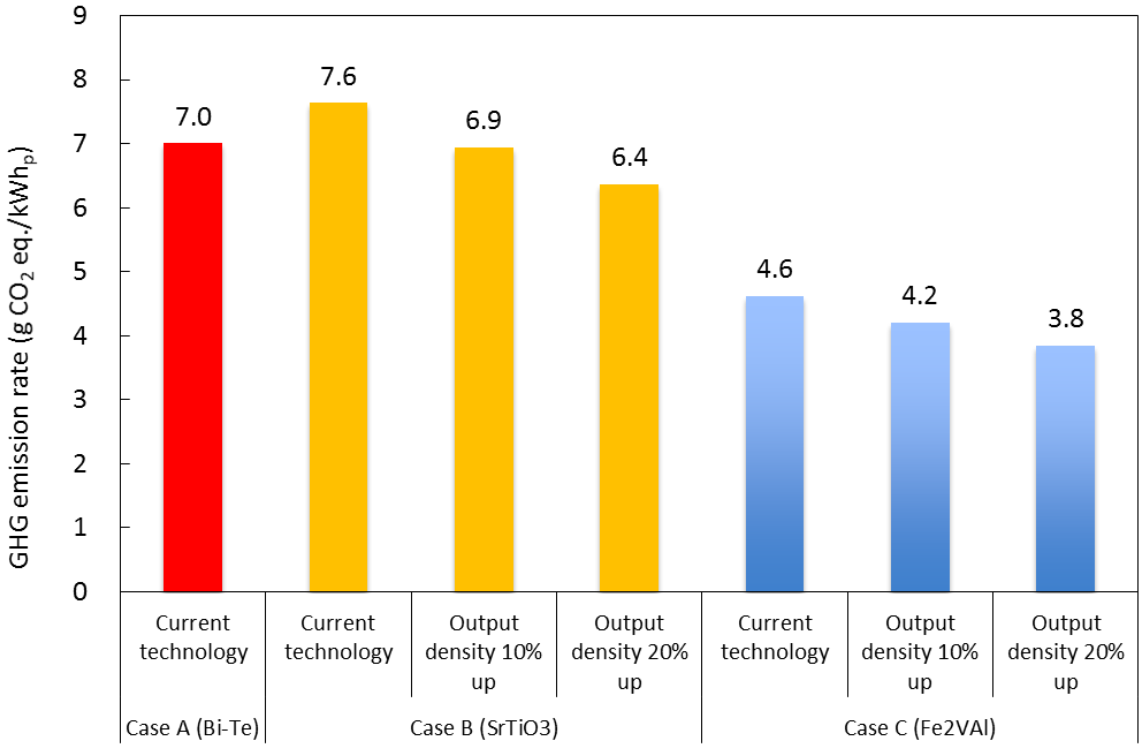


Fig. 4–7 Comparison of *GHG* emission rates of the TEG system in cases A to C, together with predicted reduction in *GHG* emission rate when future technology is realized

Figure 4–8 compares of energy profit ratio, *EPR* of the TEG system in cases A to C, together with the predicted increases in *EPR* when future technology is realized. *EPR*s in cases A to C of the state-of-the-art were 51.7, 30.2, and 49.8, respectively. The highest *EPR* was recorded in BiTe-type scenario, showing that Bi-Te type modules were the best and brightest as power generation system due to its high output density. In the Fe_2VAl scenario of case C, if the power density of the module was increased by 10%, *EPR* will be higher than that of BiTe in future. For the $SrTiO_3$-based element in case B, even if the power density of the module is increased by 20%, *EPR* is expected to be 36.4 which is much lower than that of case A and C.

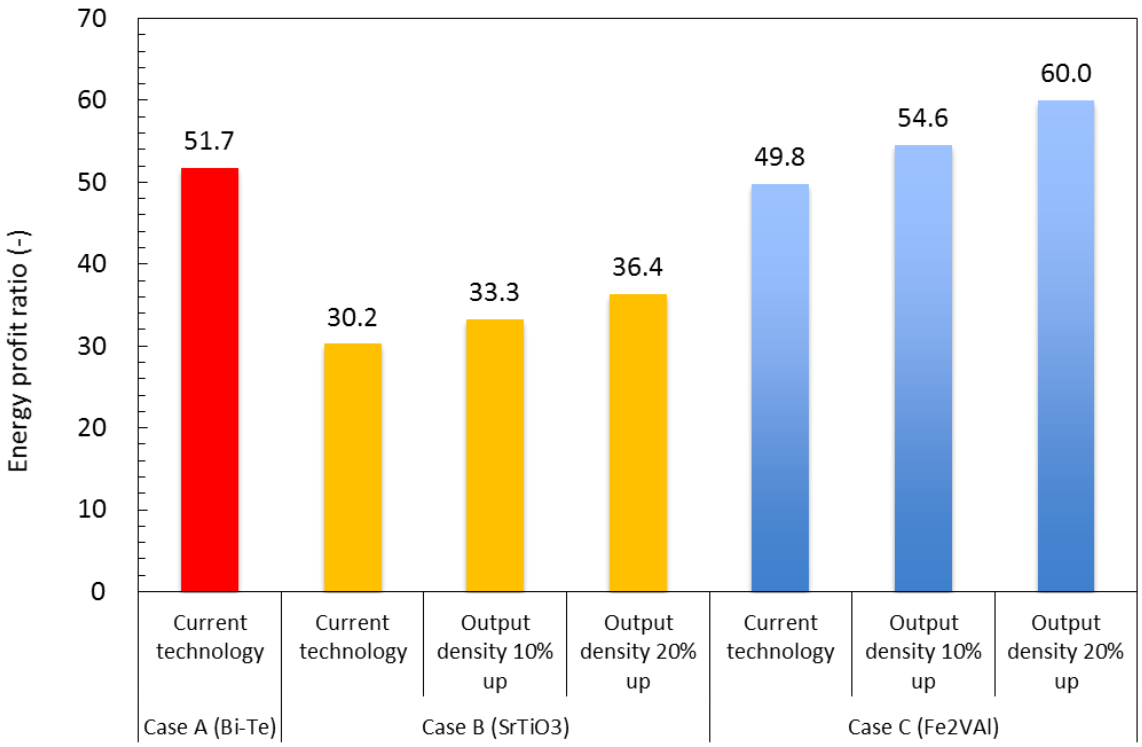


Fig. 4–8 Comparison of enrgy profit ratio (*EPR*) of the TEG system in cases A to C, together with predicted increase in *EPR* when future technology is realized

Comparison of the energy payback time, *EPBT* of the TEG system in cases A to C is shown in Figure 4–9. *EPBT*s of the TEG system for current technology were 0.19, 0.33, and 0.20 year for case A, B, and C, respectively. *EPBT*s of the current technologies in cases A to C are sufficiently small, which reveals that the TEG system with considered thermoelectric elements are good power generation system. When the increase of the output density can be achieved 20%, each *EPBT* for case B and C will be reduced to 0.28 and 0.17 year.

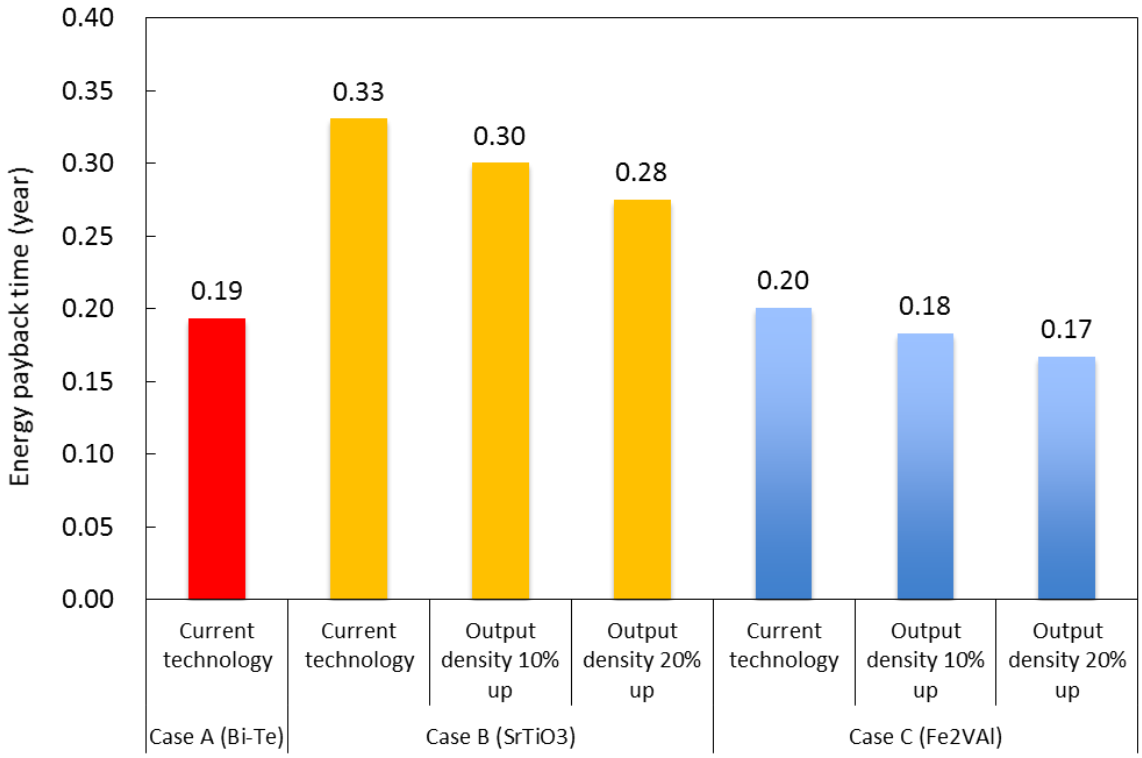


Fig. 4–9 Comparison of energy payback time (*EPBT*) of the TEG system in cases A to C, together with predicted reduction in *EPBT* when future technology is realized

4.5 Conclusions

In chapter 4, the life cycle characteristics of a TEG system with three pairs of thermoelectric elements were investigated under assumption of recovering waste heat from steelworks. The following results were obtained:

(1) *GHG* emission rates of the TEG system for the state of the art were calculated to be 7.0, 7.6, 4.6 g CO_2 eq./kWh_p for Bi_2Te_3-type, $SrTiO_3$-type, and Fe_2VAl-type, respectively.

(2) *EPR*s of the TEG system for the state of the art were estimated as 51.7, 30.2, and 49.8 for Bi_2Te_3-type, $SrTiO_3$-type, and Fe_2VAl-type, respectively. With considering the increase in the output density of the module, *EPR* was expected to be larger. *EPR* of the case C might be larger than that of case A.

(3) *EPBT*s of the TEG system for the state of the art were calculated to be 0.19, 0.33, 0.20 years each for Bi_2Te_3-type, $SrTiO_3$-type, and Fe_2VAl-type, respectively. With considering the increase in the output density of the module, *EPBT* was expected to be shorter. *EPBT* of the case C might be shorter than that of case A.

4.6 References

[1] New Energy and Industrial Technology Development Organization (Nedo). *White Paper on Renewable Energy Technology (in Japanese)*, (2010).

[2] Ltd. Swcc Showa Holdings Co., (2009). *Successful long-term power generation experiment of oxide thermoelectric power generation module using industrial furnaces (in Japanese)*.

[3] Takahiko Shindo, Yujiro Nakatani, Takashi Oishi. (2008). Thermoelectric Generating System for Effective Use of Unutilized Energy. *TOSHIBA Review*, *63*, (2),

[4] Yasuhiko Hori, Tetsuo Ito, Atsushi Yamamoto, Toshitaka Ohta. (1999). Energy Analysis for Thermoelectric Generation System Using 200°C Class Fluid Heat Source. *The papers of Technical Meeting on Frontier Technology and Engineering, IEE Japan*, (1), 5-12.

[5] Yasuhiko Hori, Tetsuo Ito. (2004). Module Design Method in Themoelectric Generation System with Environmental Load Evaluation. *IEEJ Trans. PE*, *123*, (4), 597-604.

[6] P. E. Martínez, D. M. Pasquevich, A. M. Eliceche. (2012). Operation of a national electricity network to minimize life cycle greenhouse gas emissions and cost. *International Journal of Hydrogen Energy*, *37*, (19), 14786-14795.

[7] T. E. Norgate, S. Jahanshahi, W. J. Rankin. (2007). Assessing the environmental impact of metal production processes. *Journal of Cleaner Production*, *15*, (8-9), 838-848.

[8] Iso 14040:2006. *Environmental Management – Life Cycle Assessment – Principles and Framework*.

[9] Iso 14044:2006. *Environmental Management – Life Cycle Assessment – Requirements and Guidelines*.

[10] Jfe Steel Corporation. (2013). *Implementation of demonstration test of a thermoelectric power generation technology using exhaust heat*.

[11] Kelk Ltd., (2012). *KELK Launches Testing Thermoelectric Generation at Steel Mill for the First Time: NEDO's R&D project for thermoelectric generation by using exhaust heat in the steelmaking process*.

[12] Takashi Kuroki, Ryota Murai, Kazuya Makino, Kouji Nagano, Takeshi Kajihara, Hiromasa Kaibe, Hirokuni Hachiuma, Hidetoshi Matsuno. (2014). *Research and Development for Thermoelectric Generation Technology by using Exhaust heat in Steelmaking Process*.

[13] Goksin Kavlak, T. E. Graedel. (2013). Global anthropogenic tellurium cycles for 1940–2010. *Resources, Conservation and Recycling*, *76*, 21-26.

[14] Hiromasa Kaibe. (2008). "*Cascaded-type power generation module (in Japanese)*": Thermoelectric conversion technology Handbook (in Japanese), Tokyo: NTS Ltd.

[15] Hiromasa Kaibe, Takeshi Kajihara, Shinichi Fujimoto, Kazuya Makino, Hirokuni Hachiuma. (2011). Recovery of Plant Exhaust heat by a Thermoelectric Generating System. *KOMATSU Technical Report*, *57*, (164), 26-30.

[16] Shuichi Funahashi, Takanori Nakamura, Keisuke Kageyama, Hideharu Ieki. (2011). Monolithic oxide metal composite thermoelectric generators for energy harvesting. *J. Appl. Phys., 109,* 124509-124501 -124509-124504.

[17] M. Mikami, M. Mizoshiri, K. Ozaki, H. Takazawa, A. Yamamoto, Y. Terazawa, T. Takeuchi. (2013). Evaluation of the Thermoelectric Module Consisting of W-Doped Heusler Fe2VAl Alloy. *Journal of Electronic Materials, 43,* (6), 1922-1926.

[18] M. Mikami, K. Ozaki, H. Takazawa, A. Yamamoto, Y. Terazawa, T. Takeuchi. (2013). Effect of Ti Substitution on Thermoelectric Properties of W-Doped Heusler Fe2VAl Alloy. *Journal of Electronic Materials, 42,* (7), 1801-1806.

[19] M. Mikami, Y. Kinemuchi, K. Ozaki, Y. Terazawa, T. Takeuchi. (2012). Thermoelectric properties of tungsten-substituted Heusler Fe2VAl alloy. *Journal of Applied Physics, 111,* (9), 093710.

[20] Jinqing Peng, Lin Lu, Hongxing Yang. (2013). Review on life cycle assessment of energy payback and greenhouse gas emission of solar photovoltaic systems. *Renewable and Sustainable Energy Reviews, 19,* 255-274.

[21] V. M. Fthenakis, H. C. Kim. (2011). Photovoltaics: Life-cycle analyses. *Solar Energy, 85,* (8), 1609-1628.

[22] Masakazu Ito, Kazuhiko Kato, Keiichi Komoto, Tetsuo Kichimi, Kosuke Kurokawa. (2008). A comparative study on cost and life-cycle analysis for 100 MW very large-scale PV (VLS-PV) systems in deserts using m-Si, a-Si, CdTe, and CIS modules. *Progress in Photovoltaics: Research and Applications, 16,* (1), 17-30.

[23] Masakazu Ito, Mitsuru Kudo, Masashi Nagura, Kosuke Kurokawa. (2011). A comparative study on life cycle analysis of 20 different PV modules installed at the Hokuto mega-solar plant. *Progress in Photovoltaics: Research and Applications, 19,* (7), 878-886.

[24] Marco Raugei, Paolo Frankl. (2009). Life cycle impacts and costs of photovoltaic systems: Current state of the art and future outlooks. *Energy, 34,* (3), 392-399.

[25] Varun, I. K. Bhat, Ravi Prakash. (2009). LCA of renewable energy for electricity generation systems—A review. *Renewable and Sustainable Energy Reviews, 13,* (5), 1067-1073.

[26] Pre Consultants. (2011). SimaPro software 7.3.2.

[27] Japan Environmental Management and Association For Industry. (2012). IDEA ver 1. 1. 0.

[28] Shindengen Electric Manufacturing Co.Ltd. Isolated high-frequency single-phase three-wire 10kW power conditioner "SOLGRID" series "PVS010S200" launch (in Japanese). Retrived 6/14, 2014, from http://www.shindengen.co.jp/product/new_product/top_topics/20110617.html.

[29] I. Brain, O. Knacke, O. Kubaschewski. (1973). *Thermodynamic properties of inorganic substances,* Berlin and New York: Springer-Verlag.

[30] I. Brain. (1993). *Thermochemical Data of Pure Substances, Part I,* Weinheim: VCH Verlag Gesellschaft.

[31] O. Knacke, O. Kubaschewski, K. Hesselman. (1991). *Thermochemical properties of inorganicsubstances, 2nd ed.,* Berlin: Springer-Verlag.

[32] Gas and Metals National Corporation Japan Oil. *Mineral resources Material Flow 2013 (in Japanese)*, (2014).

[33] Gas and Metals National Corporation Japan Oil. *Mineral resources Material Flow 2012 (in Japanese)*, (2013).

[34] Kazuteru Tozawa. (1992). Recent Trend of Nickel Extractive Metallurgy. *Journal of the Iron and Steel Institute of Japan, 79*, (5), 537-547.

[35] J. Paul Macmillan, Jai Won Park, Rolf Gerstenberg, Heinz Wagner, Karl Kohler, Peter Wallbrecht. (2003). "*Ullmann's Encyclopedia of Industrial Chemistry, sixth ed*": 6th ed., Wiley-VCH.

[36] Keisuke Abe, Asami Kikuchi, Noriyuki Okinaka, Tomohiro Akiyama. (2014). Single thermite-type combustion synthesis of Fe2VAl for thermoelectric applications from Fe, V2O5 and Al powders. *Journal of Alloys and Compounds*, *611*, 319-323.

[37] Tetsuya Suzuki. (2006). *Studies on the effect of material-related energy saving technologies based on energy consumption structure analysis of the transport sector (in Japanese)*.

[38] (1997). *Production technology of the automobile (in Japanese)*, Tokyo: Asakura Publishing Co., Ltd.

[39] Yoshiaki Akoh, Hiroshi Tabata. (1982). Materials Recycling for Automotive Production Process. *Journal of Society of Automotive Engineers of Japan*, *36*, (8), 869-877.

[40] Waste Management and Recycling Department Ministry of the Environment Minister's Secretariat. *Industrial waste emissions and processing status survey report in Japan (in Japanese)*, (2012).

[41] The Japan Ferrous Raw Materials Association. *Year book of Tetsugen (2013) (in Japanese)*, (2013).

[42] Ministry of Economy Agency for Natural Resources and Energy, Trade and Industry (Meti). *Imports situation by country-form of major non-ferrous metals in Japan (in Japanese)*, (2013).

[43] Tsuyoshi Adachi, Gento Mogi. (2006). Inventory Analysis of CO2 Emission for Copper Ingot Production Including Mining and Mineral Processing Processes by Cost Estimating System. *Journal of Life Cycle Assessment, Japan*, *2*, (3), 238-245.

[44] Escondida. Retrived June 20, 2014, from http://resource.ashigaru.jp/top_mine_escondida.html.

[45] Haruo Sakurai, Kiyoto Yagaguchi, Yasushi Kihara, Satoru Kamanaka. (2006). The operation profile and the feature of Los Pelambres Mine. *Shigen-to-Sozai*, *122*, 606-612.

[46] Yoichi Mizuochi. (2006). Open pit minig operation at Batu Hijau Mine. *Shigen-to-Sozai*, *122*, 601-605.

[47] Gas and Metals National Corporation Japan Oil, Mitsubishi Corporation. *Efficient recovery of heavy minerals and rare earth minerals tin mine Joint study on the study of process technology (in Japanese)*, (2012).

[48] Japan Aluminium Association. *Overview of the LCI data of primary aluminum and wrought material for recycled metal*, (2005).

[49] Nickel mine in Indonesia. Retrived June 24, 2014, from http://resource.ashigaru.jp/top_mine_1.indonesia_nickel.html.

[50] Contemporary public opinion "Northern Sea Route, which begins to move" Retrived June 27, 2014, from http://www.nhk.or.jp/kaisetsu-blog/100/167690.html.

Appendix A

Source of data used in this chapter

Components	Constituents	Name of process data used in Chapter 4	Data source	Remarks
p-type element in case A				
	$(Bi_{0.5}Sb_{1.5})Te_3$	Te, semiconductor grage, @plant/GLO U	Ecoinvent unit processes	
		Crust of parks method, from removoment of Pb/GLO U	Ecoinvent unit processes	3333 kg was input to get 1 kg of metal
		thermal energy, unidentified, in chemical plant/RER U	Ecoinvent unit processes	
		Sb, @refinally/CN U	Ecoinvent unit processes	
		Power, Production mix JP/JP S		
n-type element in case A				
	$Bi_2(Te_{2.85}Se_{0.15})$	Te, semiconductor grage, @plant/GLO U	Ecoinvent unit processes	
		Crust of parks method, from removoment of Pb/GLO U	Ecoinvent unit processes	3333 kg was input to get 1 kg of metal
		thermal energy, unidentified, in chemical plant/RER U	Ecoinvent unit processes	
		Te, semiconductor grage, @plant/GLO U	Ecoinvent unit processes	
p-type element in case B				
	$Ni_{0.9}Mo_{0.1}$	Ni, 99.5%, @plant/GLO U		Ecoinvent unit processes
		Mo, @Storage area/RER U		Ecoinvent unit processes
		Power, Production mix JP/JP S		Ecoinvent system prosesses
n-type element in case B				

	$La_{0.035}Sr_{0.965}TiO_3$	La, 7.2% in bastnasite, in crude ore, in ground	-	13.9 kg was input to get 1 kg of metal
		Ammonia E	Industry data 2.0	
		Sodium carbonate from Ammonium chloride production, @plant/GLO S	Ecoinvent system prosesses	
		Fatty alcohol, Petrochemicals, @plant/RER S	Ecoinvent system prosesses	
		Thermal energy, Heavy oil, @Industrial furnaces 1MW/CH S	Ecoinvent system prosesses	
		Power, Production mix JP/JP S	Ecoinvent system prosesses	
		P ore, in ground	-	
		Water, sea water, Ocean	-	
		Peat, in ground	-	
		Anthracite, Combustion in industrial boilers/RNA	USLCI	
		Alumina, @plant/US		
		Lead concentrate, @Mineral processing/GLO U	Ecoinvent system prosesses	
		Sodium hydroxide (concentrated) E	Industry data 2.0	
		Sodium carbonate from Ammonium chloride production, @plant/GLO S	Ecoinvent system prosesses	
		Hydrochloric acid, 36% solution, From the reaction of chlorine and propylene, @plant RER U	Ecoinvent system prosesses	
		Chlorine (compression) E	Industry data 2.0	
		Rutile, 95%Titanium dioxide, @plant/AU U	Industry data 2.0	
		Sodium chloride, @plant/RNA	USLCI	
		Sulfuric acid, liquid, @plant/RER U	Industry data 2.0	
		Potassium chloride, from K2O, @Regional warehouse/RER U	Industry data 2.0	
		Thermal energy, Heavy oil, @Industrial furnaces 1MW/CH S	Industry data 2.0	
		Secondary sulfur, @Refinery/CH S	Industry data 2.0	

		Iron scrap, @plant/RER U	Industry data 2.0	
		Aluminum scrap, new scrap, @plant/RER U	Industry data 2.0	
		Alumina, @plant/US		
		La, 7.2% in bastnasite, in crude ore, in ground	-	13.9 kg was input to get 1 kg of metal
		Ammonia E	Industry data 2.0	
		Sodium carbonate from Ammonium chloride production, @plant/GLO S	Ecoinvent system prosesses	
		Fatty alcohol, Petrochemicals, @plant/RER S	Ecoinvent system prosesses	
		Thermal energy, Heavy oil, @Industrial furnaces 1MW/CH S	Ecoinvent system prosesses	
		Power, Production mix JP/JP S	Ecoinvent system prosesses	
		Power, Production mix JP/JP S	Ecoinvent system prosesses	
p-type element in case C				
	$Fe_2V_{0.6}Ti_{0.3}W_{0.1}Al$	V ore, in ground	-	223 kg was input to get 1 kg of metal
		Thermal energy, unspecified, in chemical plant/RER U		
		Pig iron, @plant, GLO/U	Ecoinvent unit processes	1.54 kg was input to get 1 kg of metal
		Aluminium, Primary bullion@plant, RER/U	Ecoinvent unit processes	
		Ti ore, in ground	-	1.74 kg was input to get 1 kg of metal
		Thermal energy, unspecified, in chemical plant/RER U	Ecoinvent unit processes	
		W ore, in ground	-	1.74 kg was input to get 1 kg of metal
		Thermal energy, unspecified, in chemical plant/RER U	Ecoinvent unit processes	
		Power, Production mix JP/JP S	Ecoinvent system prosesses	

n-type element in case C				
	$Fe_2V_{0.9}W_{0.1}Al$	V ore, in ground	V ore, in ground	223 kg was input to get 1 kg of metal
		Thermal energy, unspecified, in chemical plant/RER U		
		Pig iron, @plant, GLO/U	Ecoinvent unit processes	1.54 kg was input to get 1 kg of metal
		Aluminium, Primary bullion@plant, RER/U	Ecoinvent unit processes	
		W ore, in ground	-	2.20 kg was input to get 1 kg of metal
		Thermal energy, unspecified, in chemical plant/RER U	Ecoinvent unit processes	
		Power, Production mix JP/JP S	Ecoinvent system prosesses	
Solder				
	$Sn_{95.5}Ag_{3.9}Cu_{0.6}$	Solder, paste, Sn95.5Ag3.9Cu0.6, for electronics, @ plant/GLO U	Ecoinvent unit processes	
Electrode				
	Cu	Cu plate, technical mix, consumption mix, @plant, 0.6mm thin EU-15 S	ELCD	
Cable				
	Cu	Cu wier, technical mix, consumption mix, @plant, division 1mm2 EU-15 S	ELCD	
Substrate				
	Al2O3	Alumina, @plant/US	USLCI	
Frame				
	Polyethylene	polyethlen, HDPE, cube, @plant/RER S	Ecoinvent system prosesses	
Heat-absorbing and -emitting plate				
	Cu	Cu plate, technical mix, consumption mix, @plant, 0.6mm thin EU-15 S	ELCD	

Pump for heat emitting		Alkyd paint, white, 60% solvent, @plant/RER U	Ecoinvent unit processes	
		Sodium metasilicate pentahydrate, 58%, powder, @ plant/RER U	Ecoinvent unit processes	
		Kerosene, @ refinery/L/US	USLCI	
		Residual fuel oil, refinery @/L/US	USLCI	
		Natural gas E	Industry data 2.0	
		lubricant, @plant/RER U	Ecoinvent unit processes	
		Polycarbonate E	Industry data 2.0	
		Hot-rolled steel sheet, steel, @ plant/RNA	USLCI	
		Cr steel 18/8, @plant/RER S	Ecoinvent system prosesses	
		Cast steel, @plant/RER S	Ecoinvent system prosesses	
		Cu, from productio of Complex metal, @refinally/SE S	Ecoinvent system prosesses	
		Steel, low alloy, @plant/RER U	Ecoinvent unit processes	
		Steel, low alloy, @plant/RER U	Ecoinvent unit processes	
		Steel, low alloy, @plant/RER U	Ecoinvent unit processes	
		Diesel, diesel generator combustion/GLO S	Ecoinvent system prosesses	
		Power, low pressure, consumption mix, @ power grid/CH U	Ecoinvent unit processes	
		Combustion of natural gas, industrial equipment/RNA	USLCI	
		Process water, ion-exchange, production mix, @ plants, from the surface water RER S	Ecoinvent system prosesses	

Piping		EAF process hot-rolled steel section, blast furnace, production mix, @ plant GLO S	USLCI	
		Steel products production, average metal processing/RER U		
Support structure		EAF process hot-rolled steel section, blast furnace, production mix, @ plant GLO S	USLCI	
		Steel product production, The average metal processing/RER U		
Power Conditioner		Polymethacrylic acid, plate, @ plant/RER U	Ecoinvent unit processes	
		Polyurethane, rigid foam, @ plant/RER U	Ecoinvent unit processes	
		High-density polyethylene pipe E	Industry data 2.0	
		PVC Injection molding E	Industry data 2.0	
		PET film (production only) E	Industry data 2.0	
		Oriented polypropylene film E	Industry data 2.0	
		Oriented polypropylene film E	Industry data 2.0	
		PVC Injection molding E	Industry data 2.0	
		PVC Injection molding E	Industry data 2.0	
		Polyurethane, flexible foam, @ plant/RER U	Ecoinvent unit processes	
		Glass fiber reinforced plastic, polyamide, injection molding, plant @/RER U	Ecoinvent unit processes	
		PVC Injection molding E	Industry data 2.0	
		Hot-rolled steel sheet, steel, @ plant/RNA	USLCI	
		Cold-rolled steel, steel, @ plant/RNA	USLCI	
		Steel, electricity, non-and low-alloy, @ plant/RER U	Ecoinvent unit processes	
		Galvo, @ plant/RNA	USLCI	
		Iron and steel, production mix	USLCI	
		Steel, low alloy, @ plant/RER U	Ecoinvent unit processes	

		Steel, low alloy, @ plant/RER U	Ecoinvent unit processes	
		Cast iron, @ plant/RER U	Ecoinvent unit processes	
		Copper, blister copper, @ primary smelter/RER U	Ecoinvent unit processes	
		Copper wire, technology mix, consumption mix, @ plant, cross-sectional area 1 mm2 EU-15 S	ELCD	
		Aluminum, secondary, rolling/RNA	USLCI	
		Polyurethane, rigid foam, @ plant/RER U	Ecoinvent unit processes	
		Tap water, @ user/CH U	Ecoinvent unit processes	
		Process water, ion exchange, production mix, @ plant, from groundwater RER S	Ecoinvent system prosesses	
		Process water, ion exchange, production mix, @ plant, from groundwater RER S	Ecoinvent system prosesses	
		Electricity, production mix AT/AT U	Ecoinvent unit processes	
		Combustion of natural gas, industrial equipment/RNA	USLCI	

Appendix B

Production yields of system components

The inputs and outputs involved in producing thermoelectric modules for a TEG system were investigated in detail. Component manufacturing yields were also taken into account. Processing yields were estimated as follows: 40% of both p-type and n-type thermoelectric elements were determined through a paper-based survey among manufacturers of thermoelectric module. For the support structure and pipe, since these would not require machining of complex shapes, the material yield was assumed to be 80% [37]. Material yield was estimated as 95% for polyethylene [38, 39]. Material yield of other non–ferrous metals was assumed to be 90% [37]. Yields were not set for the pump and the power conditioner because data on inputs and outputs for these components were collected from the IDEA. For thermoelectric elements, the processing energy was estimated to be 0.216 MJ/kg from the survey. The processing energy required for the other TEG components was assumed to be included in the energy requirements for materials stated in the database. In the present study, it was not possible to collect data on assembly, so these were assumed to be zero.

Appendix C

Definition of waste recycling and management

Modules are removed and then transported to the intermediate treatment plants then broken down, crushed, and sorted. It was assumed that the cable and the electrode materials are individually separated and reproduced in a recycling plant. Figure 4–A–1

shows the breakdown of processing for industrial wastes [40]. The recycling rate for scrap metal is as high as 96%, and the final disposal rate with the exception of the reduction is 3%. Of the scrap metal from the electrode and cable, 96% is assumed to be recycled, and 3% is landfilled. The components other than the cable and electrode are considered difficult to separate and recycle at present. Therefore, after the grinding process at the intermediate treatment plant, all components other than the electrode and cable are assumed to be landfilled.

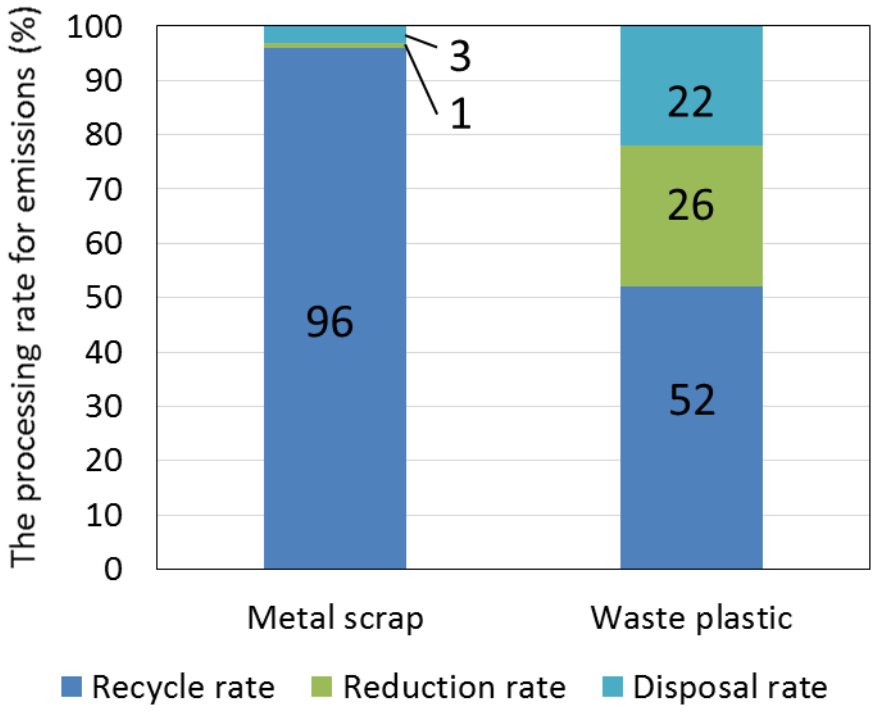


Fig. 4–A–1 Breakdown of processing for industrial wastes [40]

Iron and steel products are produced in major two streams. One produces iron and steel products by iron ore in direct reduction iron-making process and converter process. In the other, an electric furnace process mainly utilizes scrap iron, which accounts for 97–99% of the raw material in electric furnace steel production [32]. For the iron scrap, there

is home scrap generated in the factory of steel manufacturers, domestically purchased scrap that comprises industrial scrap (generated during the processing of steel, machinery, and buildings, domestically purchased scrap electrical products, etc.), and waste net scrap (that occurs at the time of disposal and dismantling). Looking at the supply and demand for domestic scrap iron in 2012, total supply was 41.1 million t and total consumption was 41.3 million t [41] (more detailed information is described in Appendix B). Therefore, the regeneration rate of steel material used in support structure and pipe was set to 100%. The transportation path assumed that the collected support structure and pipe were transported directly to the recycling plant.

At present, the power conditioner and pump are crushed at an intermediate treatment plant, and then each of the materials is regenerated or landfill after its volume is reduced. The regeneration rate of iron was set to 100% and the other non–ferrous metals to 96%. Recycling rate of plastics was assumed to be 52%; final disposal with the exception of the reduction was 22%.

The regeneration rate for the heat-emitting plate and the heat-absorbing plate is set to 96%, and 3% is assumed to be landfilled.

Regeneration rate of frame is 52%; final disposal with the exception of the reduction is 22%.

Appendix D

Definition of transport distance (Case A)

Copper ore is the main raw material for p-type element, electrodes, cables, heat-absorbing plate, and the heat-emitting plate. According to government statistics [42], 100% of the raw materials for blister copper production in Japan comprises imported copper minerals (including precipitated copper, roasted ore, sintered ore, and copper matte). Of these, 52% is supplied from Chile, 14% from Peru, and 9% from Canada. In this section, 100% of raw material for copper smelting is assumed to be copper minerals from overseas, and the transported distance was determined by the weighted average of the annual amount of imported concentrate and their transportation distance. For the elements associated with copper smelting, the following transportation stages were considered:

- from material-processing location to port in producing country (copper concentrate/land transport);
- between ports (copper concentrate/marine transport);
- from copper smelting works to processing location in Japan (bare metal/land transport); and
- from assembly location to installation in Japan (TEG unit/land transport).

Transportation stages from mine to material-processing location in the producing country; and from port to copper smelting works, and from processing location to assembly location in Japan were not considered, since the respective facilities in each country were assumed to be located near each other. The location for tellurium smelting was assumed to be the same as that for copper smelting. In all cases, transportation distance in Japan was assumed to be 50 km, via 3.5-ton truck and bulk carrier for land and marine stages respectively. Similarly, the transportation distances for lead ore, tin ore, bauxite, and iron

ore were investigated.

Table A1 Imported copper ore concentrates for Japan (1000 t/year) [43] and transportation distance

Mine site (Country)[43]	Imported concentrate [1000t/year][43]	Transportation distance [km]	
		Land	Marine
Escondida (Chile)	614 (18%)	170 [44]	16,740 (Estimated)
Los Pelambres (Chile)	410 (13%)	120 [45]	17,133 (Estimated)
Grasberg (Indonesia)	450 (13%)	173 (Estimated)	4,362 (Estimated)
Batu Hijau (Indonesia)	390 (12%)	24 [46]	5,400 (Estimated)
La Candelaria (Chile)	370 (11%)	133 (Estimated)	18,000 (Estimated)
Collahuasi (Chile)	247 (7%)	133 (Estimated)	18,000 (Estimated)
Highland Valley (Canada)	197 (6%)	332 (Estimated)	7,500 (Estimated)
Ok Tedi (P.N.G.)	200 (6%)	300 (Estimated)	5,000 (Estimated)
Antamina (Peru)	200 (6%)	576 (Estimated)	16,000 (Estimated)
Alumbrera (Argentina)	150 (4%)	1055 (Estimated)	22,000 (Estimated)
Huckleberry (Canada)	123 (4%)	300 (Estimated)	7,500 (Estimated)
Average transportation distance		**222 [km]**	**12,586 [km]**

* If there was no description of the transportation distance, the land transportation distance was assumed from the mine to the nearest trading port, and the marine transportation distance from the trading port to the port of Tokyo. Estimated values were used.

In Japan, bismuth is mainly produced from lead electrolytic slime as a by-product of lead smelting, so that lead ore is the main raw material for n-type element. The manufacture of lead involves the primary smelting industry and the playback (secondary) smelting industry. The primary smelting industry produces crude lead in the dry method from lead concentrate ore, and then produces high-purity electrolytic lead. Recycled lead produced in the secondary smelting industry is produced by a simple reverberator furnace smelting facility, a small melting furnace, such as an electric furnace using various scrap

lead and waste batteries. Recently, the recycling of batteries has been obligated, with the result that the proportion of lead manufactured from recycled batteries has increased. Of total electrolytic lead production in Japan in 2012, 41% was imported lead mineralization (precipitated lead, roasted ore, sintered ore, lead matte is also included), and 34% was from scrap [32]. Among the imported materials, 57% is supplied from Australia, 22% from the United States, and 13% from Bolivia [42]. In this chapter, 100% of the raw material for lead smelting is assumed to be lead mineralization from overseas, and transported distance was determined as described previously (see Appendix A). For the transportation of lead ore, intermediate products, and n-type element, the following stages were considered:

・from material-processing location to port in producing country (lead concentrate/land transport);

・between ports (lead concentrate/marine transport);

・from lead smelting works to processing location in Japan (bare metal/land transport); and

・from assembly location to installation in Japan (TEG unit/land transport).

Transportation stages from mine to material-processing location in the producing country; and from port to lead smelting works, and from processing location to assembly location in Japan were not considered, since the respective facilities in each country were assumed to be located near each other. Bismuth smelting location was assumed to be the same as the lead smelting location. In all cases, transportation distance in Japan was assumed to be 50 km, via 3.5-ton truck and bulk carrier for land and marine stages respectively.

Table A2 Imported lead ore concentrates for Japan (1000t/year) and estimated transportation distance

Mine site (Country)	Imported concentrate [1000t/year]	Transportation distance [km]	
		Land	Marine
Cannington (Australia)	52.5 (57%)	800	7,000
Red Dog (United States)	19.7 (22%)	280	6,900
San Cristobal (Bolivia)	11.5 (13%)	600	16,000
Average transportation distance		705 [km]	7,752 [km]

Tin is the major constituent of the solder assumed in this chapter. Of the total domestic supply of tin in 2012, 91% was imported and 3.8% was domestic production; secondary production using recovered tin sullage in Japan accounts for 0.7% [32]. For imported tin material, tin ingot accounted for 98%, and there is no import of tin ore [32]. Southeast Asia is a major partner in the importation of ingot. The main import partners in 2012 were Indonesia, Thailand, Malaysia, and Vietnam, which accounted for 55%, 30%, 8%, and 3% of the total, respectively [32]. In this chapter, it was assumed that 100% of tin supplied to the TEG system was imported from Indonesia. For the transport of the tin ingot, the following stages were considered:

- between ports (tin ingot/marine transport);
- from processing location to assembly location in Japan (bare metal/land transport); and
- from assembly location to installation in Japan (TEG unit/land transport).

Transportation stages from mine to smelter in Indonesia, and from Tokyo port to processing location in Japan were not considered, since the respective facilities in both countries were assumed to be located near each other. Marine transport was estimated to be 5511 km under the assumption that imported tin ingots were produced at a smelter

located in Muntok [47] and transportation was via bulk carrier. In all cases, transportation distance in Japan was assumed to be 50 km, via 3.5-ton truck.

The substrate, which is a structural member of the TEG system, is alumina ceramic, the raw material for which is alumina. Looking at the domestic supply and demand of alumina in 2012 [32], the total supply quantity accounted for 251,000 t (on the basis of pure metal content). Of the total amount, 63% is produced domestically and 16% is imported. An important method of producing alumina is the Bayer process, in which alumina is obtained through the aluminum hydroxide from bauxite. Aluminum hydroxide as a raw material for alumina comprised imports of 350000 t; data on domestic production and stock levels were not available. The main import partners in 2012 were Australia, Brazil, China, and Korea, which accounted for 49%, 23%, 15%, and 6% of the total, respectively [32]. In this chapter, it was assumed that 100% of alumina used in the TEG system was via aluminum hydroxide imported from Australia. For the transport of aluminum hydroxide, the following stages were considered:

- between ports (aluminum hydroxide/marine transport);
- from processing location to assembly location in Japan (alumina ceramics/land transport); and
- from assembly location to installation in Japan (TEG unit/land transport).

Transportation stages from mine to smelter in Australia, and from Tokyo port to processing location in Japan were not considered, since the respective facilities in both countries were assumed to be located near each other. Information about transportation of aluminum hydroxide was not available, so marine transport distance was estimated to be 8000 km, based on the import of new aluminum bullion [48] ; transportation was assumed to be via bulk carrier. In all cases, transportation distance in Japan was assumed to be 50 km, via 3.5-ton truck.

Steel is a major constituent of the pump, piping, support structure, and power conditioner. The mass fractions of iron in those system components were 91%, 100%, 100%, and 58%, respectively. Looking at the domestic supply of crude steel in 2012, converter steel supplied 82.8 million t and electric furnace steel 24.5 million t (on the basis of metal weight) [41]. The mixing ratio of pig iron of each converter steel and electrical steel was 89.5% and 1.1%; iron scrap otherwise became a raw material [41]. According to the Mineral Resources Material Flow of Iron 2013 [32], 100% of the iron o ore used as the raw material for domestically produced pig iron was supplied by imports. The main import partners in 2012 were Australia, Brazil, South Africa, and India, which accounted for 62%, 29%, 4%, and 2% of the total, respectively [32]. In this chapter, it was assumed that 100% of iron ore supplied to the TEG system was imported from Australia. For the transportation of iron ore, the following stages were considered:

- between ports (iron ore/marine transport);
- from steelworks to processing location in Japan (steel/land transport); and
- from processing location to installation in Japan (each component/land transport).

Transportation stages from mine to port in Australia, and from Tokyo port to the steelworks in Japan were not considered in this chapter, since the respective facilities in both countries were assumed to be located near each other. Information about the transportation of iron ore was not available, so marine transport distance was estimated to be 8000 km and via bulk carrier. In all cases, transportation distance in Japan was assumed to be 50 km, via 3.5-ton truck.

The main component of the frame is polyethylene, which was assumed to be produced in a chemical plant in Japan and transported as follows:

- from chemical plant to assembly location in Japan (polyethylene/land transport); and
- from assembly location to installation in Japan (TEG unit/land transport).

In all cases, transportation distance in Japan was assumed to be 50 km, via 3.5-ton truck.

Appendix E

Definition of transport distance (Case B)

Nickel ore is the main raw material for p-type element. The raw materials for nickel metal produced in Japan are imported matte and mixed sulfide [33]. The weight of imported matte in 2012 was 79100 t (on the basis of pure metal), mixed sulfide was 28200 t (on the basis of pure metal), and major supplier countries of matte were Indonesia and Australia, which accounted for 84% and 16% of imports respectively. In this chapter, 100% of the raw material for Ni metal is assumed to be imported matte from Indonesia, and marine transportation distance was estimated to be 4326 km [49]. or the transportation of nickel matte, the following stages were considered:

- between ports (nickel matte/marine transport);
- from Ni smelting works to processing location in Japan (nickel metal/land transport); and
- from assembly location to installation in Japan (TEG unit/land transport).

Transportation stages from mine to material-processing location in Indonesia, from material-processing works to the port in Indonesia; and from port to nickel smelting works, and from processing location to assembly location in Japan were not considered, since the respective facilities in both countries were assumed to be located near each other. In all cases, transportation distance in Japan was assumed to be 50 km, by means of 3.5-ton truck and bulk carrier for land and marine stages respectively.

Strontium is the main constituent of the n-type thermoelectric element in case B.

Strontium metal is not distributed in Japan and imports of strontium ore have been stopped. All the required strontium carbonate is imported, and major import partners are Germany, China, and Mexico, accounted for 46%, 30%, and 24% of imports [32]. In this chapter, 100% of the raw material for n–type thermoelectric was assumed to be imported strontium carbonate from Germany. Information about transportation distance was not available, so was estimated to be 422 km on land and 13700 km [50] marine. For transportation of strontium carbonate and n–type element, the following stages were considered:

- from material–processing location to port in Rotterdam [50] (strontium carbonate/land transport);
- between ports (strontium carbonate/marine transport);
- from port to processing location in Japan (strontium carbonate/land transport); and
- from processing location to installation in Japan (TEG unit/land transport).

Transportation stages from mine to material–processing location in the producing country were not considered, since the respective facilities were assumed to be located near each other. Processing of the n-type thermoelectric element and assembly of the TEG unit were assumed to be done at the same place. In all cases, transportation was via 3.5-ton truck and bulk carrier for land and marine stages respectively, and distance in Japan was assumed to be 50 km.

Chapter 5

General Conclusions

In this thesis, the feasibility of thermoelectric power generation system using exhaust heat from steel industry was studied. In this study, 1) exergy-conservative preparation methods for sustainable thermoelectric elements; La-doped $SrTiO_3$ and Fe_2VAl were proposed from the point of view of effective use of energy; 2) the environmental impacts of a thermoelectric power generation system were investigated systematically, using life cycle assessment. A summary of each chapter is as follows.

In Chapter 1, a general introduction is given; further, energy demand and supply in Japan; exhaust heat situation in Japan and also in the steel industry; and an overview of thermoelectric power generation technology. Sustainable thermoelectric materials were introduced to clarify the motivation for this thesis, and the purpose of the thesis was also described.

In Chapter 2, the effects of operating conditions of spark plasma sintering were investigated. The following findings were obtained:

(1) Spark plasma sintering of $Sr_{0.92}La_{0.08}TiO_3$ was successfully carried out at a temperature range of 1513 to 1633 K. $Sr_{0.92}La_{0.08}TiO_3$ powders were not sintered well at 1663 K, due to the formation of many intercrystalline cracks.

(2) High-temperature sintering introduced many oxygen defects that produced electrons as carriers. Thus, samples sintered at higher temperature showed high electric conductivity. However, high-temperature sintering also caused an increase in thermal

conductivity because of the increase in average grain size, therefore the optimum sintering temperature with maximized ZT was 1573 K.

(3) ZT tended to increase with temperature and peaked at around 1000 K. The maximum ZT of 0.16 at 1005 K was obtained from the sample sintered at 1573 K.

(4) Prolonged sintering introduced more oxygen defects into the sample, which can produce carrier electrons. Thus, except for the sample sintered for 15 min, samples sintered for longer times showed higher electrical conductivities.

(5) Prolonged sintering increased the grain size of the samples, which caused higher thermal conductivities.

(6) The sample sintered for only 5 min recorded the maximum ZT value of 0.37 at 1045 K. This is the largest value reported thus far for $SrTiO_3$-based bulk semiconductors.

(7) Bulk densities of sintered samples varied from 4.98 g/cm^3 of 95.0% T.D. to 5.14 g/cm^3 of 98.1% T.D., when sintering was carried out under conditions of the same heating rate of 30 K/min at 1573 K for 5 min.

(8) Samples that showed larger displacement during sintering became dense and showed higher electric conductivity.

(9) $SrTiO_3$ was successfully synthesized from SrO_2, TiO_2, and Ti in the absence of $NaClO_4$ at various $Ti/(Ti+TiO_2)$ ratios from 0.175 to 0.300.

(10) TG/DTA measurements were conducted to study the reaction mechanism during the CS of $SrTiO_3$.

(11) The apparent activation energy of the CS reaction was calculated as 287.6 kJ/mol, showing that the overall reaction was controlled by the diffusion of Sr^{2+} ions.

(12) $SrTiO_3$ of high purity was prepared by this new CS process. No detectable amounts of impurities were observed in the synthesized $SrTiO_3$. The results suggest that a one-step CS process without post-heat treatment can be employed to produce

commercially available ceramics.

In Chapter 3, new methods to synthesize Fe_2VAl based on utilizing the heat of thermite reactions were studied by means of an enthalpy–exergy diagram and a thermodynamic comparison focusing on enthalpy and exergy. The following results were obtained:

(1) *EXL* of single thermite synthesis decreased by 751 kJ per 1 mol of synthesized Fe_2VAl compared to that of double thermite synthesis, due to the reduction method of Fe. From the standpoint of exergy, Fe should be prepared through steelworks, including carbon-based iron-making, decarburization, and oxygen production, rather than via a thermite reaction using Al.

(2) By comparing *EXL* of systems, the production method consuming the least exergy was found to be the proposed single thermite synthesis method. The main reason why the single thermite synthesis method is the most suitable for producing Fe_2VAl is that the sensible heat of V can be utilized effectively for the alloying of Fe_2VAl.

(3) The total *EXL* of conventional arc-melting method and two proposed methods, single thermite synthesis and double thermite synthesis, were calculated to be 807 kJ, 562 kJ, and 1313 kJ per 1 mol of synthesized Fe_2VAl, respectively. The proposed single thermite synthesis decreased the *EXL* by 30% compared to that of the conventional arc-melting method.

In chapter 4, the life cycle of a thermoelectric power generation system with three pairs of thermoelectric elements was investigated under the assumption of recovering exhaust heat from the steel industry, and the following results were obtained:

(1) *GHG* emission rates of the TEG system for the state of the art were calculated to be 7.0, 7.6, 4.6 g CO_2 eq./kWh_p for Bi_2Te_3-type, $SrTiO_3$-type, and Fe_2VAl-type, respectively.

(2) *EPR*s of the TEG system for the state of the art were calculated to be 51.7, 30.2, and 49.8 each for Bi_2Te_3-type, $SrTiO_3$-type, and Fe_2VAl-type, respectively. With considering the increase in the output density of the module, *EPR* was expected to be larger. *EPR* of the case C might be larger than that of case A.

(3) *EPBT*s of the TEG system for the state of the art were calculated to be 0.19, 0.33, 0.20 years each for Bi_2Te_3-type, $SrTiO_3$-type, and Fe_2VAl-type, respectively. With considering the increase in the output density of the module, *EPBT* was expected to be shorter. *EPBT* of the case C might be shorter than that of case A.

In this study, combustion synthesis was utilized for the development of exergy-conservative production processes of $SrTiO_3$-based and Fe_2VAl thermoelectric elements. For the $SrTiO_3$ type, combustion synthesis with post-spark plasma sintering successfully led the improvement of merit since grain growth were effectively suppressed and oxygen defects can be introduced at the same time, which resulted in the low thermal conductivity and good electronic properties. For the Fe_2VAl, thermodynamic analysis was pursued and the usefulness of thermite synthesis was revealed in terms of exergy efficiency. Additionally, LCA was used to quantify the environmental impact of thermoelectric power generation, focusing on the composition of the elements.

APPENDIX

Publications

1. ***Asami Kikuchi***, Noriyuki Okinaka, and Tomohiro Akiyama "Thermodynamic Analysis of Thermite Synthesis for Thermoelectric Fe_2VAl", *Journal of Applied Thermal Engineering*, **70** (2014) 876-883.
2. ***Asami Kikuchi***, Noriyuki Okinaka, and Tomohiro Akiyama "Novel Combustion Route for $SrTiO_3$ Powders", *Applied Physics Express* **5** (2012) 041201.
3. ***Asami Kikuchi***, Lihua Zhang, Noriyuki Okinaka, Tsuyoshi Tosho and Tomohiro Akiyama "Optimization of Sintering Temperature for Maximizing Dimensionless Figure of Merit of La-Doped Strontium Titanate Thermoelectric Material in the Combination of Combustion Synthesis with Post Spark Plasma Sintering", *Materials Transactions*, **51**, (10) (2010) 1919-1922.
4. ***Asami Kikuchi***, Noriyuki Okinaka and Tomohiro Akiyama "A large thermoelectric figure of merit of La-doped $SrTiO_3$ prepared by combustion synthesis with post-spark plasma sintering", *Scripta Materialia*, **63**, (2010) 407–410.
5. ***Asami Kikuchi***, Lihua Zhang, Noriyuki Okinaka, Tsuyoshi Tosho and Tomohiro Akiyama "Effects of Sintering Temperature on Thermoelectric Device of La- Doped Strontium Titanate in the Combination of Combustion Synthesis and Spark Plasma Sintering", *Materials Transactions*, **50**, (11) (2009) 2675-2679.

Review Paper

1. Noriyuki Okinaka, ***Asami Kikuchi***, Tsuyoshi Tosho and Tomohiro Akiyama "Heat Recovery Using Thermoelectric Generator (TEG)", Journal of the Japan Institute of Energy, **88**, (2009) 961-966.

Presentations (International)

1. ***Asami Kikuchi***, Noriyuki Okinaka and Tomohiro Akiyama, "Life Cycle Materials and Energy Balance of Thermoelectric Generation System Using Exhausted Industrial

Heat", 32nd International Conference on Thermoelectrics, Kobe, Japan June 30–July 4, 2013.

2. ***Asami Kikuchi***, Noriyuki Okinaka and Tomohiro Akiyama, "Densification Behavior of Thermoelectric Strontium Titanate during Spark Plasma Sintering", Powder Metallurgy World Congress and Exhibition 2012, Yokohama, Japan, 14–18 Oct, 2012.
3. ***Asami Kikuchi***, Noriyuki Okinaka and Tomohiro Akiyama, "Thermite Synthesis of Fe_2VAl", 31st International & 10th EuropeanConference on Thermoelectrics, Aalborg, Denmark, 9–12 Jul, 2012.
4. ***Asami Kikuchi***, Sidney Lin, Noriyuki Okinaka and Tomohiro Akiyama, "Optimization of Spark-Plasma-Sintering Conditions for Maximizing Figure of Merit of La-Doped $SrTiO_3$", 35th International Conference and Exposition on Advanced Ceramics and Composites, Florida, USA, 23–28 Jan, 2011.
5. ***Asami Kikuchi***, Noriyuki Okinaka and Tomohiro Akiyama, "Optimization of Holding Time for Maximizing Figure of Merit of La-Doped $SrTiO_3$ Prepared by Combustion Synthesis and post Spark Plasma Sintering", 8th European Conference on Thermoelectrics, Como, Italy, 22–24 Sep, 2010.
6. ***Asami Kikuchi***, Lihua Zhang, Noriyuki Okinaka, Tsuyoshi Tosho and Tomohiro Akiyama, "Optimization of Sintering Temperature for Producing Thermoelectric Device of La-doped $SrTiO_3$", 39th Australian Chemical Engineering Conference, Perth, Australia, 27–30 Sep, 2009.

Presentations (Domestic)

1. ***Asami Kikuchi***, Takeshi Kajiwara, Kunihiro Hatiuma, Noriyuki Okinaka and Tomohiro Akiyama, "Materials and Energy Balance of Thermoelectric Generation System Using Exhausted Industrial Heat", The 8th Meeting of the Institute of Life Cycle Assessment Japan, Ritsumeikan University, Kusatsu, 6–8 March, 2013.
2. ***Asami Kikuchi***, Noriyuki Okinaka and Tomohiro Akiyama, "Effects of Current Profiles during SPS for Producing Thermoelectric Devices of La-doped $SrTiO_3$ in the Combination of Combustion Synthesis and Spark Plasma Sintering", 149th Japan Institute of Metals, Okinawa Convention Center, Ginowan, 7–9 November, 2011.

3. ***Asami Kikuchi***, Noriyuki Okinaka and Tomohiro Akiyama, "Thermoelectric Properties of La-doped $SrTiO_3$ Spark-Plasma-Sintered for various holding times", 146th Japan Institute of Metals, Tsukuba University, Tsukuba, 28–30 March, 2010.
4. ***Asami Kikuchi***, Noriyuki Okinaka and Tomohiro Akiyama, "Optimization of Sintering Holding Time for Producing Thermoelectric Devices of La-doped $SrTiO_3$ in the Combination of Combustion Synthesis and Spark Plasma Sintering", 75th Society of Chemical Engineers, Kagoshima University, Kagoshima, 18–20 March, 2010.
5. ***Asami Kikuchi***, Noriyuki Okinaka and Tomohiro Akiyama, "Thermoelectric Properties of La-doped $SrTiO_3$ Spark-Plasma-Sintered for various holding temperatures", 145th Japan Institute of Metals, Kyoto University, Kyoto, 15–17 September, 2009.
6. ***Asami Kikuchi***, Noriyuki Okinaka and Tomohiro Akiyama, "Thermoelectric Properties of Nonstoichiometric $SrTiO_{3-\delta}$ Prepared by Combustion Synthesis and Spark Plasma Sintering", 6th Thermoelectrics Society of Japan, Tohoku University, Sendai, 10–11 August, 2009.
7. ***Asami Kikuchi***, Noriyuki Okinaka, Tsuyoshi Tosho and Tomohiro Akiyama, "Optimization of Sintering Temperature for Producing Thermoelectric Devices of La-doped $SrTiO_3$ in the Combination of Combustion Synthesis and Spark Plasma Sintering", 157th The Iron and Steel Institute of Japan, Tokyo Institute of Technology, Tokyo, 28–30 March, 2009.

Awards

1. ***Asami Kikuchi***, Support of ¥300,000 for International Technological Interaction funded by Murata Science Foundation, Tokyo, Japan (2012).
2. ***Asami Kikuchi***, Support of ¥197,000 for International Technological Interaction funded by TEPCO Memorial Foundation, Tokyo, Japan (2010).
3. ***Asami Kikuchi***, Support of ¥804,020 for travel fee and living cost at Lamar University as an exchange student funded by Hokkaido University, Sapporo, Japan (2010).

Acknowledgments

謝辞

この論文をまとめるにあたり、指導教官である北海道大学 大学院工学研究院 エネルギー・マテリアル融合領域センター センター長 秋山友宏教授に深く感謝申し上げます。著者は 2008 年 4 月の学部 4 年時にエネルギーメディア変換材料研究室に配属され、以来 6 年半の長きにわたり熱心にご指導をいただきました。研究に行き詰まったときはいつも丁寧にアドバイスをいただき、適切な方向に導いて下さいました。学会発表、国際会議、プロジェクトや研究会などの貴重な経験も財産となりました。また、体調や家族の事にも配慮下さり、理解を示し寛大に受け入れて下さった事にも感謝しています。ありがとうございました。

本論分の審査をして下さった材料科学専攻 鈴木亮輔教授、松浦清隆教授、環境創生工学部門 松藤敏彦教授には有意義なご指摘やご意見をいただきました。感謝申し上げます。また、審査委員となっていただいた他の材料科学専攻の先生方にも感謝申し上げます。

第 2 章、第 3 章をまとめるにあたり、沖中憲之准教授にご指導をいただきました。また、パソコンやネットワーク関連のことでも大変お世話になりました。おかげさまで研究を円滑に進めることができました。感謝申し上げます。

第 4 章をまとめるにあたり、独立行政法人 国立環境研究所 中島謙一氏にご指導いただきました。中島さんとの出会いがなければ第 4 章を書き上げることはできませんでした。ご多忙の中、親切丁寧にご教授くださりありがとうございました。感謝申し上げます。

今回同時に博士論文を提出した牛晶さんとは、共に助け合いながら頑張ってきました。挫折しそうになったとき、牛さんの励ましが大きな力となりました。感謝申し上げます。また、衣雪梅助教、能村貴宏助教、渡辺美紀氏、千葉香織氏をはじめ、エネルギーメディア変換材料研究室の学生、スタッフの皆様に感謝申し上げます。

最後に、修士課程修了まで経済的に支援してくれたお父さん、秋田－札幌間を何度も往復し家事育児を手伝ってくれたお母さんに感謝します。心配や苦労をたくさんかけてしまいましたが、両親のおかげで無事学位を取得し、納得のいく形で学生生活を終わる事ができます。また、家事育児の分担、研究のディスカッション、時にはサンドバッグとなり、心身を支え、安らぎを与えてくれた夫と、笑顔と泣き顔と日々の成長で精神的な支えとなってくれた長男に感謝します。両親と家族の支えがなければこの論文は書き上げることができませんでした。この場を借りて感謝申し上げます。

2014.8.18

大矢麻美